Fusion of Deformable and Biomechanical Models for Tracking Left Ventricular Endocardium by Echocardiography

by

Hussin Shaban Ketout

Submitted in partial fulfilment of the requirements
for the degree of Doctor of Philosophy

at

Dalhousie University
Halifax, Nova Scotia
September 2013

TO MY PARENTS,
MY BROTHERS,
MY SISTERS,
MY WIFE
AND
MY CHILDREN

TABLE OF CONTENTS

LIST OF TABLES

LIST OF FIGURES

ABSTRACT

Biomedical image processing is a very important research area. Image analysis is one of the most important techniques in studies related to heart functions. The clinical assessment of LV function is very important to evaluate the heart function for patients or suspected heart disease sufferers. 2D echocardiography allows us to study the dynamic analysis of the heart which results in obtaining the quantitative and qualitative analysis of the LV. Cardiac function quantitative analysis depends on the heart's shape characteristics like the enclosed area and heart wall thickness. The segmentation of medical images and obtaining the traces of the LV boundaries is an essential procedure to get the quantitative and qualitative analysis. Yet, in clinical procedure, this task depends on manual tracing which is slow, tedious and time consuming job. Hence, automating this clinical procedure during the cardiac cycle is of great importance. The aim of this thesis is to automate the manual process of detecting and tracking the LV boundaries of 2D echocardiographic image sequence. Instead of depending only on the imaging based techniques, the designed and implemented framework utilizes the LV mechanics beside the imaging based techniques. When it comes to information extraction from patterns which have been classified, it has been proved that the different contour detection methods complement each other. As a result, efficient combination of different contour detectors is expected to achieve better contour detection than if only one detector is used. This combination of contour detectors produces incremental gains in overall performance. In the first framework, the detection and tracking are accomplished by employing the extended Kalman filter framework to combine the contours estimated by the biomechanical model and the contours extracted using the deformable models. An alternative framework is used by employing averaging fusion followed by level set method. A gold standard is created from three manual outlines and utilized in the experimental results to evaluate the automated results. The tracking and segmentation of LV during the cardiac cycle was accomplished successfully in all cases. The results showed limits of agreement for an average perpendicular distance of 1.277 ±0.252 mm versus the created gold standard. This proved that this framework achieved better performance in tracking and segmenting the LV through the cardiac cycle.

LIST OF ABBREVIATIONS AND SYMBOLS USED

List of Abbreviations

2D	Two Dimensional
ED	End Diastolic
ES	End Systolic
LV	Left Ventricular
RV	Right Ventricular
RA	Right Atrium
LA	Left Atrium
ACM	Active Contour Models
CLG	Combined Local and Global
MRF	Mark of Random Field
Ed	Data Energy
Ep	Point Energy
ASM	Active Shape Model
PCA	Principle Component Analysis
PMD	Points Distribution Model
AAM	Active Appearance Model
AV	Atrioventricular valve
EDV	End Diastolic Volume
ESV	End Systolic Volume
SV	Stroke Volume
PA	Pulmonary Aortic Valve
A	Aortic
LVV	Left Ventricular Volume
LVP	Left Ventricular Pressure
PV	Pressure Volume loop
EF	Ejection Fraction
BEM	Boundary Element Method
FEM	Finite Element Method

APD	Average Perpendicular Distance
CV	Chan-Vese Level Set Method
SNR	Signal to Noise Ratio
TI	Temporal Information
SI	Spatial Information
SPF	Signed Pressure Function
PDE	Partial Differential Equation
BIE	Boundary Integral Equation
EKF	Extended Kalman Filter
1st PK	First Piola-Kirchhoff Stress Tensor
2nd PK	Second Piola Kirchhoff Stress Tensor
ECG	Electrocardiography
MRI	Magnetic Resonance Imaging
CT Scan	Computed Tomography scan
MVN_CNN	Multi Valued Neural Cellular Neural Networks
UBN_CNN	Universal Binary Neural Cellular Neural Networks
FCNN	Fuzzy Cellular Neural Networks
ANN	Artificial Neural Networks
CNN	Cellular Neural Networks

List of Symbols

G_x	Derivative of the Image in the x Direction
G_y	Derivative of the Image in the y Direction
τ	Sampling Point
k_f	Curvature
k_g	Curvature
E_{total}	Total Energy of Snake
E_{int}	Internal Energy of Snake
E_{img}	Image Energy
α	Control Parameter for the Snake
β	Control Parameter for the Snake
C_0	Initial Contour

$F(k)$	Speed Function
N	Normal Vector
ϕ	Level Set Function
ϕ_t	Derivative of the Level Set Function
δ_x	Displacement in the x Direction
δ_y	Displacement in the y Direction
δ_t	Time Period
v_x	x Image Velocity
v_y	y Image Velocity
I_x	Derivative of the Image w.r.t. x
I_y	Derivative of the Image w.r.t. y
I_t	Derivative of the Image w.r.t. t
v	Optical Flow
$\bar{x}$	Mean
$d\bar{x}$	Derivative of each Shape
$\sum$	Covariance Matrix
P_i	Eigen Vectors
λ_i	Eigen Values
P	Eigen Value Matrix
g	Constant Value
b	Weight Vector
T	Model Vector
s	Scale Matrix
θ	Rotation Matrix
t_x	Translation in x Direction
t_y	Translation in y Direction
A_λ	Synthesized Appearance
E	Strain
R_0	Reference Configuration

R_t	Deformed Configuration
x	Undeformed State
X	Deformed State
J	Jacobian
u	Displacement
F	Deformed Gradient
dx	Gradient of Undeformed State
dX	Gradient of Deformed State
du	Gradient of Displacement
λ	Stretch Ratio
df	Infinitesimal Force
dS	Surface Element
σ	First Piola Kirchoff Stress Tensor
S	Second Piola Kirchoff Stress Tensor
C	Right Cauchy Deformation
$I_1,\ldots,I_5$	Invariants of Right Cauchy Deformation
P_{hyd_active}	Hydrostatic Pressure in the Active Phase
$P_{hyd\_passive}$	Hydrostatic Pressure in the Passive Phase
W_{pass}	Strain Energy Function for the Passive Phase
W_{active}	Strain Energy Function for the Active Phase
Q	Constant Parameter
$c_1\ldots$	Material Parameters
x^p	Load Point
x^d	Displacement Point
U_{kl}	Fundamental Solution for the Displacement
T_{kl}	Fundamental Solution for the Stress
R	Distance Between Load Point and Displacement Point
σ^L	Linear Stress
σ^n	Nonlinear Stress
σ_{ij}	Total Stress

E_f	Fiber Stiffness
E_p	Cross Fiber Stiffness
ν_p, ν_{fp}	Poisson Ratio
G_f	Shear Models across Fiber
t	Boundary Traction
Γ	LV Boundary
Ω	LV Domain
D_{ijk}	Derivative of Fundamental Solution T_{kl}
K_{ijm}	Derivative of Fundamental Solution U_{kl}
N_n	Shape Function
ξ	Intrinsic Co-ordinates
H	Coefficient Matrix
g	Coefficient Matrix
f	Coefficient Matrix
y	Matrix of Unknowns
A	Coefficient Matrix
M	Number of Cells in the LV Domain
∇u	Displacement Gradients
N_g	Number of Gaussian Points
ξ_n	Gaussian Co-ordinates
ω_n	Associated Weight
$r_{,x}$	Derivative of Distance w.r.t x
$r_{,y}$	Derivative of Distance w.r.t y
η	Unit Vector along Tangential Vector Direction
I_Γ	Integration Value of Fundamental Solution T_{kl}
I_U	Integration Value of Fundamental Solution U_{kl}
C_i^n	Coefficient Matrix
F^n	Coefficient Matrix
H^n	Coefficient Matrix
z_k	Measurement Value at time k

x_k	Predication State at time k
$\hat{x}_k$	Next State Estimate
A_1	Coefficient Matrix
A_2	Coefficient Matrix
D	Coefficient Matrix
x^{BM}	Contour Computed by Biomechanical Model
x^{Snake}	Contour Computed by Snake
R	Measurement Covariance Matrix
Y	Average Curve
$X_1 \ldots$	M given Curves
A	Scatter Matrix
α_m, α_M	Eigen value
a_m, a_M	Eigen vectors
M	Number of Given Curves
E_d	Data Energy
E_p	Prior Energy
e_i	Unit Vector
α_{kj}	Constant Value
Be	Number of Boundary Elements in LV domain
Face1,Face2,Face3	Faces of the Triangle Element at the Boundary of LV
E_{image}	Image Energy
E_{edge}	Edge Energy
E_{INT}	Internal Image Energy
Δ	Control Factor
K_k	Kalman Gain
C_0	Initial Contour
x_{k-2}	Contour of Frame Number *k-2*
x_{k-1}	Contour of Frame Number *k-1*
$\hat{x}_k$	Predicted Contour of Frame Number *k*
x_k	Contour of Frame Number *k*

P_k	Error Covariance Matrix
C_{avg}	Average Computed Contour
ϕ	Zero Level Set Function
$\varepsilon(\phi)$	Variational Function
$\rho(\phi)$	Penalization Term
μ	Constant
$\varepsilon_{g,\lambda,\nu}(\phi)$	Energy Functional
λ,ν	Constants
H	Heaviside Function
l_1	Average Intensities Inside Object
l_2	Average Intensities Outside Object

ACKNOWLEDGEMENTS

First and foremost, all the thanks and praises should go to ALLAH who gave me courage to complete my degree. I want to thank my great mother, my lovely wife and my lovely children for their support and patience during this part of my educational life.

I would like to express my deepest thanks and appreciation to my supervisor Professor Jason Gu. The encouragement, support, and advice from my supervisor have been immeasurable. From the very first day of my degree, he provided me guidance with my research work. My thesis would not be possible without his guidance and continues help.

I would like to acknowledge the advice and guidance provided by my committee members Professor Mo El-Hawary and Professor William Phillips. It was a pleasure to have such amazing people on my committee and to be able to benefit from their expertise

I would like to acknowledge and thank the Cardiologists from Queen Elizabeth II Halifax Infirmary, Cardiac Sonographer, Capital Health Authority: Dr Gabrielle Horne, Cindy MacDougall, Josette D'Eon, Carly Lucas for providing me the manual tracings of the samples that used to create the gold standard.

I would like to express my thanks and appreciation to Professor LI, Youfu to be the external examiner of my thesis.

CHAPTER 1 INTRODUCTION

1.1 MOTIVATION

Biomedical image processing is a very important research area. One of the key aspects is using the techniques of the image analysis to investigate the patient's heart function [1]. The clinical assessment of LV function is the major key in the evaluation of heart function for patients or suspected heart disease sufferers. In the clinical routine, 2D echocardiography is commonly used to determine the LV function to obtain the quantitative and qualitative analysis of the heart [1, 2]. Clinically, quantitative analysis is more preferable over qualitative analysis, especially for wall motion and volume estimation [3]. The cardiac function Quantitative analysis depends on shape attributes of the heart like the computed volume or area and the heart wall thickness [4]. Tracing the borders during the end-diastolic (ED) and end-systolic (ES) periods on 2D echocardiographic images allows analysts to compute clinically important measures such as regional wall thickness and ejection fraction. On the other hand, tracing the borders on complete cardiac cycle images gives the quantitative analysis of the LV contraction dynamics [2].

Most of the researchers have focused their research on LV analysis by detecting, segmenting and tracking the LV over the cardiac cycle. LV is responsible for pumping blood from the heart to the whole body. By examining the functioning of the LV, many conditions and disease can be discovered [5]. In medical imaging, the segmentation and obtaining the tracing of the boundaries of the heart is a significant step to take out the qualitative and quantitative measurements [1], Figure (1.1).

Figure (1.1) - Normal and abnormal heart [6]

However, manual tracing is still the only way to perform this job in the clinical practice [7]. Manual tracing of the LV boundaries is a very slow process that leads to consume a lot of time and ends up with a tedious work. Furthermore, the resulting tracings vary between different cardiologists [7, 8]. Hence, there is a clinical need for automatically detecting these borders over the cardiac cycle [7]. "Amongst the other medical imaging modalities, 2Dechocardiography is valuable for patients with heart diseases. It is non-invasive, non-radioactive, portable, real time, easy to use in clinical environment and non-expensive when compared to other modalities" [8, 9]. Automatic LV border detection and tracking over the cardiac cycle in echocardiographic image sequences remains an open and challenging problem due to many difficulties related to the heart and its dynamics, as well as other difficulties related to the echocardiography ultrasound machine.

1.2 Challenges and Difficulties with Tracking Echocardiographic Image Sequence

Echocardiographic image sequence has many challenges and difficulties that can hamper not the automation process but also the human interpretation. The challenges and difficulties are as follows:

- Echocardiography ultrasound images suffer from poor resolution and quality with several artifacts such as shadowing, speckle and side lobes [1, 8].

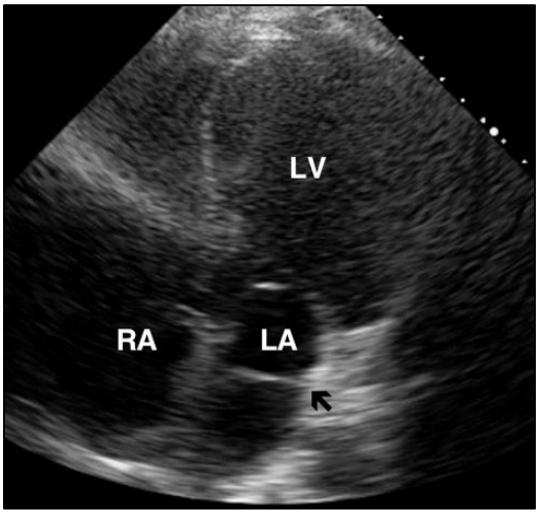

Figure (1.2) - Poor quality of 2D echocardiographic images

- Images of echocardiography suffer from signal dropout. This dropout in the echocardiography signal makes part of the LV boundary invisible, which yields an open contour as shown in Figure (1.3) [2, 8].

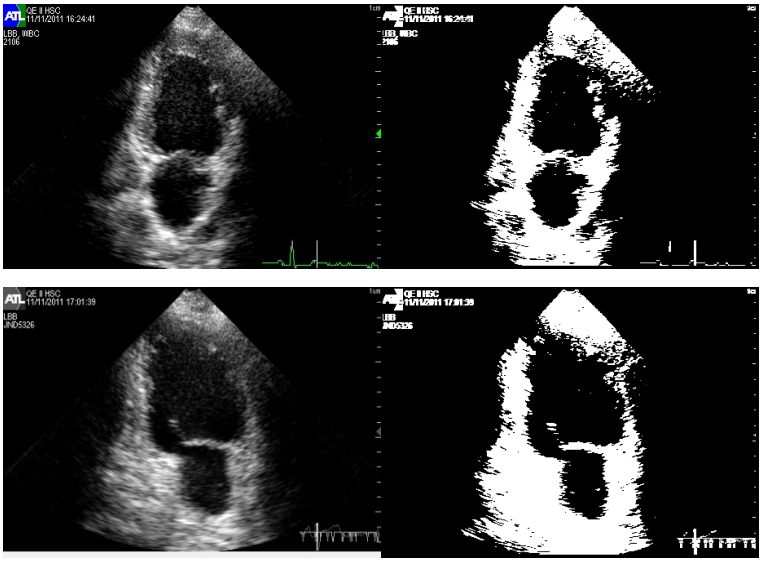

Figure (1.3) - 2D echocardiography images signal dropout and missing parts of the LV contour

- Low signal to noise ratio (SNR) and limited echo windows [2, 8].
- Gray level intensity variability [10].

- The LV real boundaries cannot always extract from the strongest images features. The strongest edge locations do not always relate to the real contour as drawn by cardiologists [3].
- The heart itself is a highly deformable object with a wide range of motion. The papillary muscle impedes the detection of the real LV boundary. The mitral valve also is one of the contributors to the problem of detecting the LV boundaries.

The problem of LV detection, segmentation and tracking is still open and challenging. Numerous of the proposed methods have shown good results after evaluating the methodologies with good quality images [11]. Up to date, there is no methodology clinically approved to be used in clinical routine for automatic or semiautomatic LV segmentation or tracking [11]. There is still demand of robust methodology to detect, segment and track the LV of 2D echocardiographic images for estimating quantitative and qualitative parameters [12].

1.3 THESIS OBJECTIVES AND CONTRIBUTIONS

To tackle the challenges and difficulties due to echocardiographic images and LV complex motion, the objective of this thesis is developing a robust and reliable framework to track and segment LV through a 2D echocardiographic image sequence.
The contributions of the thesis can be listed and illustrated by the following points:

- Unlike the previous work done for segmenting and tracking the LV from 2D echocardiographic image sequence, this approach does not depend on the imaging based techniques alone. Depending in imaging based techniques alone does not provide the solution to the difficulties and challenges due to the ultrasound images and the heart. The novelty in the framework is by utilizing the LV mechanical properties through the BM model. The BM model is represented by the constitutive equations that simulate the LV movement and function. Also, another novelty is by using FEM to track and segment LV contour and area. ABAQUS FEM is used to solve the BM model constitutive equations and provide the deformations of the LV to find its new shape and contour through the cardiac cycle.

- The heart is load dependent. The movement and deformations of the LV during the cardiac cycle depends on the amount of the load that applied to its boundaries. So, finding the exact and suitable amount of load at each time step in the cardiac cycle is crucial point in the solution of BM model equations. By finding the relation between the frames and the pressure, we can simulate the pressure in each frame. This relation enables us to provide the specific load required in each frame.
- The myocardium tissue is anisotropic, highly nonlinear, undergoes large deformations and time dependent [13, 14]. To get the exact deformations of the LV at each frame in the cardiac cycle, the exact time is provided to the FEM to run the BM model solution procedure. The BM model will deform in the same time that the real LV will deform from one to another shape in the cardiac cycle.

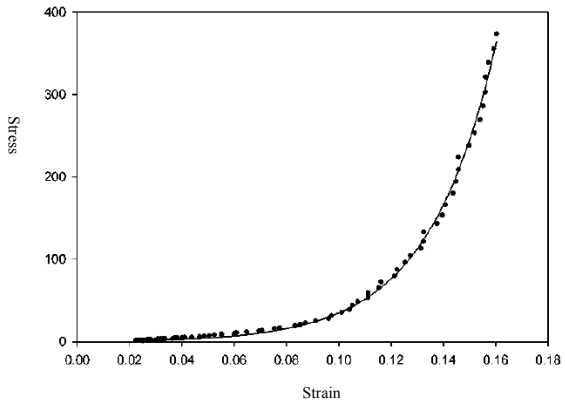

Figure (1.4) - Stress and strain relationship in LV myocardium tissue [15]

- Employing the BM model in the solution provides the stability and robustness to the tracking framework. Moreover, the BM model enables to detect the LV contour in positions where parts of the LV are missed in the image or suffered from signal drop out. By integrating the BM model in the tracking framework, it gains the ability to detect and track the LV through the 2D echocardiographic image sequence independently from the quality of ultrasound images.
- When it comes to information extraction from patterns which have been classified, it has been proved that the different contour detection methods complement each other. As a result, efficient combination of different contour

detectors is expected to achieve better contour detection than if only one detector is used. This combination of contour detectors produces incremental gains in overall performance [7, 16, 17]. By fusing the contours of the deformable and BM models, we can overcome the difficulties and challenges due to the 2D echocardiographic images and LV. The evaluation of the framework shows, the %95 confident level of the framework is 1.277±0.285 mm

1.4 THESIS OUTLINE

The thesis is divided into seven chapters and they listed as follows:

- The first chapter addresses the motivation behind this work, the challenges and difficulties facing this work and the objective and contribution of the thesis.
- The second chapter provides the literature review of the previous work about tracking the LV borders through the echocardiographic image sequence with a brief explanation about the technique used and the shortcomings in each work.
- A medical background is given in the third chapter. A brief about the definitions of the medical terms, the phases of the cardiac cycle and the pressure and volume loop is presented.
- Detailed information about the biomechanical model with continuum mechanics, strain energy functions and the equations of the LV stresses are given in chapter four. Also, the FBEM (Field Boundary Element Method) is introduced along with the derivation of the nonlinear equation of FBEM and the iterative incremental solution to get the LV deformation. FEM is used instead of FBEM to solve the BM constitutive equations. Complete details are given for the solution, along with a brief introduction to the ABAQUS model.
- Chapter five presents the Snake, the Kalman filter and the combination of the Snake with the BM model by utilizing EKF. Averaging framework is used instead of EKF. Detailed information is given about this framework.
- Chapter six is about creating the gold standard, the experimental results and the evaluation of these experimental results by comparing them with the the created gold standard.
- In the last chapter, the conclusion of the thesis is given with the future work.

- In APPENDIX I, images of tracking and segmenting LV in a complete cardiac cycle are given with the plot of all the computed contours.
- In APPENDIX II, a sample of running the BM model to compute the deformations of the LV during contraction phase is given.
- In APPENDIX III, a sample of the computed deformations of the LV during passive phase.
- In APPENDIX IV, ten tables of the X-Y coordinates data for the manually plotted contour of the three cardiologists for all the samples along with the created the gold for each sample

CHAPTER 2 LITERATURE REVIEW

2.1 INTRODUCTION

Clinically speaking, LV segmentation and tracking is very important. This importance led to a long search for a good segmentation and tracking algorithm to be medically applicable. This search resulted in many segmentation and tracking algorithms published in computer vision and other related journals. Methods for LV contour extraction and tracking can be categorized into eight approaches according to the technique used in the approach

2.2 EARLY COMPUTER VISION APPROACHES

Contour detection is one of the well-used techniques in computer vision and it is the first step in image segmentation [18]. This importance led to a long search for a good contour detection algorithm to be used in a variety of applications. Many contour detection algorithms were published in image processing journals [18]. Methods for contour extraction are categorized into two approaches; the first is the bottom-up method (early vision techniques) and the second approach the top down method, which include Active Contour Models (ACM-deformable models) and other recently developed techniques. Early methods of edge detection techniques rely on the gradient method to detect the edges by looking for the maximum and minimum in the first derivative of the image [19, 20]. If *f(x, y)* refers to the image, the gradient of point (x, y) is defined as follows:

$$\nabla f = \begin{bmatrix} G_x \\ G_y \end{bmatrix} = \begin{bmatrix} \frac{\delta f}{\delta x} \\ \frac{\delta f}{\delta y} \end{bmatrix} \tag{2.1}$$

The solution of this equation will be:

$$\nabla f = mag(\nabla f) = \left[G_x{}^2 + G_y{}^2 \right]^{\frac{1}{2}}$$

$$= \left[\left(\frac{\delta f}{\delta x} \right)^2 + \left(\frac{\delta f}{\delta y} \right)^2 \right]^{\frac{1}{2}} \qquad (2.2)$$

And its direction as $\theta(x, y) = \arctan(G_y / G_x)$

More advanced techniques such as Fuzzy logic, artificial neural networks and cellular neural networks are also used for edge detection purposes. In early vision techniques, the edge detection is extracted, followed by the boundary formation where the gaps between edges are filled (edge linking). Following is an explanation of the work relating to this category.

L. Zhang *et al.* [10] assumed that important information concerning the edges to be detected was present in the motion between sequential video frames. The algorithm requires the operator to define the end diastolic, end systolic and the closing end diastolic frame for the cardiac cycle; and roughly define the border on each frame. Once the operator has defined these boundaries, the threshold will be decided automatically, followed by a search region limited by the initial outlined from the observer in each frame. Lastly, border detection and spatial and temporal smoothing is carried out. D. Wilson *et al.* [21] used large matched filters to extract the endocardial and epicardial boarders during the systole in 2D short axis. The algorithm introduced by C. Chu *et al*. [4], first detects spatially significant features from image intensity variations. This is followed by a process of edge thinning and linking to remove false edges and filling gaps by interpolation. A final refinement process is then used for ensuring an accurate estimate of the boundaries. The approach of I. Herlin *et al.* [22] takes the time sequence echocardiographic images as input, extracting the edges of the image, initiates the segmentation of a preselected anatomical structure and uses deformable model for tracking. M. Baroni *et al.* [23] utilized Gaussian filtering at both coarse and fine scales to detect the LV edges. The coarse edges are used to define the region of interest as a binary map throughout image sequence. A contour template is matched against the gradient of the first image. Two contours are estimated, one by maximizing an edge likelihood function and the other by using a region growing algorithm. Both edge and region contours are combined by maximizing another likelihood function with the edge map

computed at fine scale. In our work [24], a Fuzzy logic is used to extract the LV endocardial after smoothing the image with contrast enhancement. Four inputs are given to the Fuzzy IF THEN inference system. Each input has five linguistic variables named VLOW, LOW, MED, HIGH and VHIGH. The Fuzzy rules have the ability to detect the endocardial edges even in low contrast regions. In [1], FCNN is used to detect the endocardial edges instead of pure Fuzzy logic. MVN_CNN nonlinear filter is used as image smoother due to its ability to remove the noise while keeping the image information. In [25] , UBN_CNN is used to extract the endocardial edges of the LV. UBN_CNN uses a non threshold Boolean function with nine variables to detect the edges corresponding to the upward and downward brightness overleaps. MVN_CNN nonlinear filter is used also in this approach to smooth echocardiographic images. In [16], improved Dempster and Shafer theory is used to fuse Fuzzy inference system, ANN and CNN edge detectors to get more accurate edge detection contour. Choy *et al.* [26] used the mathematical morphology, Temporal Information (TI) and Spatial Information (SI) to segment the 2D echocardiographic image sequence. To improve the initial contour in frame number *i*, the image information from frame number *i*-1 is combined with the initial contour in frame *i*. The authors tried by this technique to overcome the difficulty of poor image quality of echocardiographic images. Narang *et al* [27] used hybrid filters to extract to select and extract the region of interest (ROI) and then applying *K*-means to enhance the ROI. First step is the contrast enhancement and noise reduction is applied to the image. Second step, the image is segmented using thresholding. Third step is Robert's operator edge detector is applied. Fifth step is ROI is extracted using morphological operation. Last step is enhancing the ROI by *K*-means.

- **Shortcomings of Early Vision Techniques:**

Early vision techniques perform a static segmentation on single two-dimensional (2D) frames. The segmentation results are inconsistent with the dynamics of the cardiac cycle. Among other difficulties, these techniques could not solve the problem of dropout in echocardiography signals. Also, there is no provision in the system to correct any initial detection error due to noise or imprecise knowledge representation.

2.3 CONTOUR MATCHING APPROACH

Contour matching is a significant problem in computer visions with a variety of applications such as model based recognition and tracking. In these applications the two matched curves are usually very similar. Contour matching techniques are based on the assumption that for any distinguishable shape, landmarks can be consistently followed through a sequence of images. At the beginning, we need to find the initial correspondence between frames by comparing the segmented contours. Then, we choose the match that minimizes the metric, based on curvature difference in the optimization function. The problem is formulated as finding parameters that minimize a cost function. The cost function can be defined as the elastic energy which is needed to transform points on one curve at time *t* to points on the next curve at time *t*+1. Suppose we have two contours; C_1 and C_2, indexed by sampling point $\tau \in [0, N]$. We can define corresponding mapping functional $F_1(\tau)$ and $F_2(\tau)$ such that a displacement emanating from point $F_1(\tau)$ on C_1 specifies a point $F_2(\tau)$ on C_2.

$$Let\ F_2(\tau) = \tau + \delta, \quad F_1(\tau) = \tau \tag{2.3}$$

Where δ is small, then the energy matching is functional and will be as follows:

$$\begin{aligned}(F_1^*, F_2^*) &= \arg \min_{F_1, F_2} e(F_1, F_2) \\ &= \arg \min_{F_1, F_2} \frac{1}{2} \int_S \left[k_g(F_2) - k_f(F_1) \right]^2 d\tau \end{aligned} \tag{2.4}$$

Where *S* is the segment on C_2 used for matching, k_f is the curvature for any given point on the C_1 and k_g is the curvature of a candidate point within a set $G(\tau)$ of the nearest point on C_2. The functional *e* $(F_1, F2)$ is the bending energy required to deform points from contour C_1 to points on contour C_2 for a given index τ [28] .

J. McEachen *et al*. [28] presented an approach for tracking and quantifying the non-rigid, non-uniform motion of the LV endocardial on a point-by-point basis over the entire cardiac cycle on 2D cardiac image sequences. J. McEachen *et al.* built their approach

based on the assumption that recognition of the shape landmarks can be consistently tracked through a sequence of images. Given two LV contours C_i and C_{i+1} derived from successive image frames representing times t_i and t_{i+1} in a cardiac imaging sequence, the initial correspondences between frames is extracted by comparing the shape of contour segments. Next, the match that minimizes bending energy is chosen by the metric based on differences in curvature. McEachen *et al.* also in [29] addressed the problem of tracking LV endocardial motion from medical images. The approach is based on information over two spatial dimensions and time in formulating a displacement flow field of the LV wall viewed as a deformable contour. The approach consists of two stages. The first stage is comprised of shape-based matching and the second is a smoothing of the resultant vectors over pairs of successive contours. The authors used a least squares analysis to derive an analytic solution to the smoothing stage, while still constraining displacement vectors to the contour definitions. S. Yeo *et al.* in their paper [30] recovered and elucidated the left ventricular wall motion during isovolumetric contraction using a shape-based tracking approach. The LV surface properties are derived by local surface fitting and the point correspondences between successive time frames are determined using a thin plate bending model. J. McEachen *et al.* [31] presented a framework for temporal analysis of left ventricular (LV) endocardial wall motion. The harmonic estimation is utilized to model the periodic nature of cardiac motion. A flow vector computation method is used to define a relationship between image-derived, shape-based correspondences and set of correspondences. A recursive filter is then constructed which takes into consideration this relationship, as well as knowledge of temporal trends. The trajectories contrast markers implanted in the LV wall are compared with trajectories estimated by the filter. P. Bansod *et al.* [11]proposed a semi-automatic method to estimate the contour of the endocardial border of heart chambers in short axis view of 2 or 4 chamber and long axis view echocardiographic image sequences. This method is based on ellipse fitting and a subsequent radial search with gradient magnitude and direction. The multi frame guided local search employed the temporal information to recover the dropout as a refinement process. The procedure is evaluated with one manual contour drawn by an expert without evaluating other parameters like LV area. A Mishra *et al.* [32] algorithm for detecting the LV motion on a non-rigid shape approach utilized

an expansion and contraction of shape matched templates to optimize the correspondence in each level. The optimization process is done by using genetic algorithms.

- **Shortcomings of Contour Matching Approach:**

The choice of which matching criterion and which features to match can affect the tracking quality. After extended periods, the trajectories of these matches diverged from the trajectories of the markers, requiring a temporal constraint to correct for this issue. This approach did not provide any solution to echocardiography difficulties like contour missing parts.

2.4 SNAKE BASED APPROACH

Kass *et al.* [33] introduced the concept of active Contour Models (ACM), or Snake in his paper "Snakes: Active Contour Models". Snakes are used in the area of image processing to detect the object boundaries. Detecting the object boundaries by utilizing the low level image processing techniques (Sobel, Laplacian; Canny edge detection) is not successful. Following this technique, edges are not continuous (there are gaps between edges) and there is evidence of spurious edges due to noise. Snakes overcome these shortcomings by imposing desirable properties such as continuity and smoothness to the contour of the object, which means using prior knowledge for solving the problem of detecting the object boundaries. The snake model is modeled as parametric curve that evolves into a position where its energy function is minimized. The position of the snake is given by the parametric curve $C(s) = [x(s), y(s)]$ with $s = [0, 1]$. Kass *et al.* introduced the following energy functional for the Snake:

$$E_{Total} = \int_0^1 (E_1(c(s)) + E_2(c(s)))ds \tag{2.5}$$

Where

$$E_1 = \int_0^1 (\alpha \|c'(s)\|^2 + \beta \|c''(s)\|^2)ds \tag{2.6}$$

$$E_2 = \int_0^1 P(c(s))ds \tag{2.7}$$

E_1 is the internal energy term and E_2 represents the external energy term. The first term in the internal energy represents the elasticity and the second term represents the curvature. The influence of the two terms is controlled by the parameters α and β respectively. The external energy (image energy) attracts the Snake to the boundaries of the object in the images. The image energy here will be defined as follows:

$$E_2 = -\|\nabla I(x, y\|^2 \tag{2.8}$$

where I is the image function. Following this, the snake function will be minimized in the position with high gradient values.

Many authors exploited the Snake to segment and track LV from echocardiographic images. U. Bharali *et al.* [5] presented an unsupervised active contour tracking algorithm. The algorithm is fully automatic without any user interaction. The authors utilized multi-resolution image segmentation to initialize the contour in the first frame of the sequence. The output from the current frame was used as the initial contour to the next frame until the end of the sequence. The authors did not use any tracking methodology and they depended only on the snake output from one frame to another. By using this method, the snake cannot follow the movement of the LV because it does not have the ability to detect large displacement movements. Also the authors did offer any evaluation of their method. The approach of S. Malassiotis [34] is to first apply a Hough Transform (HT) to find the initial approximation at the first frame. The snake model is then applied to estimate LV boundaries. The PCA (Principle Component Analysis) is used in this approach to find the reduced ordered orthonormal basis of the LV deformations to constrain the motion of the snake. The authors did not provide any evaluation for their approach, V. Chalana *et al*. [2] designed a method based on an extension of active contour models to detect both epicardial and endocardial boundaries. The idea is to use temporal information to detect cardiac boundaries from echocardiograms by extending the original active contour model to three dimensions, because individual echocardiographic images often contain missing boundaries and the detection errors using a 2D model may propagate and increase further in the sequence. The approach of Sheng *et al.* [35] is based on taking aid from the neighbouring frames. These frames have consistent locations and shape that aid in segmentation process. To work with the constraining information provided by the neighbouring frames, the authors combined the

template matching with the conventional snake model. A multi-scale directional snake was proposed by J. Cheng *et al.* [36] to segment echocardiographic images. First, morphological operations were used to locate the left ventricular center point and region of interest. After that, a multi-scale directional edge map is applied to enhance snake performance. This step eliminates the initialization step, so Snake will propagate on this region only during deformation. By combining optical flow with snake, I. Mikic *et al*. developed their algorithm to extract the LV contour from echocardiographic image sequence [37]. Their technique incorporates the information on pixel velocities (optical flow) into the estimation of initial contour to enable tracking of LV endocardial contours. M. Berger *et al.* used a hierarchical approach to track the LV motion [38]. First, the authors computed a global estimation of the ventricular motion based on a parametric motion model with a small number of parameters. An optical flow is used to compute the LV motion. Then a fine tuning algorithm is applied to adjust the detection of the ventricular wall. After tuning, a conventional Snake is used to refine the detected contour. Cheng *et al.* [39] located the area of LV by using the watershed transform and morphological operations. This step is followed by Snake and multi-scale edge map detection to extract the LV endocardial boundaries.

- **Shortcomings of Snake Based Approaches:**

a) Snake when used for tracking by selecting the contour from the current frame as an initial position to the next frame fails to detect large displacements.
b) Snakes performance depends on the elastic forces and the local image features. This dependency makes the curve evolution not easily controlled and sensitive to noise or to image corruption. Snakes do not work well on low-quality data where noisy feature measurements attract it into noisy areas of the image because there is no constraint on valid deformations.
c) Snake's performance depends on the initialization process. Snake should be initialized very close to the required contour.
d) Snake has a difficulty to handle the topological changes.

2.5 LEVEL SET BASED APPROACH

The level set method was introduced by Osher and Sethian [40] as a solution to the shortcomings of the classical Snake. Let $C(p, t)$, defined as $\{(x, y, t)\}$ denote a family of closed contours generated by moving an initial contour $C_0(p, t)$ in the direction of normal vector N. Let F denote the speed function of the curvature k; thus the curve evolution equation will be written as:

$$\begin{cases} C(p,t) = F(k)N \\ C(p,0) = C_0 \end{cases} \tag{2.9}$$

The level set method represents the contour implicitly as the zero level set of a smooth, continuous scalar function $\phi(x, y, t)$ known as the level set function. The implicit contour at any time t is given by $C(p, t) = \{x, y | \phi(x, y, t) = 0\}$. By taking the derivative of $\phi(x, y, t) = 0$ w.r.t. time and space, the following equation results:

$$\begin{cases} \phi_t = -F(k)|\nabla\phi| \\ \phi(C_0(p,0) = 0 \end{cases} \tag{2.10}$$

This equation links the moving contours $C(p,t)$ with the evolving level set curves $\phi(x,y,t)$ [40]. For related work that utilized the level set method, C. Corsi *et al.* [6] utilized a level set method to detect and track LV boundaries through the 2D echocardiographic images sequence. The authors depend on the level set method only in their approach to segment and track the LV boundaries. In our work [16] , improved Dempster and Shafer theory is used to fuse edge and region based level set to detect the endocardial edge detection. Data fusion has great improvement in the performance of the framework when using more than one classifier in a detection system. In [41] , the LV contour is detected by MVN_CNN and UBN_CNN framework as mentioned in [25] then the area of the LV is extracted by using edge based level set. By using the MVN_CNN and UBN_CNN framework enabled us to extract the exact area of LV due to the powerfulness of MVN_CNN for noise removal and image smoothness and the ability of UBN_CNN to detect the edges of the LV. Cheng et al [42] employed Markovian level set to tackle the difficulties of echocardiographic images. The authors combined the MRP and the level set methods tighter. The MPR is used to handle the local statistics and level set to detect the LV topologies. Saini et al in [43] employed level set method based on a new Signed

Pressure Force (SPF) function based on Chan-Vese (CV) region based level set method. SPF is given by the following formula:

$$spf\ (I(x,y)) = \frac{I(x,y) - \frac{l_1 + l_2}{2}}{\max\left(\left|I(x,y) - \frac{l_1 + l_2}{2}\right|\right)}, x, y \in \Omega \tag{2.11}$$

where

$$l_1 = \frac{\int_{\Omega} I(x,y) H(\phi) dx dy}{\int_{\Omega} H(\phi) dx dy}$$

$$l_2 = \frac{\int_{\Omega} I(x,y)(1 - H(\phi)) dx dy}{\int_{\Omega} (1 - H(\phi)) dx dy}$$

Here, H(.) is Heaviside function.

- **Shortcomings of Level Set Based Approaches:**

a) The authors depend on the edge based stop criteria to stop curve evolution which cannot be guaranteed to stop the curve from leaking out of the LV true boundaries.

b) The authors used a fixed number of iterations, which will not guarantee the convergence.

c) There is no temporal and spatial coherence between frames to ensure robustness of the performance.

d) The authors did not mention any solution to signal drop out and missing parts of LV boundaries.

2.6 Optical Flow Based Approach

The Optical Flow (OF) of an image is defined as how parts of the image move with respect to the previous image. In 2D, the optical flow specifies how much each image pixel moves between adjacent images. There are many different methods to estimate the optical flow, which can be divided into correlation, energy, phase and differential based

methods. Most optical flow approaches are based on the assumption that image objects keep the same intensity value under motion for at least a short period of time.

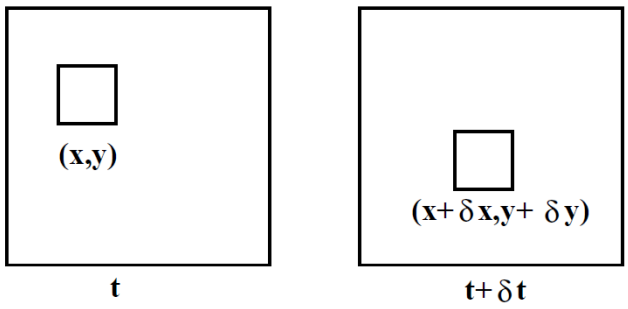

Figure (2.1) - The position (x,y,t) in the image is the same as at ($x+\delta x$,$y+\delta y$,$t+\delta t$)

Let $I(x,y,t)$ be the center pixel in $n \times n$ neighbourhood and moved by δx,δy in time δt to $I(x+\delta x,y+\delta y,t+\delta t)$. $I(x,y,t)$ and ($I(x+\delta x,y+\delta y,t+\delta t)$) are the same point in the image, then we have:

$$I(x, y, t) = (I(x + \delta x, y + \delta y, t + \delta t) \tag{2.12}$$

This assumption forms the basis of the 2D motion constraint equation as in Figure (2.1). The assumption is true for small motions, which means δx, δy and δt are small values. By using Taylor series expansion, we get the following equation:

$$I(x + \delta x, y + \delta y, t + \delta t) = I(x, y, t) + \frac{\delta I}{\delta x}\delta x + \frac{\delta I}{\delta y}\delta y + \frac{\delta I}{\delta t}\delta t + H.O.T. \tag{2.13}$$

H.O.T. is the Higher Order Terms, which are assumed to be small and can be ignored. By using Equation (2.12) and Equation (2.13), we get:

$$\frac{\partial I}{\partial x}\partial x + \frac{\partial I}{\partial y}\partial y + \frac{\partial I}{\partial t}\partial t = 0 \tag{2.14}$$

$$\frac{\partial I}{\partial x}\frac{\partial x}{\partial t} + \frac{\partial I}{\partial y}\frac{\partial y}{\partial t} + \frac{\partial I}{\partial t} = 0 \tag{2.15}$$

$$\frac{\partial I}{\partial x}v_x + \frac{\partial I}{\partial y}v_y + \frac{\partial I}{\partial t} = 0 \tag{2.16}$$

Where v_x and v_y represent the *x* and *y* image velocity components, we call them optical flow. $\frac{\partial I}{\partial x}$, $\frac{\partial I}{\partial y}$ *and* $\frac{\partial I}{\partial t}$ are the image intensity derivatives at (*x,y,t*). The above partial derivative equation can be written in this way:

$$(I_x, I_y).(v_x, v_y) = -I_t \tag{2.17}$$

here, $I_x = \frac{\partial I}{\partial x}$, $I_y = \frac{\partial I}{\partial y}$ and $I_t = \frac{\partial I}{\partial t}$.

or as:

$$\nabla I.\vec{v} = -I_t \tag{2.18}$$

where, ∇I is the spatial intensity gradient.

$\vec{v}$ is the image velocity or optical flow at pixel (x,y) at time t.

Equation (2.18) is known as (2D Motion Constraint Equation), which is one equation in two unknowns. To solve this problem we have to find another constraint that has a second different equation with the same unknowns [44] .

Many authors utilized optical flow to track LV motion. To track the heart motion in B mode echocardiography, N. Sahba et *al.* [45-47] combined local and global (CLG) optical flow with multi-resolution spatiotemporal spline moments to increase the accuracy and robustness of shear, rotation and wide range of motions that the optical flow techniques suffer from. The results demonstrate better efficiency with respect to other motion estimation techniques such as Lucas-Kanade, Horn-Schunck and the spatiotemporal affine technique. M. Unser *et al.* [48] presented a serial extraction of a myocardial boarder. The technique consists of three steps: image enhancement, template matching and boarder extraction. M. Sühling *et al.* [49] combined the Lucas–Kanade method of optical flow with a local motion model inside a sliding spatiotemporal window. The objective from using a local-affine model is to calculate the velocity in space which describes heart motions such as rotation, contraction, expansion and shear. A multiresolution strategy was used to improve the estimation of the motion. Y. Chunke *et. al*. [50] applied the Lukas-Kanade optical flow, which is a local gradient based method to analyze two echocardiographic image sequences. Chunke found that the applied motion can be clearly recognized when the local spatial constant window size is properly

selected. The authors also proposed a hierarchical improvement to solve the problem of contradiction between the motion blur and the sensitivity of the numerical differentiation to the noise. The good quality results from these improvements depend on the properly selected weight which determines the relation between the motion blur and the sensitivity to the noise. M. Berger *et al.* [38] used a hierarchical algorithm to outline the LV boundaries. The authors first computed a global estimation of the ventricular deformation. This global estimation is based on a parametric motion model that has a small number of parameters. The parameters are estimated from the velocity field that computed at all points on the LV contour. Secondly, a fine tuning is applied to the deformation to adjust the details. From the previous estimations, an active contour model is applied detect the LV outlines. G. Mailloux *et al.* [51] applied the Horn and Shunk optical flow method to track the heart motion through 2D echocardiographic images. The authors noted that they got good results but without any validation. In their paper, D. Boukerroui *et al.* [52] combined the similarity measure technique proposed by Cohen and Dinstein and the Singh block matching technique and also proposed a global optimisation scheme for the parameters estimation. The results from this combination showed a more effective block-matching algorithm in ultrasound sequences and the resulting optimisation improves the outcome in about 35% in comparison to the worst case. In this paper, the performance of the proposed block matching approach is demonstrated on B-mode ultrasound images. P. Baraldi *et al.* [53] evaluated the performances of three methods for evaluations of motion on synthesized 2D echocardiographic image sequences with features similar to real ones. The selected techniques are based on the computation of optical flow of the differential type and assume that the image brightness pattern is constant over time. The images were synthesized by simulating the process of echo formation, considering the interaction between ultrasonic fields and human tissues. Moreover, two different approaches were followed to generate the sequences. In the first approach, a known motion field was applied to the intensity distribution of the synthesized images. In the second approach, a known motion field was applied directly to the point scatterer distribution of the tissue. Good results were obtained by applying Lucas-Kanade and Horn-Schunck techniques to the sequences of the first type, while all the techniques produced large errors when applied to the other type of sequences. The

approach of A. Giachetti [54] for tracking LV is based on fast correlation optical flow. Initially, the contour is detected by a balloon active contour model, then LV contour is tracked with optical flow and snake based regularization.S. Riyadi *et al.* in their framework [55-57] extracted the profile of myocardium motion of the segmented boundary. By obtaining the optical flow between two consecutive frames, the inner boundary is extracted by the Canny operator and centroidal based searching method. The last stage is smoothing the extracted boundary. M. Suhling *et al.* [58] estimated the heart motion from 2D echocardiography sequences using the Lucas-Knande optical flow algorithm. In their work, Suhling *et al.* does not depend on the assumption of constant motion in the sliding window, instead they used a locally affine model that can account for dilation, contraction and shear motion of the heart. Suhling *et al.* also estimated the displacement vector at different scales. Hamou *et al.* tried to improve the performance of the deformable model (Snake) by using the optical flow as the external energy of the Snake. Using the optical flow as external energy can provide additional information to the Snake to improve the extract of more accurate contours. Q. Duan *et al.* [59] used optical flow to track the LV in the three dimensional echocardiography to extract the displacement field. G. Hamarneh *et al.* [60] used the optical flow to derive a new force from two consecutive frames. This new force will be combined to the Snake forces to assist the tracking of Snake to the desired dynamics.

- **Shortcomings of Optical Flow:**

a) Optical flow methods are well known for being sensitive to image noise.
b) Optical flow is based on the assumption that the object motion is not wide. From this, optical flow cannot capture or detect wide range motions.
c) Optical flow is highly computationally expensive.
d) Optical flow is highly dependent on whether the smoothness of velocity variation assumption holds.
e) Optical flow is crucially dependent on the accuracy of the initial estimates of the velocity components.

2.7 MRF Based Approach

A Markov Random Field is a graphical model in which a set of random variables have a Markov property described by an undirected graph. MRF is a principled approach for incorporating context information and domain knowledge. According to the Bayesian framework, the segmentation problem formula will be as:

$$P(x \mid y) = \frac{p(y \mid x)P(x)}{p(y)} \tag{2.19}$$

If we take the logarithm of both sides of Equation (2.19), then we will get the following equation:

$$\log p(x \mid y) = \log\ \mathrm{p(y|x)}\text{-}\log \mathrm{p(x)} + \mathrm{C} \tag{2.20}$$

which is the posterior log likelihood. To find the solution x (in this case, the maximum a posterior MAP) for a given measurement y, we simply minimize the log likelihood, which can be expressed in the following energy function:

$$E(x, y) = E_d(x, y) + E_p(x) \tag{2.21}$$

The constant C is ignored because its value has no effect during energy minimization. The first term in the energy function represents the data energy and measures the log likelihood where the data is observed given the unknown state x. The second term is the prior energy which works as smoothness energy. In image processing, the unknown x is the output pixels and y is simply the input pixels [61]. The following work has been carried out using MRF:

I. Herlin *et al.* [62] combined spatial properties and temporal properties to segment and track heart boarders in 2D echocardiographic image sequence under the MRF framework, which is used to model the energy function. The first frame is manually segmented. This manual segmentation is used to estimate the parameters of the model (energy function) to

be used for segmenting and tracking subsequent frames. I. Herlin *et al.* [63] used the Markov random fields and stochastic processes for the automatic selection of the parameters. The authors addressed the problem of initial segmentation by using grey level, texture and gradient information. A global energy function is minimized to get the regularization of the surface boundaries. N. Friedland *et al.* [64] presented an approach for detecting endocardial boundaries from 2D echocardiographic image sequences. The approach can be summarized into three steps. First the predetermined size window is decimated into another size after low pass filtering. Secondly the center of gravity is determined and an elliptical Hough Transform (HT) is performed to estimate the cavity boundaries. Thirdly, 64 radii are bounded by the high probability region and defined as a link in a 1-D, 64 member cyclic Markov random fields. A stochastic relaxation optimization (SA) is performed upon the MRF to bring the energy function to a global minimum. J. Dias *et al.* [65] presented a probabilistic model for endocardial and epicardial contour estimation in sequences where echocardiographic images are presented. The problem was formulated under the Bayesian setup. Contours are assumed two-dimensional, i.e., they have spatial and temporal indexes. For each temporal index, the contour is modeled as a noncausal first-order Markov random process. For each spatial index, the resulting process is assumed as a causal, first-order Markov random process. The physics of image generation and the heart morphology play a key role in building the image generation model; namely, the observed image pixels were modeled as Rayleigh distributed random variables with means depending on their positions relative to the contours. The MAP criterion is then applied to derive the contour estimates.

- **Shortcomings of MRF:**

  One of the shortcomings of MRF is the different parameters of the algorithm. Choices of parameter values are usually a major drawback of MRF modelling. Also MRF suffers from high cost of computation. The technique does not provide a solution to the signal dropout in echocardiographic images and missing parts of contours.

2.8 ACTIVE SHAPE MODEL BASED APPROACH

The Active Shape Model (ASM) is a parametric deformable model where a statistical model of the global shape variation, called a Point Distribution Model (PDM) is built from a training set. The ASM model detects the main variations in the training data using Principal Component Analysis (PCA). By finding the variations, the ASM has the ability to automatically recognize the contour of an object. A brief description for constructing the PDM using a principal component analysis (PCA) is given by [66].

The shape is represented by choosing n-points (features) from training instances of the shape

$$X = (x_1, y_1, ..., x_{n-1}, y_{n-1}, x_n, y_n)^T \tag{2.22}$$

- Aligning the shape instances

The Procrustes algorithm is used so that the sum of distances to the mean of each shape is minimised $\sum_{i=1}^{m} (x_i - \bar{x})^2$.

- Compute the mean shape

$$\bar{x} = \frac{1}{m} \sum_{i=1}^{m} x_i \tag{2.23}$$

- The deviation of each shape from the mean shape:

$$d\bar{x}_i = x_i - \bar{x} \tag{2.24}$$

The estimation of the covariance matrix can now be written as:

$$\Sigma = \frac{1}{m} \sum_{i=1}^{m} dx_i \, dx_i^T \tag{2.25}$$

- Compute the eigenvectors (p_i) and the eigenvalues(λ_i)
- The matrix P is then built from each eigenvector ordered in descending order of the corresponding eigenvalues.

$$P = [p_1 ... \quad p_{2n}] \tag{2.26}$$

- A shape instance can then be generated by deforming the mean shape by a linear combination of eigenvectors:

$$x = \bar{x} + Pb \tag{2.27}$$

- PCA can be applied to the training set to reduce the number of parameters in the model. Choose *t* so that:

$$\sum_{i=1}^{t} \lambda_i \geq g \sum_{i=1}^{2n} \lambda_i \tag{2.28}$$

A suitable value for *g* is 0.98.

- Approximate any instance of the shape, including the training instances, by projecting onto the first *t* eigenvectors:

$$x = \bar{x} + \sum_{i=1}^{t} b_i p_i \tag{2.29}$$

The weight vector b is identified as the characteristic of this instance shape

$$b = [b_1, ..., b_t]^T \tag{2.30}$$

- Varying the weights b_i enables us to explore the allowable variations in the shape.
- A model instance is defined by its model vector *T* as following:

$$T = \{t_x, t_y, s, \theta\} \tag{2.31}$$

where t_x, t_y is translation, s for scale, and θ for rotation.

- The model instance in the image will be as follows:

$$x = T(\bar{x} + \sum_{i=1}^{t} b_i p_i) \tag{2.32}$$

- After selecting *K* points in the image, the boundaries of the object will be detected by minimizing the following equation:

$$\left| K - T(\bar{x} + \sum_{i=1}^{t} b_i p_i) \right|^2 \tag{2.33}$$

Many authors employed the ASM to detect and track LV boundaries. To model and segment spatio-temporal shapes (ST-shapes), G. Hamarneh *et al*. [67] extends 2D active shape models to 2D + time. The model builds the statistical of ST-shape parameters that

describe the principal modes of variation plus the constraints on the allowed variations. The active approach is used for segmentation after an initial ST-shape is deformed to better fit the shape. D. Comaniciu [68] introduced an approach that incorporates other information about the image in the tracking process. The authors proposed a fusion formulation in the information space for robust shape tracking, optimally resolving uncertainties from the system dynamics, heteroscedastic measurement noise, and subspace shape model. K. Leung *et al.* [64, 69] employed the ASM to classify the heart wall motion. J. Nascimento *et al.* [70] used ASM with bank of nonlinear filters to deal with measurement uncertainty to attenuate the influence of outliers (false edges).

- **Shortcomings of ASM:**

The efficiency of ASM directly depends on the comprehensive object variations in the training set and a suitable initialization. The obtained model changes only in the available variations in the training set. All changes outside of the training set are not covered by the model. The initial shape which easily affects the final result is another challenging problem. If the initial shape is not suitable, the final result will not be satisfactory. Another disadvantage to ASM is that it only uses data around landmarks and does not utilize all available grey information across the object, meaning that it yields less reliable results.

2.9 Active Appearance Model Based Approach

The Active Appearance Model (AAM) is a generalization of the widely used Active Shape Model approach, but AAM uses all the information in the image region covered by the target object, rather than just the near modeled edges. AAM combines a statistical model of the shape and grey-level appearance of the object of interest. When the image is matched to AAM, this process includes finding the model parameters that minimize the difference between the image and a synthesized model example.

AAM was introduced by Cootes *et al.* [71] as an improvement to shortcomings of ASM. The following steps illustrate the model operations:

- Create the distribution model PDM. The same steps are followed as in ASM (Shape model).

$$x = \bar{x} + Pb \tag{2.34}$$

- Create the appearance model:

$$g = \bar{g} + p_g b_g \tag{2.35}$$

- Warp each image in the training set, so each control point matches the mean shape.
- Find the optimal shape parameters p and appearance parameters λ to minimize the difference between the warped-back appearance *I(W(p))* and synthesized appearance

$$E_a(p,\lambda) = \left\| A_\lambda - I(W(p)) \right\|^2 \tag{2.36}$$

J. Bosch *et al.* and S. Zhou *et al.* employed AAM to segment and track LV.

- **Shortcomings of AAMs**

a) The large number of parameters makes this process difficult.

b) If the distribution is disjunctive or skewed, the model may generate implausible intermediates or may fail to cover the full range of variability.

c) AAM is not suitable for highly deformable objects. Due the wide variety of heart shapes for different people and different ages, at various degrees of good and poor health; the shape and movement of the heart can be completely different. Depending on the training data base, AAM cannot recognize a new shape or a new movement that is not already included in the training data set.

2.10 BLAKE FRAMEWORK

G. Jacob *et al.*in their papers [72-74] utilized dynamic contour algorithm introduced by Blake [75] to track and evaluate an LV endocardial border. A dynamic contour tracker is based on a linear Kalman filter technique, where a model and measurements are combined together. The model is spatiotemporal and contains two stages. The first stage is a deformable model describing the deformations and a motion-model describing the temporal properties of the contour. The second stage is the measurement. G. Jacob *et al.*used edge detection to find the LV borders by employing a normal displacement technique, which detects the edges by searching for edge pixels in the normal direction of

the LV contour, as predicted from the motion model. F. Orderud *et al.* [76-79] used the same approach of G. Jacob *et al.* for the 3D echocardiography and with EKF instead of a linear Kalman filter.

- **Shortcomings of the Blake Framework**

G. Jacob and F. Orderud followed the Blake framework by using a simple edge detection technique in the measurement stage to find the edges in the normal direction to the surface of LV contour, as predicted from the motion model. This technique will lead to poor results due to difficulties mentioned regarding echocardiography ultrasound images. Another disadvantage is that the normal displacement technique will search in the normal direction only, whereas the real edge may be located in a different position outside of the predicted LV contour.

2.11 FEM AND LV TRACKING

FEM is used in literature to study the heart, especially the LV motion and mechanical properties. For LV motion tracking, I did not find any work relating to LV tracking from 2D or 3D echocardiography image sequences. For other modalities (MRI, CT scan, X-ray and MRI), FEM was used only to reconstruct the LV or the heart shape after extracting the LV boundaries using deformable models or other techniques.

a. CT scan and FEM

T. McInerney and D. Terzopoulos [80] tracked the LV surface motion during the cardiac cycle using physics based approach. The authors used CT images to estimate the LV surface images. A dynamic balloon model (spherical shape thin plate) under the tension surface spline is used to deform elastically to fit the image data. By means of internal force estimated from the elastic properties of the spline and the external forces that are extracted from the image data, the fitting process is done. FEM is employed to reconstruct the LV shape during the cardiac cycle.

b. X-Ray and FEM

Choi and Kim [81] tracked the LV motion in the cardiac cycle through the X- ray angiographic images. The framework, based on a 3D deformable model that consists of a

non-rigid body that deforms around a reference shape, is obtained from the previous image. The FEM is used here to reconstruct the shape of LV in 3D.

c. MRI and FEM

Young *et al.* [82] tracked the stripe motion tMRI images starting from the given locations of the tagging planes of the undeformed shape and the 3D locations of the stripes in the deformed shape. The authors then calculated the displacement for all the tracked stripes. FEM is used in this work as the 3D template for the 16 shapes of the heart that represent the cardiac cycle. The framework has a large error (16%) due to the inability to approximate the cylindrical geometry and the displacements. The authors did not evaluate their work. J Park *et al.* [83] tracked the systole phase of the cardiac cycle from MRI images. The data is extracted from the image and rigid body motion is used to simulate the translation and rotation. The Lagrangian dynamics model with FEM is used to simulate the deformation by using the image data. C. Conti *et al.* [84] developed a semi-automatic framework to track heart boundaries for the MRI image sequence. Deformable models are used to detect the heart boundaries and FEM is used to calculate the strains from the image data. X. Wang *et al.* [85] reconstructed the LV motion from tMRI image sequence using deformable models and FEM. The intersection of the three tagged planes with the intersection of the LV boundaries and the tagged planes of the LV area is segmented and interpolated onto mesh vertices. From the extracted image data, FEM is used to reconstruct the LV shape at each image. X-rays and CT scans have radiations and are therefore not suitable for heart disease patients. MRIs use magnetic fields and radio waves to view the heart anatomy, which can cause series problems for some patients [86]. MRIs can cause malfunctions to cardiac pacemakers and insulin pumps and also can cause panic attacks to patients due to loud noises emanating from the machines [87]. To avoid potential shortcomings in the computer vision techniques, there are correction steps to avoid any errors in the segmentation steps. Also, there is no spatial and temporal coherence between image sequences. The reconstruction step of the LV by FEM depends completely on the previous process of the segmentation, where the image data is used to draw the LV shape.

2.12 SUMMARY

In this chapter, the review to the approaches that have been used to detect and track the LV boundaries is introduced. The approaches are classified into 9 categories depending on the technique that used in the approach. A brief introduction about each technique is given along with the shortcomings of the utilized approach. A brief explanation about using the FEM with other modalities is mentioned for tracking and reconstructing the LV shape during the cardiac cycle.

CHAPTER 3 MEDICAL BACKGROUND

3.1 INTRODUCTION

As mentioned in Chapter 1, the objective of this thesis is to track and detect the LV boundaries during the cardiac cycle. The approach is to utilize LV mechanics with deformable models. To achieve this objective and to use the LV mechanics, some knowledge about the heart anatomy and the stages of the cardiac cycle during its various activities phases is very important. Also, knowing the LV structure and understanding its mechanics are essential, necessary steps to reach the target and be able to use the knowledge gained in the resulting framework.

3.2 HEART ANATOMY

The human heart works as a mechanical pump that receives low pressure blood from the venous system and ejects it with higher pressure into the arterial system [88]. The heart consists of four chambers, left and right ventricle and left and right atria with a septal that separates the left and right chambers as illustrated in Figure (1). A muscular tissue known as myocardium encompasses the four heart chambers. The myocardium works in a sequence of contractions and relaxations. Out of the four chambers in human heart, Left Ventricle (LV) is the strongest. The force needed to circulate blood through the body is provided by its muscular walls which on average are only one centimeter thick [88]. The heart has four valves which regulates the flow of the blood between the chambers. The valves can be classified as follows:

- The tricuspid valve: controls blood flow between the right atrium and right ventricle.
- The pulmonary valve: regulates blood flow from the right ventricle into the pulmonary arteries.
- The mitral valve: passes blood from lungs through the left atrium into the left ventricle.
- The aortic valve: passes blood from the left ventricle into the aorta [88].

3.3 Activities During the Cardiac Cycle

The cardiac cycle can be defined as the period of time required for one heart beat and can be divided into two stages [89]:

Diastole: represents the time when the ventricular are filling with blood and a short period before filling. In this stage the left and right atria contract to eject blood into the ventricles.

Systole: is the time when both ventricle contract to eject blood to the body. No blood enters the ventricles while blood is continuing to enter the atria, Figure (2) [89, 90].

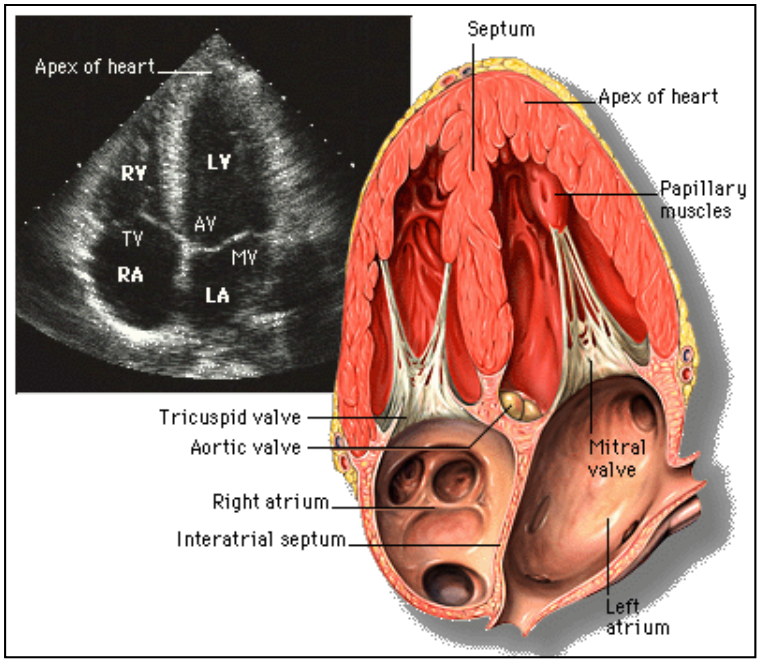

Figure (3.1) Heart Anatomy [91]

3.4 Phases of the Cardiac Cycle

The cardiac cycle is divided into seven phases that illustrate in detail the activities that occur during the diastole and systole stages as shown in Figure (3) [89, 90] .A brief description about each phase follows:

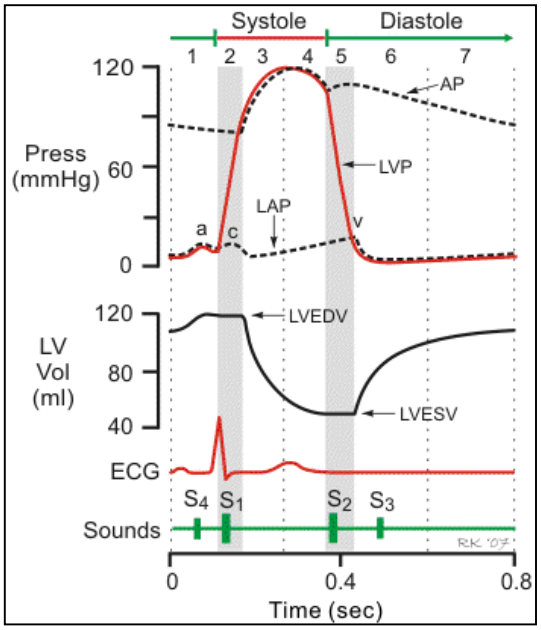

Figure (3.2) Systole, diastole and LV volume during the cardiac cycle [89, 90]

- **Phase One: Atrium Contraction**

[AV Valves Open - Semilunar Valves Closed]

In the first phase, the atrium muscles are contracted due to the electrical depolarization of the atria. This contraction causes the pressure inside the atriums to increase. At this moment, the atrioventricular (AV) valves are open which leads to a rapid flow of blood into the ventricles. The atrium pressure starts to decrease at the end of the contraction which leads to the valves to float upward before closure. At this phase, the ventricular have the maximum volume which is known as End Diastolic Volume (EDV) [89, 90].

- **Phase Two: Isovolumetric Contraction [All Valves Closed]**

In the second phase, the intraventricular pressure is greater than the atrium pressure that causes the AV valves to close. Ventricular contraction triggers the contraction of the papillary muscles also stimulated from the contraction of ventricular that prevents the blood to leak from the AV valve.

During this phase, all valves are closed and the pressure in the ventricular pressure increases quickly. There is no ejection, so the volume of ventricular remains as it is which is known as isovolumetric contraction [89, 90].

- **Phase Three: Rapid Ejection [Aortic and pulmonary Valves Open - AV Valves Remain Closed]**

The third phase represents the time when the pressure inside the ventricles is over the one inside the aorta and pulmonary artery. This leads the aortic and pulmonary valves to open causing a rapid flow of the blood from ventricular into the aorta and pulmonary arteries. The ejection of the blood occurs because the blood energy in the ventricle is more than blood energy in the aorta [89, 90].

- **Phase Four: Reduced Ejection**

[Aortic and Pulmonary Valves Open- AV Valves Remain Closed]

In the fourth phase, the rate of blood ejection becomes less due ventricular repolarization that leads to ventricular active tension to go down with the ventricular pressure too [89, 90].

- **Phase Five: Isovolumetric Relaxation [All Valves Closed]**

The fifth phase is when isovolumetric relaxation occurs. The aortic and pulmonary valves are closed because the intraventricular pressures are less. There is no change in the ventricular volume because all valves are closed. The remaining blood in the ventricular is known as the End-Systolic Volume (ESV). The difference between the end-diastolic and the end-systolic volumes is known as Stroke Volume (SV) [89, 90].

- **Phase Six: Rapid Filling [AV Valves Open]**

The sixth phase is when the ventricular start filling. This occurs due to the intraventricular pressures is below the pressure in the atrium and the AV valves become open. While the ventricles under relaxation, the pressure inside them is going down until they completely relaxed, after that intraventricular pressures rise because they fill with blood from the atria [89, 90].

- **Phase Seven - Reduced Filling [AV Valves Open]**

The last phase is when the ventricles continue to fill with blood and their volume will increase. The expansion of the volume causes the intraventricular pressures to rise and to reduce the pressure gradient across around the AV valves. The result will be the rate of filling becomes less [89, 90].

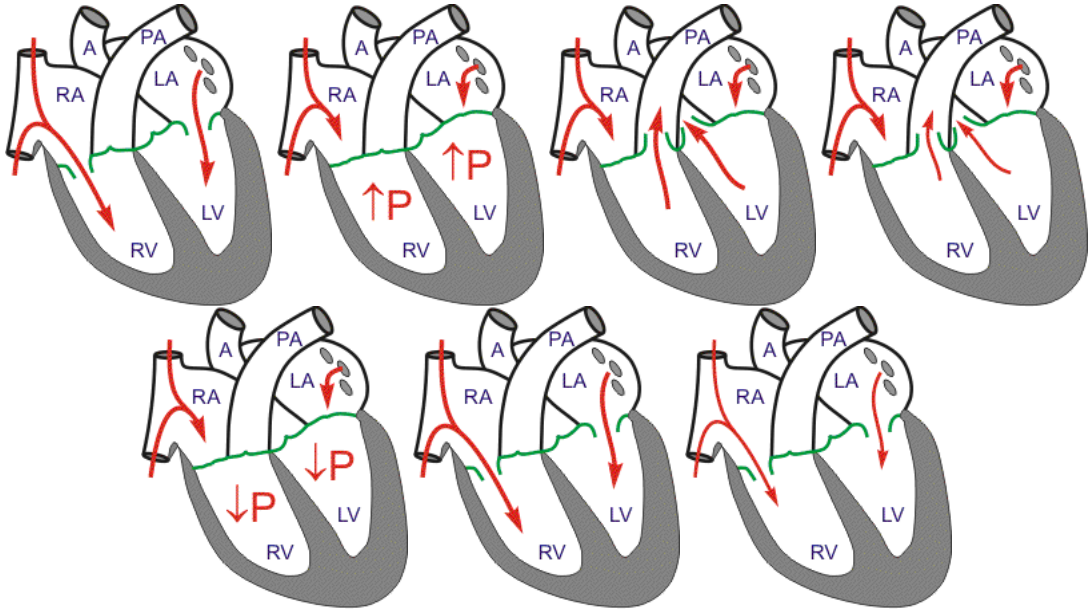

Figure (3.3) The seven phases of the cardiac cycle starting from left to right respectively [89, 90]

3.5 Geometry of Left Ventricular

The normal ventricular is usually visualized mentally as ellipsoid. The long axis extends from apex to base. Due to the posterolateral wall and the anterior wall, the short axis cross section does not appear in a circular geometry, Figure (3.4) [91]. The papillary muscles and trabecula cause an extremely irregular shape to the endocardial surface. The LV wall also has irregularity in its thickness. The LV wall thickness at septum is less thick than the posterolateral wall [92].

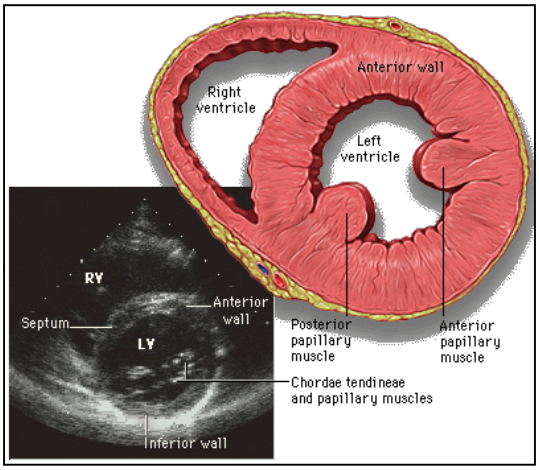

Figure (3.4) Short axis view [91]

3.6 LV Pressure Volume Relationship

There are many advantages to displaying left ventricular pressure (LVP) as a function of left ventricular volume (LVV) on a pressure – volume diagram. This is accomplished by plotting the measured LVV on the x-axis and the measured LVP on the y-axis for one cardiac cycle. This plot forms a loop. This loop is called the Pressure-Volume loop (PV loop) where the PV points go around the loop in a counter clockwise direction as the time proceeds [89].

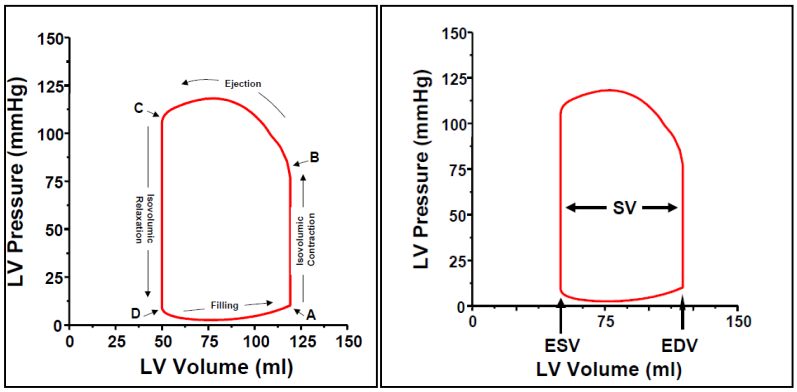

Figure (3.5) LV Pressure and volume relationship (LV Loop) [89]

3.7 Physiological Measurements Retrievable From the Pressure Volume Loop

As mentioned above, the PV loop shows the relation between intraventricular pressure and volume throughout the cardiac cycle. From this plot, the cardiologist can ascertain values of several parameters and variables of physiological importance. If we picked out the maximum volume from the volume axis, we will have the End Diastolic Volume (EDV) which represents the ventricular volume at the end of the cardiac cycle. The minimum volume is known as the End Systolic Volume (ESV), which represents the ventricular volume at the end of the ejection phase. The ratio difference between EDV and ESV is the stroke volume (SV), which is the amount of blood ejected during the cardiac cycle. The ratio between SV and EDV is known as the Ejection Fraction (EF), which is the most commonly used index of contractility [89].

$$EF = \frac{EDV - ESV}{EDV} * 100 = \frac{SV}{EDV} * 100 \tag{3.1}$$

3.8 Myocardium Structure

The heart resides inside a special cyst called the pericardium, which consists of two layers; fibrous and serous. The serous also has two layers, which are the visceral and parietal layers. The fibrous has a soft and lubricated lining, which protects the heart from infection and gives free movement to the heart [10].

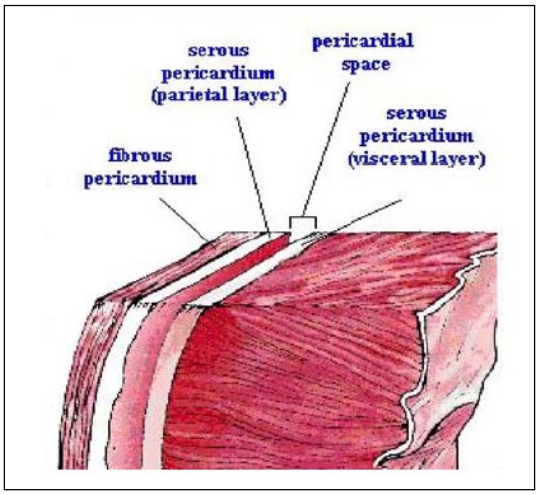

Figure (3.6) Structure of pericardial sac [92]

The epicardium, myocardium and endocardium are the three layers that make up the ventricle wall. The endocardium is the inner layer lining of the cavities, which also holds the valves of the heart and the tendons that carry the valves. The epicardium is the outer layer, which consists of connective tissue and a serous surface. The most important layer is the myocardium, which enables the ventricle to contract and pump the blood to the body [93].

The myocardium tissue consists of layers of interconnected sheets separated by cleavage planes. Each sheet in the myocardial tissue is formed by three to four cells connected together by extracellular matrix collagen, known as endomysial collagen. The sheets of the myocardium are coupled together by the perimysal collagen network [10].

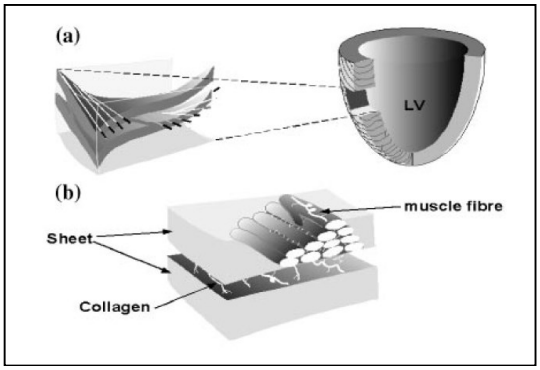

Figure (3.7) Schematic of fibrous sheet structure of cardiac tissue [94]

Figure (3.8) illustrates the representation of the microstructure using rectangular Cartesian axes. The first axis is the fiber axes. The second is the sheet axis and the third is the sheet-normal axis. The three material axes are used in the passive elasticity, while only the fiber direction is used in the continuum mechanics [94].

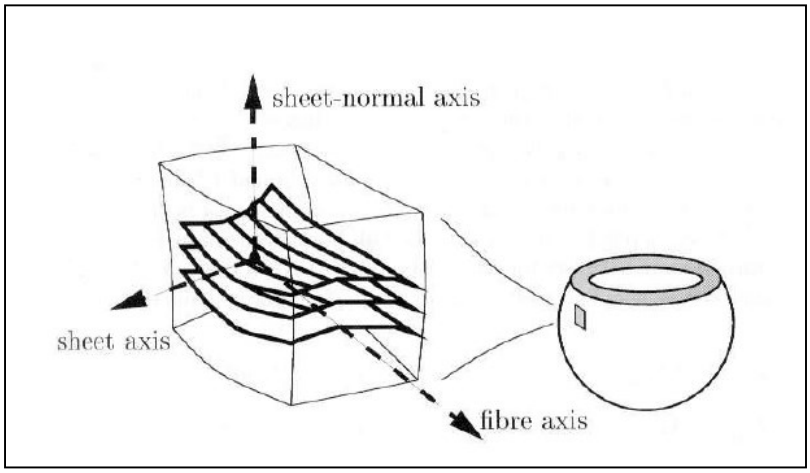

Figure (3.8) The local microstructure represented as Cartesian axes [94]

3.9 SUMMARY

Chapter three gives a brief overview of the medical background of the heart. The heart anatomy introduces the chambers and valves with their functions. The cardiac cycle and the activities during the seven phases are summarized. The quantities that used in the LV measurements are mentioned. The relationship between the pressure and volume in the LV is also presented, along with the measurements that can be retrieved from it. The structure of the heart muscles is given with a focus on the myocardium.

CHAPTER 4 BIOMECHANICAL MODEL, FIELD BOUNDARY ELEMENT METHOD AND FINITE ELEMENT METHOD

4.1 INTRODUCTION

Some biological tissues are subjecting to a large deformation in physiologic activity [95, 96]. Large deformation can be defined as deformations greater than 3 - 5% strain. Small deformation linear strain tensors can be used only in cases of small deformations. Cardiac cells change in length by over 20% during a normal heart beat, so the mechanical analysis must be based on a finite deformation elasticity theory [94]. During the cardiac cycle, myocardial deformation is produced as a result of longitudinal and circumferential motion, which is accompanied by thickening or thinning in the radial dimension. This deformation is quantified by the strain (E). At the end of diastole, myocardial length and thickness are at baseline, while during systole, longitudinal and circumferential shortening give negative strain values, reaching their minimum negative values. At the beginning of the diastole, the strain backs up to a less negative value and when the ventricular completes filling, the strain backs up to baseline, Figure (4.1) [97].

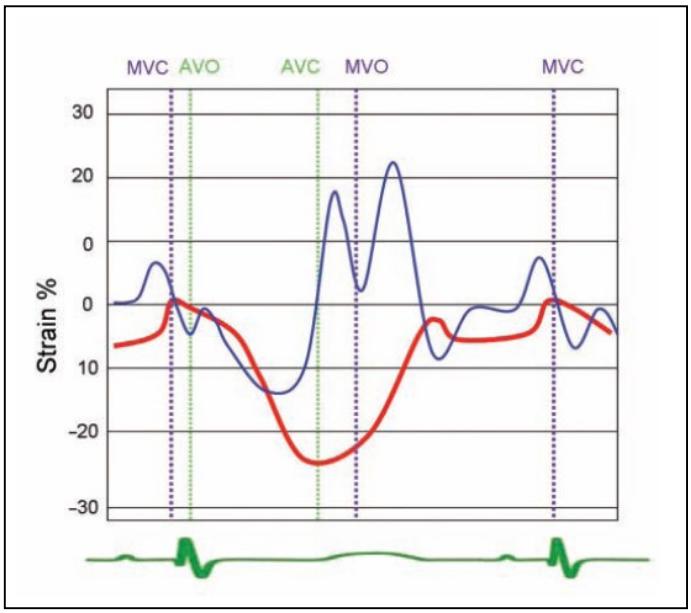

Figure (4.1) - Strain and strain rate during one cardiac cycle [97]

When a force is acting on a deformable object, a displacement field results in which each point moves a certain amount depending on its position in the object relative to the

applied force and on the mechanical properties of the object. Strain tensors are defined in terms of displacement gradients using kinematic relations [98].

The accurate myocardial mechanics model can simulate the heart wall motion during the diastolic (relaxation) and systolic (contraction) stages of the cardiac cycle. LV deformation can be determined through a model of the mechanics of myocardium. The BioMechanical (BM) model based on finite deformation elasticity and solving the resultant functional of the model by utilizing Field Boundary Element Method (FBEM) and Finite Element Method (FEM) is presented in this chapter.

4.2 MATERIAL BEHAVIOR

Due to the intra- and extra-vascular fluid displacements that occur throughout the contraction, the myocardial tissue is characterized as a highly anisotropic and weakly compressible material [99] . The material behaviour of myocardium is time dependent in that it varies through the cardiac cycle. Anisotropy, which is due to the alignment of the contractile elements of the tissue, makes the behaviour of the material directional dependency while applying the loads. The fiber orientation in the myocardium is highly complex with regional variability, making it challenging to incorporate anisotropy into the mechanical model of the LV. Instead, simplified transversely isotropic material models with different strain energy functional and material parameters have been used to create constitutive equations of the LV. The advantage of assuming the myocardium tissue as a transversely isotropic material is that, the strain energy function can be determined directly from the experimental data [100, 101]. Recently, orthotropic material models for myocardium were also proposed. The problem with the assumption of orthotropic material, the experimental data are not adequate to determine the strain energy functional and the associated material constants without further assumptions [102, 103].

4.3 CONTINUUM MECHANICS

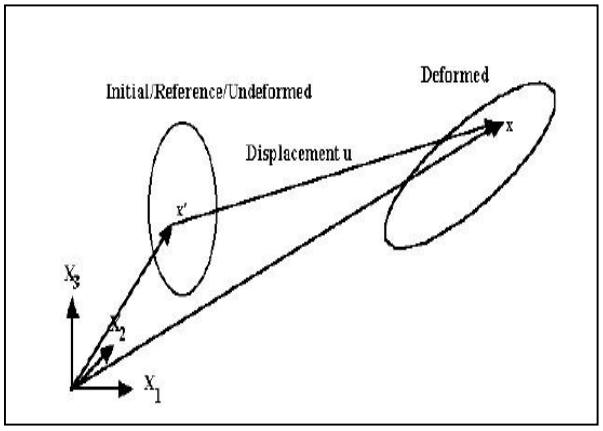

Figure (4.2) –Un-deformed body, deformed body and displacement [104]

The first step in measuring of large deformation is to establish the relation between the un-deformed and deformed shapes of the LV. The un-deformed shape is the state of the LV in 3D space before applying the loads while the deformed shape is the location and shape of the LV after applying the loads. An illustration of the relationship between the un-deformed and deformed configurations is shown in Figure (4.2) [104].

It is assumed that there is one to one mapping between the un-deformed R_0 to the deformed R_t, so that for every point of the body we can write:

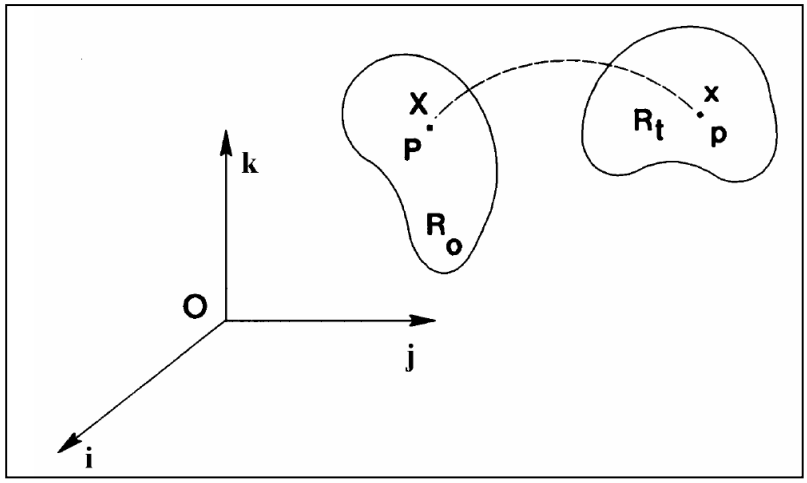

Figure (4.3) – Movement of one point from reference to deformed body [104]

$$x = x(X, t) \tag{4.1}$$

Furthermore, this mapping can be assumed invertible so that:

$$X = X(x, t) \tag{4.2}$$

For physically realistic problems the Jacobian description of the transformation can be written as:

$$J = \det\left[\frac{\partial x_i}{\partial X_j}\right] \tag{4.3}$$

But must not be zero for t>0.

The relation between the position vectors in the un-deformed and deformed shapes can be obtained by vector addition and written directly as follows:

$$x = u + X \tag{4.4}$$

From (4.4) we can define the deformation gradient tensor as:

$$dx = FdX \tag{4.5}$$

Or with respect to the components, as:

$$F_{ij} = \frac{\partial x_i}{\partial X_j} \tag{4.6}$$

Now, the relation between displacement and deformation gradient tensor can be derived as follows:

$$\begin{aligned} x &= u + X \\ dx &= du + dX \\ F &= grad\ \text{u+I} \\ \text{F}_{\text{ij}} &= \frac{\partial u_i}{\partial X_j} + \delta i_j \end{aligned} \tag{4.7}$$

The deformation gradient tensor characterizes the state of motion and deformation in the neighborhood of any point of the body [104].

The right Cauchy-Green tensor is as follows:

$$C = F^T F \tag{4.8}$$

The stretch ratio λ is defined as:

$$\lambda = \sqrt{N.C.N} \tag{4.9}$$

Where N is the unit vector

A further useful tensor is the Green-Lagrange strain tensor, which is defined as:

$$E = \frac{1}{2}(C - I) \tag{4.10}$$

where I is the unity matrix

Or in terms *of displacement*

$$E_{ij} = \frac{1}{2}\left[\frac{\partial u_i}{\partial X_j} + \frac{\partial u_j}{\partial X_i} + \frac{\partial u_k}{\partial X_i}\frac{\partial u_k}{\partial X_j}\right] \tag{4.11}$$

The quadratic term, which is the product of the displacement gradients, is the source of the geometrical nonlinearity in kinematical relations. The linear strain is given by the following equation:

$$\mathrm{e}_{ij} = \frac{1}{2}\left[\frac{\partial u_i}{\partial X_j} + \frac{\partial u_j}{\partial X_i}\right] \tag{4.12}$$

If *df* denotes the infinitesimal force acting on surface element $d\boldsymbol{S}$, we introduce the first Piola-Kirchhoff (1st PK) stress tensor by writing:

$$\sigma(X,t) = \frac{df}{dS} \tag{4.13}$$

W(F), known as a strain–energy function that is a single-valued function of the deformation gradient tensor ***F*** at any point of the body and any time**,** is independent of the rate of deformation or its history. *W* is the internal mechanical energy due to deformation that is stored in the body [104].

The first PK stress tensor can be derived from the strain-energy function:

$$\sigma = \frac{\partial W(F)}{\partial F} \tag{4.14}$$

The strain energy function can be represented by right Cauchy deformation tensor (*C*), by (*E*), or by invariants of right Cauchy deformation tensors (I_1, I_2, …). We denote these functions by *W(F) , W(C), W(E)* or $W(I_i)$.
Then S and σ will be defined as follows:

$$\sigma = 2F\frac{\partial W(C)}{\partial C}$$
$$S = 2\frac{\partial W(C)}{\partial C} = \frac{\partial W(E)}{\partial E} \tag{4.15}$$

If strain invariants are used, then *W* will be as follows:

$$W = W(I_1(C), I_2(C), I_3(C))$$
$$I_1(C) = trC$$
$$I_2(C) = \frac{1}{2}\left[(trC)_{28} - trC^2\right] \tag{4.16}$$
$$I_3(C) = \det C = J^2$$

The second Piola-Kirchhoff (2nd PK) stress tensor will be redefined as follows:

$$S = 2\sum_{i=1}^{3}\frac{\partial W(C)}{\partial I_i}\frac{\partial I_i}{\partial C} \tag{4.17}$$

If the material is incompressible, then J=1 and the S will be defined as follows:

$$S = -pC^{-1} + 2\frac{\partial W(C)}{\partial C} \tag{4.18}$$

The 1st PK stress tensor σ can be found from 2nd PK stress tensor as follows:

$$\sigma = FS \tag{4.19}$$

4.4 TRANSVERSELY ISOTROPIC MATERIAL

Transversely isotropic material can be defined as a material that exhibits a preferred direction, where the material properties depend on this direction and the response of the material along directions which are normal to this direction is isotropic Figure (4.4) [103].

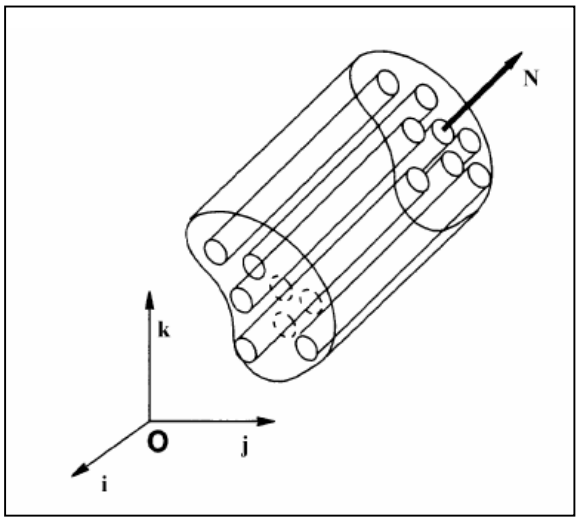

Figure (4.4) transversely isotropic material [103]

In the transversely isotropic material, the strain-energy function depends on ***C*** and on the preferred direction ***N***. In other words, if the material undergoes deformation, the vector ***N*** will deform with the body [99, 105]. The strain energy function of transversely isotropic material will be as follows:

$$W = W(C, N \otimes N) \tag{4.20}$$

W will be function of $I_1(C)$, $I_2(C)$, $I_3(C)$, $I_4(C)$ and $I_5(C)$ as following:

$$W = W\left[I_1(C), I_2(C), I_3(C), I_4(C, N), I_5(C, N)\right]$$

where

$$I_4(C, N) = N.C.N$$

$$I_5(C, N) = N.C^2.N \tag{4.21}$$

Then, the second PK stress tensor will be as follows:

$$S = 2\frac{\partial W(C, N \otimes N)}{\partial C}$$

$$S = 2\sum_{i=1}^{5} \frac{\partial W(C, N \otimes N)}{\partial I_i} \frac{\partial Ii}{\partial C} \tag{4.22}$$

4.5 CONSTITUTIVE EQUATION

A constitutive equation is a mathematical model that describes the relationship between stress and strain. Constitutive equations consist of two parts; one part is the unknown constants or material properties, which should be found experimentally [104]. The other part is the measures of deformation which may be a linear or nonlinear deformation.

To develop a constitutive equation for the tissue mechanics, some assumptions should be taken into account due to the complexity of this kind of mechanics.

Essentially, it is not possible to develop a constitutive equation that will precisely model the tissue behavior. To develop a constitutive equation for modeling a tissue, there should be a balance between the ability to accurately mimic the tissue behavior and the ability to obtain a constitutive equation simple enough to experimentally determine the material properties and numerically solve the equations [104].

a. LV Constitutive Equations:

To track the LV movement, our work depends on the Lin-Yin model [14] for the constitutive equation based on hyperelastic material theory. In this model, the strain

energy potential W is divided into two components: one is passive (W_{pass}), and the other is active (W_{active}). Lin *et al.* [14] performed multiaxial tests using a similar protocol as Humphrey *et al.* [100, 101] on passive and activated specimens. To reduce the passive parameters from 14 to 5, Lin *et al.* [14] used an exponential function instead of a polynomial function. The passive strain energy function is given as follows:

$$W_{pass} = c_1(e^{Q} - 1)$$
$$Q = c_2(I_1 - 3)^2 + c_3(I_1 - 3)(I_4 - 1) + c_4(I_4 - 1)^2 \quad (4.23)$$

where, c_1, c_2, c_3 and c_4 are the material property parameters that are determined experimentally. Lin *et al.* found that the active stress-strain responses were more linear than the passive ones, which indicated that both active and passive phases should have different kinds of materials that lead to establishing different strain energy functions to describe their behavior. The polynomial form of the active strain energy function which fit the experimental data is given in the following form:

$$W_{active} = c_5 + c_6(I_1 - 3)(I_4 - 1) + c_7(I_1 - 3)2 + c_8(I_4 - 1)2 + c_9(I_1 - 3) + c_{10}(I_4 - 1) \quad (4.24)$$

c_5, c_6, c_7, c_8, c_9 and c_{10} are material property parameters determined experimentally. Table (4.1) shows the values that are used for each material parameter. The material properties are given in (g/cm^2).

Table (4.1) – Values of material properties

Material parameter	Value (g/cm^2)
c_1	2.92
c_2	3.21
c_3	-2.60
c_4	2.01
c_5	0.0
c_6	-7.89
c_7	66.20
c_8	51.12
c_9	40.12
c_{10}	0.0032

I_1 and I_4 are the invariants of right Cauchy deformation tensor and given by the following equations:

$$I_1 = tr\ \mathrm{C_{ij}} = \mathrm{C_{11}} + \mathrm{C_{22}} + \mathrm{C_{33}} \tag{4.25}$$

$$\begin{aligned} I^2{}_4 &= N_i\ \mathrm{C_{ij}}\ \mathrm{N_j} \\ &= N_1\ \mathrm{C_{11}}\ \mathrm{N_1} + N_1\ \mathrm{C_{12}}\ \mathrm{N_2} + N_1\ \mathrm{C_{13}}\ \mathrm{N_3} + N_2\ \mathrm{C_{21}}\ \mathrm{N_1} + N_2\ \mathrm{C_{22}}\ \mathrm{N_2} \\ &\quad + N_2\ \mathrm{C_{23}}\ \mathrm{N_3} + N_3\ \mathrm{C_{31}}\ \mathrm{N_1} + N_3\ \mathrm{C_{32}}\ \mathrm{N_2} + N_3\ \mathrm{C_{33}}\ \mathrm{N_3} \end{aligned} \tag{4.26}$$

b. Driving the Stress Equations of the LV Model:

Second PK stress for a nonlinear elastic incompressible material based on a strain energy function is given as follows:

$$S_{ij} = -p_{hyd} C_{ij}^{-1} + 2\frac{\partial W}{\partial C_{ij}} \tag{4.27}$$

$$S_{ij\_\mathrm{passive}} = -p_{hyd\_passive} C_{ij}^{-1} + 2\frac{\partial W_{pass}}{\partial C_{ij}}$$

$$S_{ij\_active} = -p_{hyd\_active} C_{ij}^{-1} + 2\frac{\partial W_{active}}{\partial C_{ij}} \tag{4.28}$$

Here, $p_{hyd\_passive}$ and p_{hyd_active} represent the hydrostatic pressure value at passive and active phases.

Lin *et al.* followed the same assumption of Humphreys *et al.* for the muscle fiber direction. Humphreys *et al.* assumed that the fibers were located in the *x* direction. This assumption leads to the normal vector *N* will be equal (1, 0, 0); and from this assumption the following invariants will be equal:

$$I_4^2 = C_{11}$$

so

$$I_4 = \sqrt{C_{11}} \tag{4.29}$$

The components of the second PK stress will be directly written as follows:

$$S_{11\_passive} = -p_{hyd\_passive} C_{11}^{-1} + 2\frac{\partial W_{pass}}{\partial C_{11}} \tag{4.30}$$

$$S_{11\_active} = -p_{hyd\_active} C_{11}^{-1} + 2\frac{\partial W_{active}}{\partial C_{11}}$$

The differentiation of the passive energy function with respect to C_{11} will be given as follows:

$$\frac{\partial W_{pass}}{\partial C_{11}} = c_1 * \exp\left(\begin{array}{l} c_4\left(C_{11}^{(1/2)} - 1\right)^2 + c_2\left(C_{11} + C_{22} + C_{33} - 3\right)^2 + \\ c_3\left(C_{11}^{(1/2)} - 1\right)\left(C_{11} + C_{22} + C_{33} - 3\right) \end{array} \right)$$
$$\left(c_2\left(2C_{11} + 2C_{22} + 2C_{33} - 6\right) + c_3\left(C_{11}^{(1/2)} - 1\right) + \right.$$
$$\left.\left(c_4\left(C11^{(1/2)} - 1\right)\right) / C_{11}^{(1/2)} + \left(c_3\left(C_{11} + C_{22} + C_{33} - 3\right)\right) / \left(2C_{11}^{(1/2)}\right)\right) \tag{4.31}$$

The differentiation of the active energy function with respect to C_{11} will be as follows:

$$\frac{\partial W_{active}}{\partial C_{11}} = c_9 + c_7\left(2C_{11} + 2C_{22} + 2C_{33} - 6\right) + c_{10} / \left(2C_{11}^{(1/2)}\right) +$$
$$c_6\left(C_{11}^{(1/2)} - 1\right) + \left(c8\left(C_{11}^{(1/2)} - 1\right)\right) / C_{11}^{(1/2)} +$$
$$\left(c_6\left(C_{11} + C_{22} + C_{33} - 3\right)\right) / \left(2C_{11}^{(1/2)}\right) \tag{4.32}$$

The first stress component for the passive and active phases will be as follows:

$$S_{11\_passive} = -p_{hyd\_passive} C_{11}^{-1} + c_1 * \exp\left(\begin{array}{l} c_4\left(C_{11}^{(1/2)} - 1\right)^2 + c_2\left(C_{11} + C_{22} + C_{33} - 3\right)^2 + \\ c_3\left(C_{11}^{(1/2)} - 1\right)\left(C_{11} + C_{22} + C_{33} - 3\right) \end{array} \right)$$
$$\left(c_2\left(2C_{11} + 2C_{22} + 2C_{33} - 6\right) + c_3\left(C_{11}^{(1/2)} - 1\right) + \right.$$
$$\left.\left(c_4\left(C_{11}^{(1/2)} - 1\right)\right) / C_{11}^{(1/2)} + \left(c_3\left(C_{11} + C_{22} + C_{33} - 3\right)\right) / \left(2C_{11}^{(1/2)}\right)\right) \tag{4.33}$$

$$S_{11\_active} = -p_{hyd\_active} C_{11}^{-1} + c_9 + c_7\left(2C_{11} + 2C_{22} + 2C_{33} - 6\right) + c_{10} / \left(2C_{11}^{(1/2)}\right) +$$
$$c_6\left(C_{11}^{(1/2)} - 1\right) + \left(c_8\left(C_{11}^{(1/2)} - 1\right)\right) / C_{11}^{(1/2)} +$$
$$\left(c_6\left(C_{11} + C_{22} + C_{33} - 3\right)\right) / \left(2C_{11}^{(1/2)}\right) \tag{4.34}$$

The differentiation of the passive energy function with respect to C_{22} will be as follows:

$$\frac{\partial W_{pass}}{\partial C_{22}} = c_1 \exp\left(\begin{array}{l} c_4\left(C_{11}^{(1/2)} - 1\right)^2 + c_2\left(C_{11} + C_{22} + C_{33} - 3\right)^2 + \\ c_3\left(C_{11}^{(1/2)} - 1\right)\left(C_{11} + C_{22} + C_{33} - 3\right) \end{array} \right)$$
$$\left(c_2\left(2C_{11} + 2C_{22} + 2C_{33} - 6\right) + c_3\left(C_{11}^{(1/2)} - 1\right)\right) \tag{4.35}$$

The differentiation of the active energy function with respect to C_{22} will be as follows:

$$\frac{\partial W_{active}}{\partial C_{22}} = c_9 + c_7\left(2C_{11} + 2C_{22} + 2C_{33} - 6\right) + c6\left(C_{11}^{(1/2)} - 1\right) \tag{4.36}$$

The second stress component for the passive and active phases will be as follows:

$$S_{22\_passive} = -p_{hyd\_passive} C_{22}^{-1} + c_1 \exp\left(\begin{array}{l} c_4\left(C_{11}^{(1/2)} - 1\right)^2 + c_2\left(C_{11} + C_{22} + C_{33} - 3\right)^2 + \\ c_3\left(C_{11}^{(1/2)} - 1\right)\left(C_{11} + C_{22} + C_{33} - 3\right) \end{array} \right) \left(c_2\left(2C_{11} + 2C_{22} + 2C_{33} - 6\right) + c_3\left(C_{11}^{(1/2)} - 1\right)\right) \tag{4.37}$$

$$S_{22\_active} = -p_{hyd\_active} C_{22}^{-1} + c_9 + c_7\left(2C_{11} + 2C_{22} + 2C_{33} - 6\right) + c6\left(C_{11}^{(1/2)} - 1\right) \tag{4.38}$$

The differentiation of the passive energy function with respect to C_{33} will be as follows:

$$\frac{\partial W_{pass}}{\partial C_{33}} = c_1 \exp\left(\begin{array}{l} c_4\left(C_{11}^{(1/2)} - 1\right)^2 + c_2\left(C_{11} + C_{22} + C_{33} - 3\right)^2 \\ + c_3\left(C_{11}^{(1/2)} - 1\right)\left(C_{11} + C_{22} + C_{33} - 3\right) \end{array} \right) \left(c_2\left(2C_{11} + 2C_{22} + 2C_{33} - 6\right) + c3\left(C_{11}^{(1/2)} - 1\right)\right) \tag{4.39}$$

The differentiation of the active energy function with respect to C_{33} will be as follows:

$$\frac{\partial W_{active}}{\partial C_{33}} = c_9 + c_7\left(2C_{11} + 2C_{22} + 2C_{33} - 6\right) + c_6\left(C_{11}^{(1/2)} - 1\right) \tag{4.40}$$

The third stress component for the passive and active phases will be as follows:

$$S_{33\_passive} = -p_{hyd\_passive} C_{33}^{-1} + c_1 \exp\left(\begin{array}{l} c_4\left(C_{11}^{(1/2)} - 1\right)^2 + c_2\left(C_{11} + C_{22} + C_{33} - 3\right)^2 \\ + c_3\left(C_{11}^{(1/2)} - 1\right)\left(C_{11} + C_{22} + C_{33} - 3\right) \end{array} \right) \left(c_2\left(2C_{11} + 2C_{22} + 2C_{33} - 6\right) + c3\left(C_{11}^{(1/2)} - 1\right)\right) \tag{4.41}$$

$$S_{33\_active} = -p_{hyd\_active} C_{33}^{-1} + c_9 + c_7\left(2C_{11} + 2C_{22} + 2C_{33} - 6\right) + c_6\left(C_{11}^{(1/2)} - 1\right) \tag{4.42}$$

At this point, it is important to remember that the (S_{33}) third component of the second PK stress tensor is equal to zero. Thus, we can solve for the hydrostatic pressure for both passive and active phases as follows:

$$p_{hyd\_passive} = C_{33}\left[c_1 \exp\left(\begin{array}{l} c_4\left(C_{11}^{(1/2)} - 1\right)^2 + c_2\left(C_{11} + C_{22} + C_{33} - 3\right)^2 \\ + c_3\left(C_{11}^{(1/2)} - 1\right)\left(C_{11} + C_{22} + C_{33} - 3\right) \\ \qquad \left(c_2\left(2C_{11} + 2C_{22} + 2C_{33} - 6\right) + c3\left(C_{11}^{(1/2)} - 1\right)\right) \end{array}\right)\right] \tag{4.43}$$

$$p_{hyd\_active} = C_{33}\left[c_9 + c_7\left(2C_{11} + 2C_{22} + 2C_{33} - 6\right) + c_6\left(C_{11}^{(1/2)} - 1\right)\right] \tag{4.44}$$

4.6 SOLUTION USING FIELD BOUNDARY ELEMENT METHOD

"The Boundary Element Method (BEM) is a technique used to solve partial differential equations by rewriting the original Partial Differential Equation (PDE) into an integral equation over the boundary of an object where the solution of the Boundary Integral Equation (BIE) is exactly the solution of original PDE" [106-109]. Unlike the Finite Element Method (FEM), only the boundary of the object needs to be discretized, because the BIE is only over the boundary of the object [107, 108]. There are two types of boundary conditions for PDE. If the boundary condition is given as specific displacement vector, then this type is known as Dirichlet problem. The other type which is known as Neumann problem, the boundary condition is given as specific traction vector over [107]. The fundamental solutions for PDE should first be obtained to enable the conversion of the PDE into a boundary integral equation [107, 110, 111].

a. Fundamental Solutions:

"The fundamental solution for the plane stress elasticity problem is the solution for a point load x^p of unit magnitude applied to a point x in an infinite 2D medium of unit thickness. The fundamental solutions are sometimes referred to as Kelvin solutions, Green's functions, or singular solutions. The displacement of a point x in an infinite medium with a unit load applied at x^p is known as the displacement fundamental solution. U_{kj} is the fundamental solution which represents the displacement at point x in the k direction due to a unit load applied at x^p in the j direction in the infinite plane" [106]. U_{kj} is calculated by the following equation[106]:

$$U_{kl}(x^p, x) = C_1\left[C_2 \ln\frac{1}{r}\delta_{lk} + \frac{(x_l^p - x_l)(x_k^p - x_k)}{r^2}\right] \tag{4.45}$$

where

$$C_1 = \frac{1}{8\pi\mu(1-v)}$$

$$C_2 = 3 - 4v$$

$$r = \left[(x_1^p - x_1) + (x_2^p - x_2)\right]^{\frac{1}{2}} \tag{4.46}$$

"There is also a fundamental solution that gives the traction at a point x in an infinite medium due to a unit load at x^p. The traction vector must be defined in reference to a line l that cuts through the material. The traction vector is the force distribution that would have to be applied to the object if it was cut by the line l in order to maintain the same state of stress in the material" [106]. The fundamental traction solution can be written as [106]:

$$T_{lk}(x^p, x) = \frac{C_3}{r}\left[\frac{\partial r}{\partial n}\left(C_4\delta_{lk} + 2\frac{(x_l^p - x_l)(x_k^p - x_k)}{r^2}\right) + C_4\left(\frac{(n_l(x_k^p - x_k)}{r} - \frac{(n_k(x_l^p - x_l)}{r}\right)\right]$$

where

$$\frac{\partial r}{\partial n} = \frac{n_1(x_1^p - x_1)}{r} - \frac{n_2(x_2^p - x_2)}{r} \tag{4.47}$$

$$C_3 = \frac{1}{4\pi(1-\nu)}$$

$$C_4 = 1 - 2\nu$$

4.7 GOVERNING EQUATION

The framework is based on the assumption that the first PK stress tensor (which is given by Equation (4.19) and the second PK stress tensor (which is given by Equation (4.29) can be split into two parts; linear and nonlinear parts as follows:

$$\sigma_{ij} = \sigma^L{}_{ij} + \sigma^n{}_{ij} \tag{4.48}$$

Here, $\sigma^L{}_{ij}$ represents the linear stress. The nonlinear stress is represented by $\sigma^n{}_{ij}$. The nonlinear part will computed by replacing it with $\left(\sigma_{ij} - \sigma^L{}_{ij}\right)$.

As mentioned above, the myocardium tissue is treated as a transversely isotropic material [103, 112]. For the linear elastic model, the stress-strain relationship has the form:

$$\sigma^L = C^{-1}\,\mathrm{e} \tag{4.49}$$

Here, *e* represents the linear strain and the matrix C^{-1} takes the form:

$$C^{-1} = \begin{bmatrix} \frac{1}{E_p} & \frac{-\nu_{fp}}{E_p} & \frac{-\nu_{fp}}{E_f} & 0 & 0 & 0 \\ \frac{-\nu_p}{E_p} & \frac{1}{E_p} & \frac{-\nu_{fp}}{E_f} & 0 & 0 & 0 \\ \frac{-\nu_{fp}E_f}{E_p} & \frac{-\nu_{fp}E_f}{E_p} & \frac{1}{E_f} & 0 & 0 & 0 \\ 0 & 0 & 0 & \frac{2(1+\nu_p)}{E_p} & 0 & 0 \\ 0 & 0 & 0 & 0 & 0 & \frac{1}{G_f} \end{bmatrix} \tag{4.50}$$

where, E_f is the fiber stiffness, E_p is cross-fiber stiffness and ν_{fp}, ν_p are the corresponding Poisson's ratios [113]. G_f is the shear modulus across fibers and is given by the following equation [113]:

$$G_f \approx \frac{E_f}{2(1+\nu_{fp})} \tag{4.51}$$

4.8 THE EQUILIBRIUM EQUATION

The equation of equilibrium in the absence of body force can be obtained by differentiating Equation (4.48) which represents the total stress, the first PK stress tensor [111]:

$$\sigma_{ij,j} = 0 \tag{4.52}$$

As mentioned earlier in Equation (4.48), the total stress consists of the linear and nonlinear parts, so the equilibrium equation becomes as follows [111]:

$$\sigma^L{}_{ij,j} + \sigma^n{}_{ij,j} = 0 \tag{4.53}$$

In our case the boundary conditions are considered at each point on the boundary and the traction is specified and given as follows:

$$\sigma_{ij}\ N_j = t_i = \overline{t}_i \tag{4.54}$$

4.9 DERIVING THE FBEM EQUATION

Deriving the FBEM equation is based on combining the equilibrium Equation (4.52) and the boundary condition Equation (4.54), by utilizing direct BEM [108].

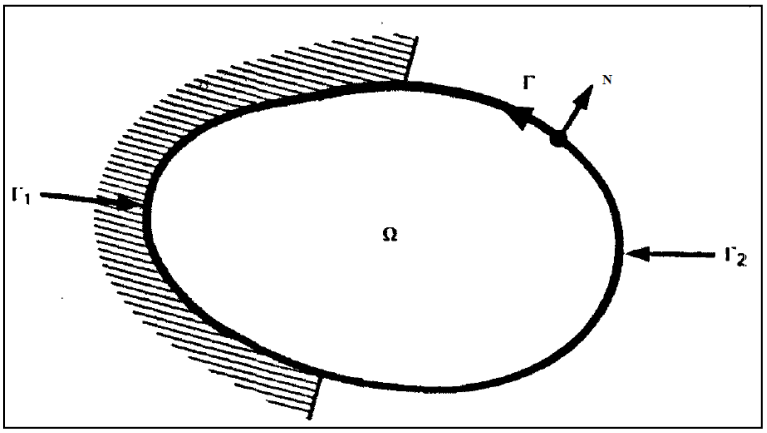

Figure (4.5) - BEM geometrical definition [108]

Equation (4.54) should satisfy the following conditions:

- Essential or displacement conditions:

$$u_k = \overline{u}_k \qquad on\ \ \Gamma_1 \tag{4.55}$$

- Traction conditions:

$$t_k = \overline{t}_k \qquad on\ \ \Gamma_2 \tag{4.56}$$

To minimize Equation (4.52), the equation will be weighted by displacement function u_k^* and orthogonoalize the product as following:

$$\int_{\Omega} (\sigma_{kj,j}) u_k^* d\Omega = 0 \tag{4.57}$$

From Equation (4.48), we will have the following:

$$\int_{\Omega} (\sigma_{kj,j}^L + \sigma_{kj,j}^n) u_k^* d\Omega = 0 \tag{4.58}$$

By applying the integration by parts and by grouping the same terms, the following

equation will result:

$$-\int_{\Omega}\sigma_{kj}^{L}e_{kj}^{*}d\Omega+\int_{\Omega}\sigma_{kj,j}^{n}u_{k}^{*}d\Omega=-\int_{\Gamma}t_{k}u_{k}^{*}d\Gamma \tag{4.59}$$

Applying the integration by parts again resulted in the following equation:

$$\int_{\Omega}\sigma_{kj,j}^{*L}u_{k}d\Omega+\int_{\Omega}\sigma_{kj,j}^{n}u_{k}^{*}d\Omega=-\int_{\Gamma}t_{k}u_{k}^{*}d\Gamma+\int_{\Gamma}t_{k}^{*}u_{k}d\Gamma \tag{4.60}$$

The two terms on the right hand side are integrals on the Γ surface of the body. If we divide the surface into two parts Γ_1 and Γ_2, applying the boundary conditions (4.55) and (4.56), the next equation will be obtained:

$$\int_{\Omega}\sigma_{kj,j}^{*h}u_{k}d\Omega+\int_{\Omega}\sigma_{kj,j}^{n}u_{k}^{*}=-\int_{\Gamma_1}t_{k}u_{k}^{*}d\Gamma-\int_{\Gamma_2}\overline{t}_{k}u_{k}^{*}d\Gamma+\int_{\Gamma_1}\overline{u}_{k}T_{k}^{*}d\Gamma+\int_{\Gamma_2}u_{k}T_{k}^{*}d\Gamma \tag{4.61}$$

The bars in the above equation represent the known values of traction t_k and displacement u_k. Applying the integration by parts again we will get the next equation:

$$\int_{\Omega}(\sigma_{kj,j}^{L}+\sigma_{kj,j}^{n})u_{k}^{*}d\Omega=\int_{\Gamma_2}(t_{k}-\overline{t}_{k})U_{k}^{*}d\Gamma+\int_{\Gamma_2}(u_{k}-\overline{u}_{k})T_{k}^{*}d\Gamma \tag{4.62}$$

The equation is a generalized expression that used to obtain the boundary integral equation. The fundamental solution is obtained when a unit load is applied at a point I in the direction of the unit vector e_i, i.e.

$$\sigma_{kj,j}^{n}=\Delta^{i}e_{l} \tag{4.63}$$

The fundamental solution can be written as follows:

$$U_{k}^{*}=U_{lk}^{*}e_{i}$$
$$T_{k}^{*}=T_{lk}^{*}e_{i} \tag{4.64}$$

The fundamental solutions U_{lk}^{*} and T_{lk}^{*} are k components of displacement and tractions due to a unit load in the l direction. The first integral in (4.62) for a particular direction e_i of the unit load becomes:

$$\int_{\Omega}\sigma_{kj,j}^{*L}u_{k}=\int_{\Omega}\sigma_{ij,j}^{*L}u_{i}d\Omega=-\int_{\Omega}\Delta^{i}u_{l}e_{i}d\Omega=-u_{l}^{i}e_{i} \tag{4.65}$$

Here, u_l^i represents the *l* component of the displacement at the point *i* of application of the load. The equation can now be written to represent the displacement at *i* as follows:

$$u_l^i + \int_{\Gamma_1} T_{lk}^* \bar{u}_k d\Gamma + \int_{\Gamma 2} T_{lk}^* u_k d\Gamma = \int_{\Gamma_1} U_{lk}^* t_k d\Gamma + \int_{\Gamma_2} U_{lk}^* \bar{t}_k d\Gamma + \int_{\Omega} \sigma_{lk,j}^n U_{lk}^* d\Omega \tag{4.66}$$

By applying the boundary conditions and combining the two parts of the boundary together $\Gamma_1 + \Gamma_2$, Equation (4.66) will be written in the following form:

$$u_l^i + \int_{\Gamma} T_{lk}^* u_k d\Gamma = \int_{\Gamma} U_{lk}^* t_k + \int_{\Omega} U_{lk}^* \sigma_{kj,j}^n d\Omega \tag{4.67}$$

Equation (4.67) for the displacement is also written for the boundary nodes as follows:

$$\alpha_{lk}^i u_l^i + \int_{\Gamma} T_{lk}^* u_k d\Gamma = \int_{\Gamma} U_{lk}^* t_k d\Gamma + \int_{\Omega} U_{lk}^* \sigma_{kj,j}^n d\Omega \tag{4.68}$$

The resulting integral equations are:

$$\alpha_{kj}(x^p) u_k(x^p) + \int_{\Gamma} T_{kj}(x^p, x) u_k(x) d\Gamma = \int_{\Gamma} U_{kj}(x^p, x) t_k^L(x^p) d\Gamma +$$

$$\int_{\Omega} U_{kj}(x^p, x) \frac{\partial \sigma_{mk}^n}{\partial x_m}(x) d\Omega \tag{4.69}$$

Here, $\alpha_{kj} = \delta_{kj}$ if x^p lies in the domain Ω, for a point on the boundary, which is smooth at the point $x^p, \alpha_{kj} = \frac{1}{2}\delta_{kj}$. δ_{kj} is the Kronecker delta. u_k is the boundary displacement vector. t_k^L is the linear part of the boundary traction vector, which is given by:

$$t_k^L = \sigma_{jk}^L n_j \tag{4.70}$$

By applying the divergence theorem to Equation (4.69), the nonlinear part can be retrieved. Then, Equation (4.69) will be in the following form:

$$\alpha_{kj}(x^p)u_k(x^p)+\int_\Gamma T_{kj}(x^p,x)u_k(x)d\Gamma=\int_\Gamma U_{kj}(x^p,x)t_k^L(x^p)d\Gamma+$$

$$\int_\Omega \frac{\partial U_{kj}(x^p,x)}{\partial x_m}\sigma_{mk}^n(x)d\Omega \tag{4.71}$$

The derivative of Equation (4.71) will give us the direct displacement gradients inside the domain as follows:

$$\frac{\partial u_j(x^p)}{\partial x^p}=-\int_\Gamma \frac{\partial T_{kj}}{\partial x^p}(x^p,x)u_k(x)d\Gamma(x)+\int_\Gamma \frac{\partial U_{kj}}{\partial x^p}(x^p,x)t_k(x)d\Gamma(x)-$$

$$\int_\Omega \frac{\partial U_{kj}}{\partial X_m \partial x^p}(x^p,x)\sigma_{mk}^n(x)d\Omega(x) \tag{4.72}$$

The domain integral in Equations (4.71) and (4.72) can be transferred to a boundary integral using the divergence theorem. The divergence theorem is given as follows:

$$\int_\Omega \nabla F\,dA=\int_\Gamma F.N\,d\Gamma \tag{4.73}$$

Here, N represents the normal vector. Both equations will be rewritten as:

$$\alpha_{kj}(x^p)u_k(x^p)+\int_\Gamma T_{kj}(x^p,x)u_k(x)d\Gamma=\int_\Gamma U_{kj}(x^p,x)t_k^L(x^p)d\Gamma+$$

$$\int_\Gamma \left\{U_{kj}(x,x^p)\sigma_{mk}^n(x)\right\}.Nd\Omega \tag{4.74}$$

$$\frac{\partial u_j(x^p)}{\partial x^p}=-\int_\Gamma \frac{\partial T_{kj}}{\partial x^p}(x^p,x)u_k(x)d\Gamma(x)+\int_\Gamma \frac{\partial U_{kj}}{\partial x^p}(x^p,x)t_k(x)d\Gamma(x)-$$

$$\int_\Gamma \left\{\frac{\partial U_{kj}}{\partial x^p}(x^p,x)\sigma_{mk}^n(x)\right\}.N\,d\Omega(x) \tag{4.75}$$

The fundamental solution $\frac{\partial T_{kj}}{\partial x^p}$ is given by the following kernel equation [114]:

$$\overset{*}{D}_{ijk} = \frac{1}{4G(1-\nu)r^2}\begin{Bmatrix} 2\left[(1-\nu)r_{,k}\delta_{ij} - r_{,i}\delta_{jk} - r_{,j}\delta_{ik} + 4r_{,i}r_{,j}r_{,k}\right]r_{,k}N_k - \\ (1-2\nu)\left[N_k\delta_{ij} + N_i\delta_{jk} - N_j\delta_{ik} - 2N_i r_{,j}r_{,k} + 2N_j r_{,i}r_{,k}\right] - 2N_k r_{,i}r_{,j} \end{Bmatrix} \tag{4.76}$$

The fundamental solution $\frac{\partial U_{kj}}{\partial x^p}$ is given by the following kernel equation [114]:

$$\overset{*}{K}_{ijm} = \frac{1}{8(1-\nu)Gr}\left\{(3-4\nu)r_{,m}\delta_{ij} - r_{,j}\delta_{im} - r_{,i}\delta_{jm} + 2r_{,i}r_{,j}r_{,m}\right\} \tag{4.77}$$

a. Discritization of FBEM Equations:

It is known that LV has complicated and different shapes during the cardiac cycle. To be more accurate in describing the LV shapes, quadratic shape functions are used with *BE* isoparametric boundary elements. The quadratic shape functions are given with the following formula [108]:

$$N_3(\xi) = 1-\xi^2$$
$$N_n = \frac{1}{2}(1+\xi_n\xi) - \frac{1}{2}N_n \qquad n = 1,2 \tag{4.78}$$

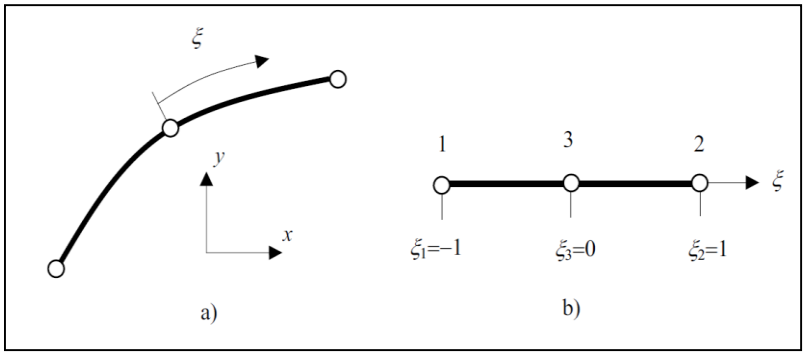

Figure (4.6) Quadratic element a) Global Coordinates b) Local Coordinates [108]

The LV domain is divided into *M* constant domain cells as shown in Figure (4.6). Creating the mesh is the first step in the solution of the BIES. It is essential to evaluate the displacement gradient at each cell in the domain and hence the hydrostatic pressure

p_{hyd} because the constitutive equations are written in terms of displacement gradients and hydrostatic pressure [115].

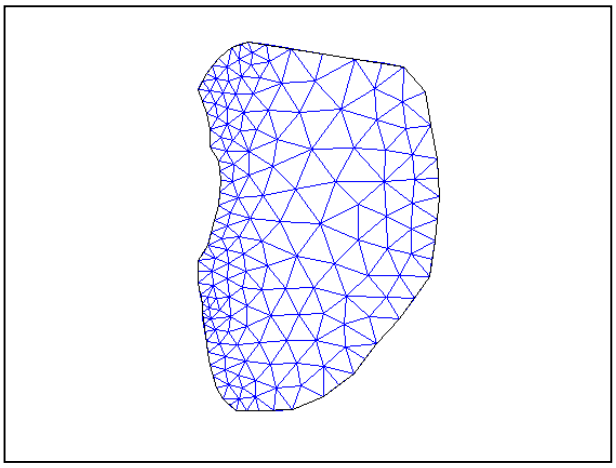

Figure (4.7) Meshing the LV into M cells

The discretization form of Equation (4.74) will be written as follows:

$$\alpha_{kj}(x^p)u(x^p) = \sum_{e=1}^{BE}\int_{\Gamma}\left(\sum_{n=1}^{N} N_n(\xi)t_n^e\right)U(x^p,\xi)d\Gamma(\xi) - \sum_{e=1}^{BE}\int_{\Gamma}\left(\sum_{n=1}^{N} N_n(\xi)u_n^e\right)T(x^p,\xi)d\Gamma(\xi) - \sum_{m=1}^{M}\int_{\Gamma_m}\left(\sum_{n=1}^{N} N_n(\xi)\sigma_{mk}^n(\xi)\right)U(x^p,\xi)d\Gamma(\xi) \quad (4.79)$$

Here, we define the following equations:

$$H = \int_{\Gamma} N_n(\xi)U(x^p,\xi)d(\xi) \quad (4.80)$$

$$G = \int_{\Gamma} N_n(\xi)T(x^p,\xi)d(\xi) \quad (4.81)$$

$$f = \int_{\Gamma_m} N_n(\xi)U(x^p,\xi)N\,d(\xi) \quad (4.82)$$

Equation (4.79) can be represented in matrix form as follows:

$$Hu = Gt + f(\nabla u, p_{hyd}) \quad (4.83)$$

Here, u represents the displacement value of the nodes at the boundary, while t represents the traction value [111]. H, G and f are the coefficient matrices given by Equations (4.80), (4.81) and (4.82). The elements of the matrix f are functions of the displacement gradients and of hydrostatic pressure.

Rearrangement of Equation (4.83) is needed to transfer the boundary unknowns to the left side in matrix y and to combine all the known values in matrix C on the right side after applying the boundary conditions with the corresponding components of H and G. The following equation will result [111]:

$$Ay = C + f(\nabla u, p_{hyd}) \tag{4.84}$$

where A is a coefficient matrix.

The same procedure will be applied to Equation (4.75) to represent it in matrix form. Applying the equation at the centroids of the M domain cells yields the following $4M$ nonlinear equations for the four plane displacement gradients [111], which are illustrated below:

$$\nabla u(x^p) = \sum_{e=1}^{BE} \int_{\Gamma} \left(\sum_{n=1}^{N} N_n(\xi) t_n^e \right) \nabla U(x^p, \xi) d\Gamma(\xi) - \sum_{e=1}^{BE} \int_{\Gamma} \left(\sum_{n=1}^{N} N_n u_n^e \right) \nabla T(x^p, \xi) d\Gamma(\xi) - \sum_{m=1}^{M} \int_{\Gamma_m} \left(\sum_{n=1}^{N} N_n \sigma_{mk}^n(\xi) \right) \nabla U(x^p, \xi) N d\Gamma(\xi) \tag{4.85}$$

Here, we define the following equations:

$$D = \int_{\Gamma} N_n(\xi) \nabla U(x^p, \xi) d\Gamma(\xi) \tag{4.86}$$

$$B = \int_{\Gamma} N_n(\xi) \nabla T(x^p, \xi) d\Gamma(\xi) \tag{4.87}$$

$$g = \int_{\Gamma_m} N_n(\xi) \nabla U(x^p, \xi) N \, d\Gamma(\xi) \tag{4.88}$$

∇T *and* ∇U are given by Equations (4.76) and (4.77) respectively. Equation (4.85) can be written in matrix form as:

$$\nabla u = Bu + Dt + g(\nabla u, p_{hyd}) \tag{4.89}$$

B, *D* and *g* are the coefficient matrices as given in Equations (4.86), (4.87) and (4.88). The elements of the matrix *f* are also functions of the displacement gradients and of hydrostatic pressure.

b. Incompressibility Condition:

Satisfying and maintaining the incompressibility condition over all the *M* domain cells in the LV area is very important in the Yin *et al.* model. The incompressibility condition can be represented mathematically as:

$$\left[\left(\det \mathrm{C}\right)_{\mathrm{m}}\right]=1 \tag{4.90}$$

where, $(\det C)_{\mathrm{m}}$ is the value of the determinant at the centroid of every cell [111] *m* in the LV domain. At every cell in the LV domain, the right Cauchy deformation tensor *C* will be given as follows [111]:

$$C_{ij}=\begin{bmatrix} C_{11} & C_{12} & 0 \\ C_{21} & C_{22} & 0 \\ 0 & 0 & C_{33} \end{bmatrix} \tag{4.91}$$

From this, by using Equation (4.90), C_{33} will be equal to the following value at each node m:

$$C_{33}=\frac{1}{C_{11}C_{22}-C_{12}C_{21}} \tag{4.92}$$

To the incompressibility condition, C_{33} will be used to find the hydrostatic pressure $p_{hyd,}$ which is given earlier by Equation (4.43) for the passive phase and by Equation (4.44) for the active phase in every cell in the whole domain of the LV during the cardiac cycle.

4.10 Evaluation of Regular and Singular Boundary Integrals:

The FBEM implementation is highly dependent on the evaluation of boundary integrals in Equations (4.79) and (4.85). The difficulties are in the singularities that exist in evaluation of matrices *f*, *H* and *G*. For the fundamental solution, x^p is known as the source point and *x* is known as the field point. If the fundamental solution is bounded

everywhere with x, then the integral will be regular in this case. If the fundamental solution has infinity value at some points of x then it is singular. The evaluation of the regular integration will be given first, and then the evaluation of a singular integral will be explained next as explained in [116].

a. Evaluation of Regular Boundary Integration:

As mentioned earlier, after discretization of the boundary into *Be* elements and referring to the fundamental solution as $f(x^p, x)$; the integration will become as follows [116]:

$$I = \sum_{e=1}^{Be} \int_{-1}^{1} f(x^p, x) d\Gamma(x) \tag{4.93}$$

$$I = \sum_{e=1}^{Be} \int_{-1}^{1} f(x^p, x) |Je| d\xi \tag{4.94}$$

Here, $|J|$ is the transformation Jacobian from global to intrinsic coordinates. The Jacobian is given by the following formula:

$$|J| = \sqrt{\left((\partial x/\partial \xi)^2 + (\partial y/\partial \xi)^2\right)} \tag{4.95}$$

To evaluate the regular integrals numerically, usually the Gaussian quadrature method is utilized by employing the following formula:

$$\int_{-1}^{1} f(x^p, x) |J| d\xi = \sum_{n=1}^{N_g} f(x^p, x(\xi_n)) |J| \omega_n \tag{4.96}$$

Here, N_g represents the number of Gaussian points, ξ_n is the Gaussian coordinates and ω_n is the associated weights.

b. Evaluation of Singular Boundary Integration:

The singularity appears on the fundamental solution equation when the source point x^p falls at the nodes of the element on the boundary of the integration. At that moment, the distance r between the source and field point given by Equation (4.43) is equal or approximately equal to zero. Under this condition, the singularity appears in Equation (4.47) (with $1/r$) and Equation (4.45)(with $\ln(1/r)$. The equations will be represented as follows [116]:

$$I_T = \int_\Gamma T(x^p, x)d\Gamma(x) = \int_\Gamma \frac{\bar{T}(x^p, x)}{r^\beta(x^p, x)} d\Gamma(x) \tag{4.97}$$

$$I_U = \int_\Gamma U(x^p, x)d\Gamma(x) = \int_\Gamma \frac{\bar{U}(x^p, x)\log\left[r\left(x^p, x\right)\right]}{r^\beta(x^p, x)} d\Gamma(x) \tag{4.98}$$

Here, $\bar{T}(x^p, x)$ *and* $\bar{U}(x^p, x)$ are bounded everywhere.

To overcome this difficulty, a solution given by [116] will be followed which is based on expressing the nonsingular parts of integration kernels as polynomials on the distance *r*. First, the differentiation element $d\Gamma$ will be transferred to *dr* as follows:

$$dr = \left(r_{,x}x_{,\xi} + r_{,y}y_{,\xi}\right)d\xi \tag{4.99}$$

The $r_{,x}$ and $r_{,y}$ given by the following equations:

$$r_{,x} = \frac{\partial r}{\partial x} = \frac{x - x^p}{r} \quad , \quad r_{,y} = \frac{\partial r}{\partial y} = \frac{x - y^p}{r} \tag{4.100}$$

As mentioned above, $d\Gamma = |J|d\xi$, then $\mathrm{d}\Gamma$ will be come as follows:

$$d\Gamma = \frac{dr}{(\hat{r}.\hat{\eta})} \tag{4.101}$$

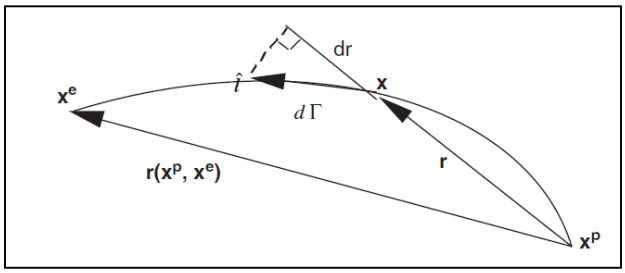

Figure (4.8) Variables over singular element [116]

The unit vector *r* is given by Equation (4.43) and η is the unit vector along the tangential vector direction to $d\Gamma$ as shown in Figure (4.8) and given by the following formula:

$$\hat{\eta}_1 = \frac{\partial x/\partial\xi}{|J|} \quad , \quad \hat{\eta}_2 = \frac{\partial y/\partial\xi}{|J|} \tag{4.102}$$

The differentiation $d\Gamma$ will be substituted by Equation (4.101) in Equations (4.97) and (4.98) to have the following two equations [116]:

$$I_T = \int_0^{r(x^p,x^e)} \frac{\bar{T}(x^p,x)}{\hat{r}.\hat{\eta} r(x^p,x)} dr(x^p,x) \tag{4.103}$$

$$I_U = \int_0^{r(x^p,x^e)} \frac{\bar{U}(x^p,x)\log\left[r(x^p,x)\right]}{\hat{r}.\hat{\eta} r(x^p,x)} dr(x^p,x) \tag{4.104}$$

As mentioned earlier, the singular integrals are evaluated by expressing the nonsingular parts as polynomials of distance r as follows:

$$\frac{\bar{T}(x^p,x)}{\hat{r}.\hat{\eta}} = \sum_{n=0}^{N} C_i^n r^n(x^p,x) \tag{4.105}$$

Here, N is the order of the polynomials and C_i^n represents the coefficients that are computed by collocating the coordinate x at $N+1$ points from the source point x^p to the end point x^e. At the first point where n=0, the term $(\hat{r}.\hat{\eta}=1)$, the first coefficient will be equal:

$$C_i^0 = f(x^p,x^p) \tag{4.106}$$

The rest of the coefficients will be computed by using the following formula:

$$\begin{bmatrix} 1 & r^1(x^p,x^1) & \cdots & x^p,x^1) \\ 1 & r^1(x^p,x^2) & \cdots & x^p,x^2) \\ \vdots & \vdots & \vdots & \vdots \\ 1 & r^1(x^p,x^N) & \cdots & x^p,x^N) \end{bmatrix} \begin{bmatrix} C_i^1 \\ C_i^2 \end{bmatrix} = \begin{bmatrix} f(x^p,x^1)/r.\eta - C_i^0/r(x^p,x^1) \\ f(x^p,x^2)/r.\eta - C_i^0/r(x^p,x^2) \\ \vdots \\ f(x^p,x^N)/r.\eta - C_i^0/r(x^p,x^N) \end{bmatrix} \tag{4.107}$$

By substituting equation (4.107) into equation (4.103) and taking the *lim*, then the integration formula will be resulted as:

$$I_T = \sum_{n=0}^{N} C_i^n F^n$$

where

$$F^n = \begin{cases} \dfrac{r^{n-\beta+1}(x^p, x^e)}{n-\beta+1} & for \quad n-\beta+1 \neq 0 \\ \log\left[r(x^p, x^e) \right] & for \quad n-\beta+1 = 0 \end{cases} \tag{4.108}$$

By using the same procedure [116], Equation (4.98) will be integrated using the following formula:

$$I_U = \sum_{n=0}^{N} C_i^n H^n$$

where

$$H^n = \begin{cases} \dfrac{-\left\{ a \log\left[r(x^p, x^e) \right] + 1 \right\}}{a^2 r^a (x^p, x^e)} & for \quad a = \beta - n - 1 \neq 0 \\ \dfrac{1}{2}\left\{ \log\left[r(x^p, x^e) \right] \right\}^2 & for \quad a = \beta - n - 1 = 0 \end{cases} \tag{4.109}$$

4.11 INCREMENTAL ITERATIVE PROCEDURE

The deformations of the LV can be obtained by solving the equations given by (4.84) and (4.85). The incremental-iterative procedure is used to obtain the LV deformations at each boundary node [111]. The incremental-iterative procedure will be processed as ordered in the following steps:

1. The displacement gradients are initialized by a small value.
2. By using the linear elasticity assumption, we set the nonlinear part to zero. This means the matrices *f* and *g* will equal to zero. This enables us to calculate the values for boundary unknowns, y^1 and the plane displacement gradients ∇u^1.
3. Calculating the initial hydrostatic pressures p_{hyd}^{1} by utilizing Equation (4.43) for the passive phase and Equation (4.44) for the active phase.
4. The matrices *f* and *g* that contain the nonlinear part and hydrostatic pressure can be obtained by employing the results of the ∇u^1 and p_{hyd}^{1}.

5. Updating the boundary unknown y^1 to a new value y^2. The boundary unknowns can be updated by utilizing the values of matrix f in Equation (4.82).
6. Updating the displacement gradients ∇u^1 to ∇u^2. In the same way, the displacement gradients can be updated by using the values of matrix g in equation (4.82).
7. Updating the hydrostatic pressure p_{hyd}^{1} to p_{hyd}^{2} by satisfying the nonlinear incompressibility constraint given by the Equation (4.90) in all LV domain cells using the updated values of the boundary unknowns and the displacement gradients in equations (4.84) and (4.89). The resulting nonlinear algebraic equations have the following form:

$$f_m = (u^2, t^2, \nabla u^2, p_{hyd}^2) = 0 \qquad m = 1, M \qquad (4.110)$$

8. The steps 4 to 7 will be iterated until the solution converges to a specified tolerance.
9. The same iteration procedure will be repeated for all the boundary traction increments and will be added in sequence after the convergence of the previous one.

4.12 RESULTS FROM FBEM

The solution of FBEM was built by MATLAB to solve the BM model equations and the results were not acceptable. FBEM cannot provide the solution to find the deformations of the heart at each frame of echocardiography images. The displacement values at the boundaries of the LV were very high, which cannot be represented in the output screen. The heart is highly nonlinear, time varying and load dependent. Cardiac cycles last for 0.8 seconds and the ultrasound images for one cardiac cycle have 40 images (frames), so each frame takes .8/40=0.02 sec. During the contraction, the cardiac muscles move under pressure, which varies between 80-120 mmHg. To mimic the LV motion at each frame, the simulation should contain these factors. In the FBEM, time and load (pressure) cannot be included in the solution. According to this, the equilibrium equation will not be satisfied which leads to divergence of the solution.

An alternative approach is used to solve the BM model equations by utilizing FEM instead of FBEM.

4.13 FEM APPROACH

The Finite Element Method is chosen to solve the BM constitutive equations due to its ability to include all the required factors of the solution. Figure (4.9) illustrates the solution steps:

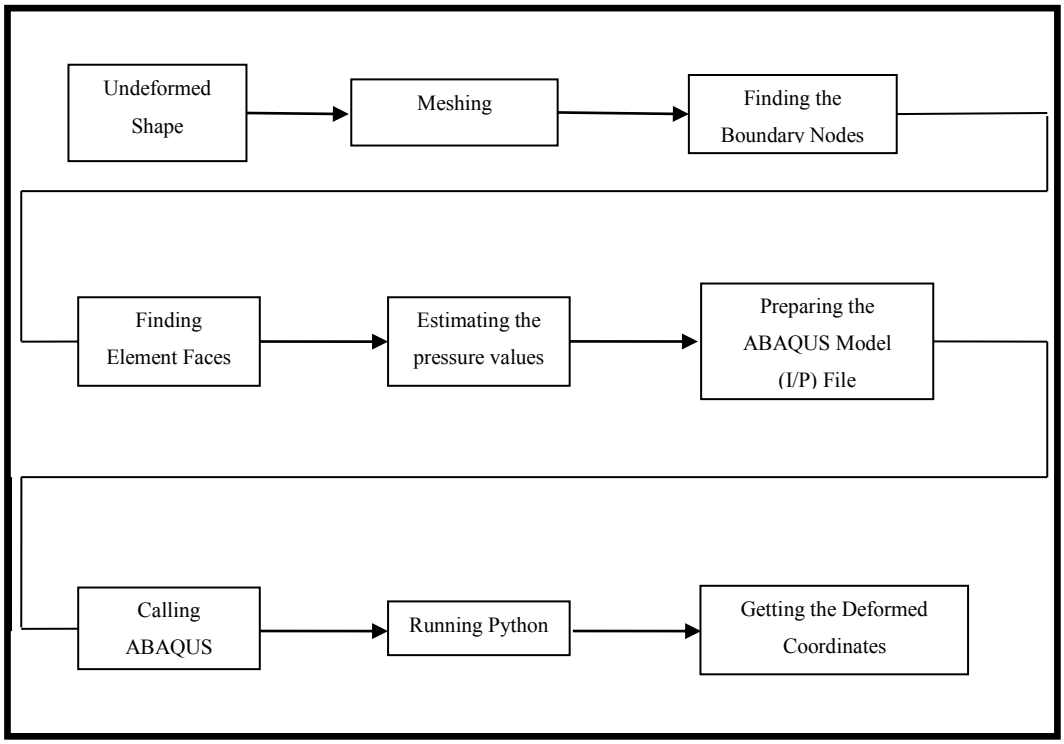

Figure (4.9) - FEM solution block diagram

The undeformed shape is obtained by using the previous frame in the cardiac cycle. The meshing of the LV domain is the same as previously explained in the FBEM solution.

a. Finding the Boundary Nodes

After meshing the LV domain, the nodes at the boundary of the LV should be found and identified. This step is necessary to find the nodes where the boundary conditions should be applied.

b. Finding the Element Faces

After finding the nodes that form the boundaries of the LV, the elements that relate to these nodes will be identified. After knowing the boundary elements, the faces of each boundary element must be recognized. Each triangle element has three faces. These faces are ordered in anticlockwise direction as shown in Figure (4.10). Next, the face of the triangle element at the boundary should be found and identified as Face1, Face2, or Face3. After identifying all the faces at the boundary of the LV, the same faces will be grouped together in one group. After that, all the groups will be combined together to form one surface. This surface is where the pressure should be applied during the systole and diastole stages of the cardiac cycle.

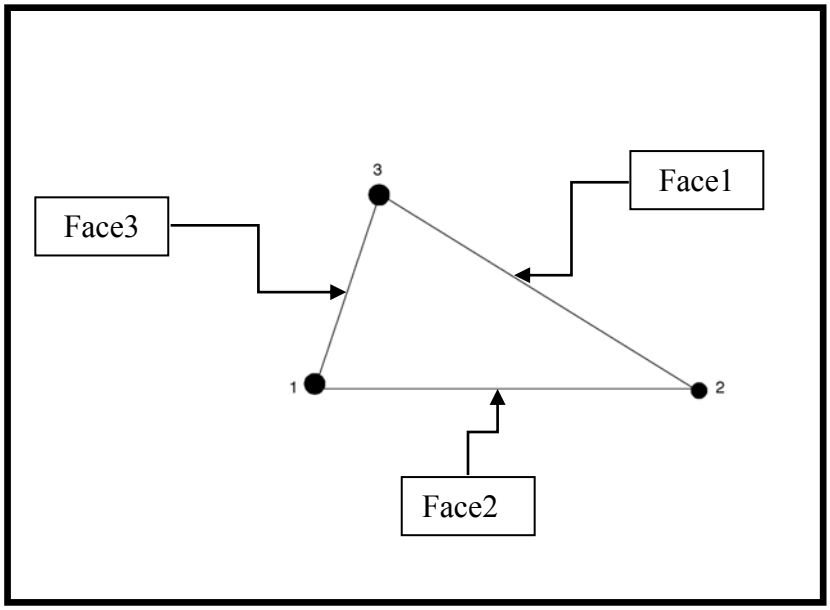

Figure (4.10)-Identifying triangle element's faces

c. Boundary Conditions and Pressure Load Simulation

In the anatomy of a heart, LV is bridled by the atria, RV (right ventricle) and the aorta. The quantitative information of the boundary conditions between these parts of the heart is unknown. To prevent rigid body motion of the left ventricle during the calculation of deformation, the basal plane (as shown in Figure (4.11)) motion should be suppressed.

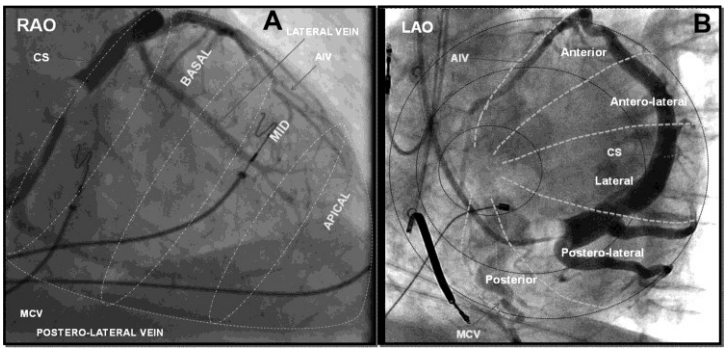

Figure (4.11) Basal, mid and apical areas of the heart [117]

The load applied to the endocardial surface is the blood pressure. The blood pressure in a human heart depends on time and location. The fluid dynamics of the blood pressure in the left ventricle should be taken into account to estimate the spatial distribution of the blood pressure as a function in time. During LV contraction, the pressure gradients are very small compared to the absolute pressure. From this, we can assume a uniform parabolic distribution of the pressure along the endocardial surface of the LV.

From tracking of the cardiac cycle, the duration of the systole phase lasts for 16 frames starting at the QRS ECG signal. The pressure starts rising up to 80 mmHg and reaches the peak of 120 mmHg and down to 80 mmHg at the end of the systole stage.

In the literature [103] , the blood pressure of the left ventricle variation with time is simulated as follows:

$$P = -944.38t^2 + 245.54t \qquad 0 \le t \le 0.2 \tag{4.111}$$

To find the pressure at each certain frame in the contraction phase, the time should be related to the frame number. The following equation is developed to establish the relation and find the specific value of the time t to the specific frame number k:

$$t = 0.055 + k \ * 0.0090625 \tag{4.112}$$

The total duration of time is divided over the 16 frames which covers the systole stage. By calculating t according to the frame number, the pressure value will be calculated from the previous equation. The minimum pressure will be 10.666 Kpa which

corresponds to 80mmHg, while the maximum pressure value is 15.96 kpa, which corresponds to 120 mmHg. These values are the normal systolic blood pressure for an intact heart.

In the diastole stage, the pressure is approximately fixed and according to the literature, a value of 5 K pa is used as indicated in the pressure curve in the cardiac cycle diagram.

d. ABAQUS FEM

ABAQUS is a powerful software package of Finite Element Analysis (FEA) that has proven high solution ability and quality in the performance of complicated engineering challenges and problems [118]

ABAQUS runs commands called keywords which are prepared in an input file. The keywords contain all the information that defines the geometry (mesh and nodes), the properties of the material, the boundary conditions and that control output from the program [118].

e. ABAQUS Model

ABAQUS analysis can be divided into three stages; preprocessing, running ABAQUS/Standard and postprocessing. These three stages are processed in sequence as follows [119] :

1- Preprocessing

In the preprocessing stage, the ABAQUS model of the physical problem is defined by creating an input file. The input file consists of two parts; model and history. The model part contains the geometry discretization by defining the nodes and elements, material data, the loads and boundary conditions. The history part defines the analysis type (linear/nonlinear, static/dynamic or other analysis) and what we will do to the created model. The work done in this part is in steps. The input file in ABAQUS has the **.inp* extension [120] .

2- Running ABAQUS /Standard

The ABAQUS model is passed to the solver (ABAQUS /Standard), which runs in background mode and starts solving the problem numerically.

3- Postprocessing

Postprocessing is the stage where we get the results and start using or evaluating these results.

For each frame of the echocardiographic image sequence, the ABAQUS model (input file) is prepared by a MATLAB script that identifies the entire model and history data, which are saved in the input file and run by ABAQUS to estimate the deformations of the LV at that moment in the cardiac cycle.

f. User Defined Subroutines

Besides the input file, two user subroutines are prepared and used in the framework. To identify the BM to ABAQUS, both the passive and active strain energy functions should be declared in a specific user subroutine in ABAQUS called UANISOHYPER_STRAIN.F. The letter U stands for User, ANISO stands for anisotropic material, HYPER stands for hyperelastic material and STRAIN stands for strain energy function. In ABAQUS, the user can use this subroutine to define the strain energy function of the anisotropic hyperelastic material and the components of this strain energy function must be defined as a function in the Green strain tensor [121].

This subroutine should be written in FORTRAN as requested by ABAQUS. In this subroutine, the first and second derivative of the strain energy functions (both for the passive and active phases) must be provided and declared as part of the solution [121].

The passive and strain energy functions will be differentiated with respect to E_{11}, E_{22} and E_{33}. The other components, which are E_{12}, E_{13}, E_{21}, E_{23}, E_{31}, and E_{32} are equal zero due to absence of their components in the strain energy functions. The first derivatives of the passive strain energy function will be as follows [118]:

$$\frac{dW_{pass}}{dE_{11}} = c_1 * exp(c_2 * (2*E_{11} + 2*E_{22} + 2*E_{33})^2 + c_4 * ((2*E_{11}+1)^{(1/2)} - 1)^2 + c_3 * ((2*E_{11}+1)^{(1/2)} - 1) * (2*E_{11} + 2*E_{22} + 2*E_{33})) * (c_2 * (8*E_{11} + 8*E_{22} + 8*E_{33}) + 2*c_3 * ((2*E_{11}+1)^{(1/2)} - 1) + (c_3 * (2*E_{11} + 2*E_{22} + 2*E_{33})) / (2*E_{11}+1)^{(1/2)} + (2*c4 * ((2*E_{11}+1)^{(1/2)} - 1)) / (2*E_{11}+1)^{(1/2)}) \quad (4.113)$$

$$\frac{dW_{pass}}{dE_{22}} = c_1 * exp(c_2 * (2*E_{11} + 2*E_{22} + 2*E_{33})^2 + c_4 * ((2*E_{11}+1)^{(1/2)} - 1)^2 + c_3 * ((2*E_{11}+1)^{(1/2)} - 1) * (2*E_{11} + 2*E_{22} + 2*E_{33})) * (c_2 * (8*E_{11} + 8*E_{22} + 8*E_{33}) + 2*c_3 * ((2*E_{11}+1)^{(1/2)} - 1)) \quad (4.114)$$

$$\frac{dW_{pass}}{dE_{33}} = c_1 * exp(c_2 * (2*E_{11} + 2*E_{22} + 2*E_{33})^2 + c_4 * ((2*E_{11}+1)^{(1/2)} - 1)^2 + c_3 * ((2*E_{11}+1)^{(1/2)} - 1) * (2*E_{11} + 2*E_{22} + 2*E_{33})) * (c_2 * (8*E_{11} + 8*E_{22} + 8*E_{33}) + 2*c_3 * ((2*E_{11}+1)^{(1/2)} - 1)) \quad (4.115)$$

The second derivatives of the passive strain energy function will be given as following:

$$\frac{d^2W_{pass}}{dE_{11}^2} = c_1 * exp(c_2 * (2*E_{11} + 2*E_{22} + 2*E_{33})^2 +$$
$$c_4 * ((2*E_{11}+1)^{(1/2)} - 1)^2 +$$
$$c_3 * ((2*E_{11}+1)^{(1/2)} - 1) * (2*E_{11} + 2*E_{22} + 2*E_{33})) *$$
$$(c_2 * (8*E_{11} + 8*E_{22} + 8*E_{33}) +$$
$$2*c_3 * ((2*E_{11}+1)^{(1/2)} - 1) +$$
$$(c_3 * (2*E_{11} + 2*E_{22} + 2*E_{33})) / (2*E_{11}+1)^{(1/2)} +$$
$$(2*c_4 * ((2*E_{11}+1)^{(1/2)} - 1)) / (2*E_{11}+1)^{(1/2)})^2 +$$
$$c_1 * exp(c_2 * (2*E_{11} + 2*E_{22} + 2*E_{33})^2 +$$
$$c_4 * ((2*E_{11}+1)^{(1/2)} - 1)^2 +$$
$$c_3 * ((2*E_{11}+1)^{(1/2)} - 1) * (2*E_{11} + 2*E_{22} + 2*E_{33})) *$$
$$(8*c_2 + (4*c_3) / (2*E_{11}+1)^{(1/2)} +$$
$$(2*c_4) / (2*E_{11}+1) -$$
$$(c_3 * (2*E_{11} + 2*E_{22} + 2*E_{33})) / (2*E_{11}+1)^{(3/2)} -$$
$$(2*c_4 * ((2*E_{11}+1)^{(1/2)} - 1)) / (2*E_{11}+1)^{(3/2)}) \quad (4.116)$$

$$\frac{d^2W_{pass}}{dE_{11}dE_{22}} = c_1 * exp(c_2 * (2*E_{11} + 2*E_{22} + 2*E_{33})^2 +$$
$$c_4 * ((2*E_{11}+1)^{(1/2)} - 1)^2 +$$
$$c_3 * ((2*E_{11}+1)^{(1/2)} - 1) * (2*E_{11} + 2*E_{22} + 2*E_{33})) *$$
$$(8*c_2 + (2*c_3) / (2*E_{11}+1)^{(1/2)}) +$$
$$c_1 * exp(c_2 * (2*E_{11} + 2*E_{22} + 2*E_{33})^2 +$$
$$c_4 * ((2*E_{11}+1)^{(1/2)} - 1)^2 +$$
$$c_3 * ((2*E_{11}+1)^{(1/2)} - 1) * (2*E_{11} + 2*E_{22} + 2*E_{33})) *$$
$$(c_2 * (8*E_{11} + 8*E_{22} + 8*E_{33}) +$$
$$2*c_3 * ((2*E_{11}+1)^{(1/2)} - 1)) *$$
$$(c2 * (8*E_{11} + 8*E_{22} + 8*E_{33}) +$$
$$2*c_3 * ((2*E_{11}+1)^{(1/2)} - 1) +$$
$$(c_3 * (2*E_{11} + 2*E_{22} + 2*E_{33})) / (2*E_{11}+1)^{(1/2)} +$$
$$(2*c_4 * ((2*E_{11}+1)^{(1/2)} - 1)) / (2*E_{11}+1)^{(1/2)}) \quad (4.117)$$

$$\frac{d^2Wpass}{dE_{11}dE_{33}} = c_1 * exp(c_2 * (2*E_{11} + 2*E_{22} + 2*E_{33})^2 +$$
$$c_4 * ((2*E_{11}+1)^{(1/2)} - 1)^2 +$$
$$c_3 * ((2*E_{11}+1)^{(1/2)} - 1) * (2*E_{11} + 2*E_{22} + 2*E_{33})) *$$
$$(8*c_2 + (2*c_3)/(2*E_{11}+1)^{(1/2)}) +$$
$$c_1 * exp(c_2 * (2*E_{11} + 2*E_{22} + 2*E_{33})^2 +$$
$$c_4 * ((2*E_{11}+1)^{(1/2)} - 1)^2 +$$
$$c_3 * ((2*E_{11}+1)^{(1/2)} - 1) * (2*E_{11} + 2*E_{22} + 2*E_{33})) *$$
$$(c_2 * (8*E_{11} + 8*E_{22} + 8*E_{33}) +$$
$$2*c_3 * ((2*E_{11}+1)^{(1/2)} - 1)) *$$
$$(c_2 * (8*E_{11} + 8*E_{22} + 8*E_{33}) +$$
$$2*c_3 * ((2*E_{11}+1)^{(1/2)} - 1) +$$
$$(c_3 * (2*E_{11} + 2*E_{22} + 2*E_{33})) / (2*E_{11}+1)^{(1/2)} +$$
$$(2*c_4 * ((2*E_{11}+1)^{(1/2)} - 1)) / (2*E_{11}+1)^{(1/2)}) \quad (4.118)$$

$$\frac{d^2w_{pass}}{dE_{22}^2} = c_1 * exp(c_2 * (2*E_{11} + 2*E_{22} + 2*E_{33})^2 +$$
$$c_4 * ((2*E_{11}+1)^{(1/2)} - 1)^2 +$$
$$c_3 * ((2*E_{11}+1)^{(1/2)} - 1) * (2*E_{11} + 2*E_{22} + 2*E_{33})) *$$
$$(c_2 * (8*E_{11} + 8*E_{22} + 8*E_{33}) +$$
$$2*c_3 * ((2*E_{11}+1)^{(1/2)} - 1))^2 +$$
$$8*c_1 * c2 * exp(c_2 * (2*E_{11} + 2*E_{22} + 2*E_{33})^2 +$$
$$c_4 * ((2*E_{11}+1)^{(1/2)} - 1)^2 +$$
$$c_3 * ((2*E_{11}+1)^{(1/2)} - 1) *$$
$$(2*E_{11} + 2*E_{22} + 2*E3_3)) \quad (4.119)$$

$$\frac{d^2W_{pass}}{dE_{22}dE_{33}} = c_1 * exp(c_2 * (2*E_{11} + 2*E_{22} + 2*E_{33})^2 + c_4 * ((2*E_{11}+1)^{(1/2)} - 1)^2 + c_3 * ((2*E_{11}+1)^{(1/2)} - 1) * (2*E_{11} + 2*E_{22} + 2*E_{33})) * (c_2 * (8*E_{11} + 8*E_{22} + 8*E_{33}) + 2*c_3 * ((2*E_{11}+1)^{(1/2)} - 1))^2 + 8*c_1*c_2 * exp(c_2 * (2*E_{11} + 2*E_{22} + 2*E_{33})^2 + c_4 * ((2*E_{11}+1)^{(1/2)} - 1)^2 + c_3 * ((2*E_{11}+1)^{(1/2)} - 1) * (2*E_{11} + 2*E_{22} + 2*E_{33}))$$

(4.120)

The first derivatives of the active strain energy function will be as follows:

$$\frac{dW_{active}}{dE_{11}} = 2*c_9 + c_7 * (8*E_{11} + 8*E_{22} + 8*E_{33}) + c_{10} / (2*E_{11}+1)^{(1/2)} + 2*c_6 * ((2*E_{11}+1)^{(1/2)} - 1) + (c_6 * (2*E_{11} + 2*E_{22} + 2*E_{33})) / (2*E_{11}+1)^{(1/2)} + (2*c_8 * ((2*E_{11}+1)^{(1/2)} - 1)) / (2*E_{11}+1)^{(1/2)}$$

(4.121)

$$\frac{dW_{active}}{dE_{22}} = 2*c_9 + c_7 * (8*E_{11} + 8*E_{22} + 8*E_{33}) + 2*c_6 * ((2*E_{11}+1)^{(1/2)} - 1)$$

(4.122)

$$\frac{dW_{active}}{dE_{33}} = 2*c_9 + c_7 * (8*E_{11} + 8*E_{22} + 8*E_{33}) + 2*c_6 * ((2*E_{11}+1)^{(1/2)} - 1)$$

(4.123)

The second derivatives of the active strain energy function will be given as follows:

$$\frac{d^2W_{active}}{d^2E_{11}} = 8*c_7 - c_{10}/(2*E_{11}+1)^{(3/2)} + (4*c_6)/(2*E_{11}+1)^{(1/2)} + (2*c_8)/(2*E11+1) - (c_6*(2*E_{11}+2*E_{22}+2*E_{33}))/(2*E_{11}+1)^{(3/2)} - (2*c_8*((2*E_{11}+1)^{(1/2)}-1))/(2*E_{11}+1)^{(3/2)} \quad (4.124)$$

$$\frac{d^2W_{active}}{dE_{22}dE_{11}} = 8*c_7 + (2*c_6)/(2*E_{11}+1)^{(1/2)} \quad (4.125)$$

$$\frac{d^2W_{active}}{dE_{11}dE_{33}} = 8*c_7 + (2*c_6)/(2*E_{11}+1)^{(1/2)} \quad (4.126)$$

$$\frac{d^2W_{active}}{d^2E_{22}} = 8*c_7 \quad (4.127)$$

$$\frac{d^2W_{active}}{dE_{22}dE_{33}} = 8*c_7 \quad (4.128)$$

$$\frac{d^2W_{active}}{dE_{33}^2} = 8*c_7 \quad (4.129)$$

The subroutines will be compiled at the same time with the input file (ABAQUS model).

ABAQUS will call these subroutines at each material calculation step of elements where the material definition contains user defined anisotropic hyperelastic material behavior.

g. ABAQUS and MATLAB Linking

ABAQUS will be called from MATLAB script and it will run in background mode.

After the completion of the ABAQUS model, a Python program will also be called from MATLAB script to read the results from the ODB file (Output Data Base).

The Python program will read the deformations (DISPLACEMNTS) at each boundary node and add these to the original coordinates to find the objective; the

deformed contour. After completion of these calculations, the MATLAB will continue running to complete the required jobs [120].

4.14 SUMMARY

In this chapter, a brief explanation about the continuum mechanics is introduced along with the most important parameters used. The material behavior of the LV is presented. The passive and active strain energy functions of the LV are described and the derivations of stress tensors are given. Brief information about the BEM is given. The derivation of the FBEM equation is provided. Also, the numerical solution of the regular and singular integrations of BIE is provided. The incremental-iterative solution of the nonlinear FBEM is given to find the LV deformations. Due to the not acceptable results from the FBEM, the alternative approach of using FEM is introduced for solving the BM constitutive equations. A brief explanation regarding ABAQUS FEA and its model is introduced. The desecration for the solution and how the ABAQUS linked with MATLAB is also provided.

CHAPTER 5 DEFORMABLE MODEL IN COMBINATION WITH BIOMECHANICAL MODEL

5.1 INTRODUCTION

In this chapter, the ACM (Active Contour Model) or Snake is introduced and explained in detail. The nonlinear Extended Kalman Filter (EKF) is also introduced along with its equations. The Kalman filter based framework, which is used to fuse the ACM with the BM model, is explained. The second order dynamic motion model is explained and used to provide robustness for the tracking system. The entire steps of the framework are explained in detail with the interpretation of the mechanism. An averaging approach alternative to EKF is introduced and used.

5.2 ACM (ACTIVE CONTOUR MODEL) SNAKE

As mentioned in Chapter 3, ACM or Snake is used in the area of image processing to detect the contour of an object. In other words, Snake can be defined as a set of control points, which target to enclose the contour of an object to be extracted. Snake is modeled as parametric curve that evolves into a position where its energy functional is minimized. The position of the snake is given by the parametric curve $C(s) = [x(s), y(s)]$ with $s = [0, 1]$. In the closed curve, the first point $C(0)$ is equal to the last point $C(N)$.

c. Snake Energy Function

Snake is a parametric curve which evolves to a position where its energy has the minimum value. A parametric deformable model is used instead of nonparametric deformable models (Level set methods) due to the way that the parametric models represent their curves with a set of control points in the same manner that we use to represent the contour curve in the BM model. The BM model represents the curve as a set of nodes. This similarity enables us to use point to point mapping to fuse both contours of Snake and BM models. Unlike the parametric deformable models, the level set method

represents the curve implicitly where the level set function is equal to zero, which does not match the way the BM model is using to represent the LV contour.

Kass *et al.* [33] formulated the Snake as an energy minimization process; the final contour is where the function has its lowest minimum value. The function consists of the contour internal energy and the image energy and is given as follows:

$$E_{Snake} = \int_0^1 (E_{internal}(C(s)) + E_{image}(C(s)))ds \tag{5.1}$$

The internal energy function represents the properties of the Snake such as its ability to stretch or bend where the image energy is the edge magnitude, which attracts the Snake to the boundaries of the object. The Snake will evolve until it reaches the lowest value that minimizes Equation (5.1) where the points of Snake *C(s)* will set the function as follows:

$$\frac{dE_{Snake}}{dC} = 0 \tag{5.2}$$

The total energy functional of the Snake is the combination of functions of the internal and the image energies. The internal energy function is given as follows:

$$E_{INT} = \int_0^1 (\alpha \|C'(s)\|^2 + \beta \|C''(s)\|^2)ds \tag{5.3}$$

The first term in the internal energy represents the elasticity due to stretching where the higher values of this derivative pushes the Snake to a new region. The second term represents the curvature due to the bending. The participation of the two terms in the internal energy is controlled by the parameters α and β respectively.

d. Image Energy Function

The image energy attracts the Snake to the boundaries of the object in the image by calculating the gradient of the image. Three different image energy models are used with and are given as follows:

e. Kass Energy Model

The original Snake introduced by Kass uses the energy model defined by the following equation:

$$E_{img} = -\left\|\nabla I(x, y)\right\|^2 \tag{5.4}$$

where I is the image function. As mentioned earlier, the echocardiography ultrasound images are very noisy, so the first step to be taken into account is noise reduction to allow for edge detection and to enhance the ability of Snake to capture the real contour of the LV. To reduce the noise, the image will be convolved by Gaussian kernel, making the image energy as follows:

$$E_{img} = -\left\|\nabla\left[G_\sigma(x, y) * I(x, y)\right]\right\|^2 \tag{5.5}$$

Here, $G_\sigma(x, y)$ is a two dimensional Gaussian filter and σ represents the standard deviation. Convolving the Gaussian kernel with the image using large values of σ makes the boundaries become blurry. The smoothing process in this case has an advantage and a disadvantage. The positive effect is increasing the range of attraction of the Snake. The negative effect is that the boundary localization will become less accurate and more image information will be lost.

f. Balloon Energy Model

Kass Snake will shrink instead of flattening if it is not under the influence of image energy. Cohen suggested another way of using the image energy by modifying the Kass model, which increases the capture of control points to edges [122]. The E_{img} is calculated by taking the normalization of the image energy as follows:

$$E_{img} = k_1 N(s) - k_2 \frac{\nabla E_{img}}{\left\|\nabla E_{img}\right\|} \tag{5.6}$$

In the first term, Cohen added a magnification factor multiplied by the normal vector, which gives it a dynamic behavior even though the contour does not affect the image energy. That is why it is called a balloon. The magnitude k_1 controls the value of first term and k_2 controls the value of normalized term. The disadvantage of the this model is that if the edge is too weak, like in the ultrasound images, the first term will push the curve away from the position of this weak edge.

g. GVF Energy Model

Xu and Prince introduced a new energy model for the by using the GVF (Gradient Vector Flow) [123] . The target of this improvement is to increase the capture range and improve the Snakes ability to move into boundary concavities.

GVF tackles these problems by employing a new external force, which is defined as GVF(x; y) = (u(x; y); v(x; y)). The GVF obtained from the solution that minimizes the following energy function is:

$$\varepsilon = \iint \left\{ \mu \left(u_x^2 + u_y^2 + v_x^2 + v_y^2 \right) + \|\nabla I\|^2 \|GVF - \nabla I\|^2 \right\} dxdy \tag{5.7}$$

In this functional *I(x, y)* is given by Equation (5.7). μ is a regularization parameter to control the tradeoff between the strength of the first and the second terms of the energy functional. To allow for noise compensation in noisy images, the value of μ should be high. In the proposed energy functional, if the gradient of the image has a large magnitude, the second term dominates the solution of the functional by getting GVF = ∇I. In the opposite situation, if the gradient of the image is low; the first term dominates the solution of the energy functional.

h. Choosing the Suitable Energy Model for Ultrasound Images

The three with their image energy models (Snake_Kass, Snake_Balloon, Snake_GVF) were built and tested with different 2D echocardiographic image sequences. Snake_Kass and Snake_Balloon showed better results than GVF. GVF shows instability and passes the boundaries of the LV. In comparison of Snake_Kass with Snake_Balloon,

Snake_Kass shows better performance than Snake_Balloon. According to these results, Snake_Kass is chosen to be used in the tracking framework.

5.3 SOLUTION OF THE SNAKE ENERGY FUNCTION

The objective is to find a set of Snake points [$C(s)$ =($x(s)$, $y(s)$] that minimizes the energy in Equation (5.2). By employing the calculus of variation, we will consider a valid solution $\hat{C}(s)$ agitated by a small amount $\varepsilon\delta C(s)$, by achieving a minimum energy as follows:

$$\frac{dE_{Snake}(\hat{C}(s)+\varepsilon\delta C(s))}{d\varepsilon}=0 \tag{5.8}$$

The agitation is spatial causing the x and y co-ordinates of the points to be as follow:

$$\delta C(S)=(\delta_x(s),\delta_y(s)) \tag{5.9}$$

The agitated solution of the Snake will become as follows:

$$\hat{C}(s)+\varepsilon\delta C(s)=(\hat{x}(s)+\varepsilon\delta_x(s),\hat{y}(s)+\varepsilon\delta_y(s)) \tag{5.10}$$

$\hat{x}(s)$ and $\hat{y}(s)$ represent the x and y co-ordinates of the solution $(\hat{C}(s)=(\hat{x}(s),\hat{y}(s)))$. The solution for the functional given by Equation (3.1) after replacing E_{img} with E_{Edge} will be written as:

$$E_{Snake}(\hat{C}(s)+\varepsilon\delta C(s))=\int_{s=0}^{1}\left\{E_{INT}(\hat{C}(s)+\varepsilon\delta\hat{C}(s)+E_{Edge}(\hat{C}(s)+\varepsilon\delta\hat{C}(s)\right\}ds \tag{5.11}$$

E_{INT} is given by Equation (5.3), and by replacing it in the previous equation, the solution will become as follows:

$$E_{Snake}(\hat{C}(s)+\varepsilon\delta C(s))=\int_{s=0}^{1}\begin{Bmatrix}\alpha(s)\left|\dfrac{d\left((\hat{C}(s)+\varepsilon\delta C(s)\right)}{ds}\right|^2+\beta(s)\left|\dfrac{d^2\left((\hat{C}(s)+\varepsilon\delta C(s)\right)}{ds^2}\right|^2+\\ E_{Edge}(\hat{C}(s)+\varepsilon\delta C(s)\end{Bmatrix}ds \tag{5.12}$$

The complete solution of Equation (5.10) is given in detail in [124] and we thereby arrive at the following equations:

$$f_s=a_s x_{s-2}+b_s x_{s-1}+c_s x_s+d_s x_{s+1}+e_s x_{s+2} \tag{5.13}$$

where

$$f_s=-\frac{1}{2}\frac{\partial E_{Edge}}{\partial x}\bigg|_{x_s,y_s}$$

$$a_s=\frac{\beta_{s-1}}{h^4}$$

$$b_s=-\frac{2(\beta_{s-1}+\beta_{s-1})}{h^4}-\frac{\alpha_s}{h^2}$$

$$c_s=\frac{\beta_{s+1}+4\beta_s+\beta_{s-1}}{h^4}+\frac{\alpha_{s+1}+\alpha_s}{h^2}$$

$$d_s=-\frac{2\left(\beta_{s+1}+\beta_s\right)}{h^4}-\frac{\alpha_{s+1}}{h^2}$$

$$e_s=\frac{\beta_{s+1}}{h^4}$$

The equation can be written in a linear matrix equation as:

$$Ax=f_x(x,y) \tag{5.14}$$

Where $f_x(x,y)$ is the first order of the edge magnitude along the x axis and A is given by:

$$A=\begin{bmatrix} c_1 & d_1 & e_1 & 0 & .. & a_1 & b_1 \\ b_2 & c_2 & d_2 & e_2 & 0 & .. & a_2 \\ a_3 & b_3 & c_3 & d_3 & e_3 & 0 & \\ \vdots & \vdots & \vdots & \vdots & \vdots & \vdots & \vdots \\ e_{s-1} & 0 & .. & a_{s-1} & b_{s-1} & c_{s-1} & d_{s-1} \\ d_s & e_s & 0 & .. & a_s & b_s & c_s \end{bmatrix} \tag{5.15}$$

In the same way, the linear matrix equation for y will be:

$$Ay = f_y(x, y) \tag{5.16}$$

To evolve the Snake from contour C_i to C_{i+1}, both equations will be solved iteratively as:

$$\begin{aligned} \frac{\left(x^{i+1} - x^i\right)}{\Delta} + Ax^{i+1} &= f_x(x^i, y^i) \\ \frac{\left(y^{i+1} - y^i\right)}{\Delta} + Ay^{i+1} &= f_y(x^i, y^i) \end{aligned} \tag{5.17}$$

The control factor Δ, controls the speed of evolution of the Snake. Large values cause the Snake to pass the real boundaries of the object while small values let the Snake move slowly. An appropriate value should be chosen for Δ. The final solution for the Snake after rearrangement can be given as:

$$\begin{aligned} x^{i+1} &= \left(A + \frac{1}{\Delta} I\right)^{-1} \left(\frac{1}{\Delta} x^i + f_x(x^i, y^i)\right) \\ y^{i+1} &= \left(A + \frac{1}{\Delta} I\right)^{-1} \left(\frac{1}{\Delta} y^i + f_y(x^i, y^i)\right) \end{aligned} \tag{5.18}$$

5.4 KALMAN FILTER

R. Kalman introduced his seminal paper in 1960 describing a computationally recursive solution to the problem of discrete data linear filtering. The paper was entitled "A new approach to linear filtering and prediction problems" [125].

Since that time, the Kalman filter became a vast research point and application, especially in the area of navigation and automation [126]. Using the least square method, the Kalman filter affords an adequate solution to the set of mathematical equations in a recursive way. The solution is optimum because it minimizes the estimated error covariance under the condition that some assumptions are met. This efficiency comes from its ability to support the estimation of past, present and future; even if we do not know the precise nature of the modeled system [127].

The estimation of the process in the Kalman filter framework is done in the form of feedback control; by estimating the process state at some point in time and allowing feedback to come from the noisy measurement. Kalman filter equations can be classified into two stages; the time update and measurement update equations. The time update equation uses the current state and error covariance to get the a priori estimates for the next time step, while the function of measurement update equations is to provide feedback by assimilating a new measurement into the a priori estimate to get an enhanced a posteriori estimate. In the literature, the time update equations are known as predictor equations while the measurement equations are known as the correction equations. Figure (5.1) represents the estimation algorithm by using time update (prediction) and measurement update (correction) equations.

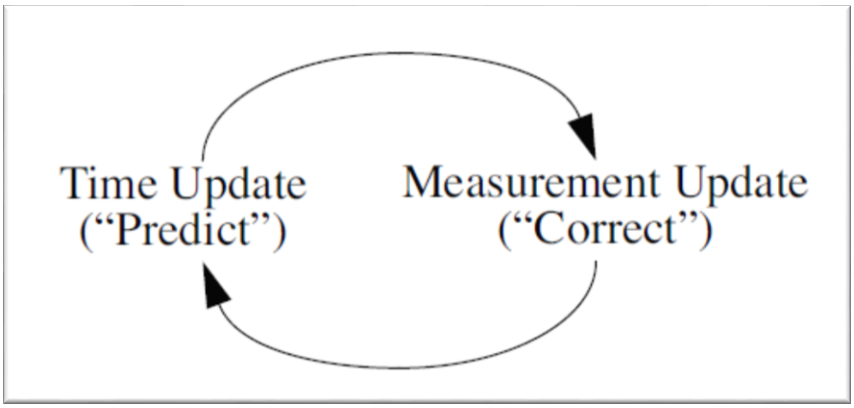

Figure (5.1) – The estimation algorithm by using time update and measurement update stages

The standard Kalman filter can be used to estimate the state of a discrete-time process, only if this process is governed by a linear stochastic difference equation. In our case, as mentioned earlier, the LV is highly nonlinear system. Our approach is to use Extended Kalman Filter or EKF which based on linearizing the system equation about the current mean and covariance [128].

a. Extended Kalman Filter Equations

The equations for the EKF are given as follows [128]:

- State equation:

$\tilde{x}$) (5.19)

- Jacobian equation:

$$H = J = f'(\hat{x}_k) \tag{5.20}$$

- Kalman gain

$$K_k = P_k H^T (HP_K H^T + R)^{-1} \tag{5.21}$$

- Error covariance matrix

$$P_{k+1} = (I - K_k H) P_k \tag{5.22}$$

- Next estimate will equal

$$\hat{x}_k = \tilde{x} \tag{5.23}$$

5.5 TRACKING THE LV BOUNDARIES USING EKF FRAMEWORK

The approach to track the LV contour in the echocardiographic image sequence will be performed in a sequential state estimation fashion, using the extended Kalman filter (EKF) to recursively predict and update LV contour deformations. EKF is used to integrate the advantages of mathematical physical models and time-series models. Measurement information is used to find and eliminate modeling errors, errors in the input and errors in the parameters. Model information is used to eliminate outliers in the measurements.

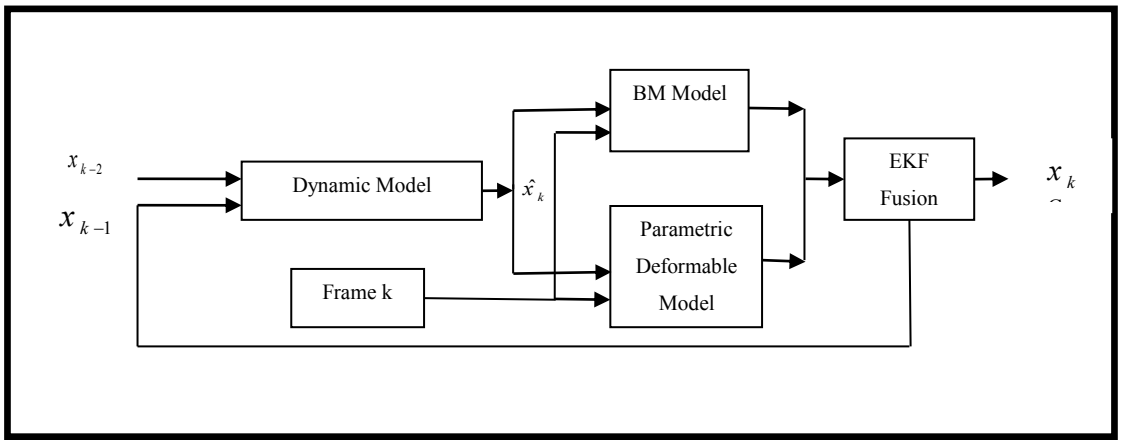

Figure (5.2) Processing frames starting from second frame for EKF framework

In the designed work, we will see the tracking as a probabilistic inference problem. The probabilistic framework is essential for dealing with classes of shapes and motions [129]. In order to track the shape of the LV (non-rigid time-varying object), a second order dynamic model is used to predict the contour state. A deformable model is used to describe the shape changes in the LV that deforms through time. The function of the deformable model is to transform the contour points (*C*) into deformed points using a state vector (*x*) as parameters. The Jacobian matrix is also computed in this stage. The BM model is used to estimate the LV deformation, which will be treated as measurement stage. In the last stage, the predicted contour from the deformable model and the estimated contour from the BM model will be fused together to compute the final contour of the LV. Figure (5.2) illustrates the tracking framework.

a. Prediction Stage

The predicted state of the LV contour will be provided by the dynamic model. To enable modeling of motion, in addition to position, a second-order dynamic model is proposed to be used as follows [129]:

$$\hat{x}_{k+1} = A_1\hat{x}_k + A_2\hat{x}_{k-1} + (I - A_2 - A_1)\bar{x} \tag{5.24}$$

The technique that takes the contour at time step *k-1* as an initial contour to the time step *k*, is lacking a mechanism to extrapolate the motion between frames and it is only suitable

for objects that have slow motion. If the posterior at time k is handed on as prior to the time step *k-1*, it will cause the measurement information to accumulate and the covariance will decrease to zero. The system with zero covariance will put greater emphasis on the predication state meaning the measurement will have no effect in the estimated contour [129]. The suitable framework should provide a contingency plan for possible motions, the deformation of the shape and a deterministic part which gives the expected displacement between the successive frames. This dynamic, prior distribution must be applied between all pairs of successive frames [129].

To overcome these shortcomings, a second order dynamic process is used in the tracking framework. The second order dynamic process provides the temporal and spatial coherence between frames to insure robustness of the performance. Instead of one frame, two successive frames are used to increase the robustness and accuracy of the LV boundary detection. $\hat{x}_k$ represents the state of the LV contour at the k^{th} frame and $\hat{x}_{k-1}$ represents the state of the LV contour at frame *k-1*.

b. Dynamical learning problem

The coefficients in the second order dynamical model which are the matrices A_1, A_2, the mean $\bar{x}$ and the variable $\hat{D}$ that used to calculate the mean. These parameters that describe the dynamics of the moving shape of LV can be obtained through dynamical learning algorithm given by [129, 130] . Using a set of manually outlined contours of the LV boundaries for a one cardiac cycle from an image sequence, we can compute these parameters. The manually outlined contours for the one cardiac cycle are used as training set which are outlined by a cardiologist. The following algorithm is used to get the matrices A_1, A_2, $\hat{D}$ and the mean $\bar{x}$.

c. The Learning Algorithm

1. First step is calculating the summations which are representing the auto-correlation coefficients where, *i, j*= 0, 1, 2. The three summations are computed with the following formulas:

$$R_i = \sum_{k=3}^{M} X_{k-i} \tag{5.25}$$

$$R_{ij} = \sum_{k=3}^{M} X_{k-i} X^T_{k-j} \tag{5.26}$$

$$R'_{ij} = R_{ij} - \frac{1}{M-2} R_i R_j^T \tag{5.27}$$

2. Estimating the parameters by utilizing the following formulas:

$$\hat{A}_2 = \left(\hat{R}_{02} - \hat{R}_{01}\hat{R}_{11}^{-1}\hat{R}_{12}\right)\left(\hat{R}_{22} - \hat{R}_{21}\hat{R}_{11}^{-1}\hat{R}_{12}\right)^{-1} \tag{5.28}$$

$$\hat{A}_1 = \left(R'_{01} - \hat{A}_2 R'_{21}\right) R'^{-1}_{11} \tag{5.29}$$

$$\hat{D} = \frac{1}{M-2}\left(R_0 - \hat{A}_2 R_2 - \hat{A}_1 R_1\right) \tag{5.30}$$

3. The mean $\bar{x}$ is estimated from the following formula:

$$\bar{x} = \left(I - \hat{A}_2 - \hat{A}_1\right)^{-1} \hat{D} \tag{5.31}$$

4. The following formula is used to estimate the covariance coefficient B_0 as a matrix square root $B_0 = \sqrt{\hat{C}}$, where the matrix C estimated by the following formula:

$$\hat{C} = \frac{1}{M-2}\left(R_{00} - \hat{A}_2 R_{20} - \hat{A}_1 R_{10} - \hat{D} R_0^T\right) \tag{5.32}$$

After obtaining the parameters of the motion dynamic model, these parameters will be used to estimate the *a priori* error covariance matrix that will be used in the combining process. For the second order dynamic system, the more advanced formula will be used to estimate the *a priori* error covariance matrix as follows given by [131]:

$$\bar{P} = A_2 P_{k-2} A_2^T + A_1 P_{k-1} A_2^T + A_2 P_{k-2}^T A_1^T + A_1 P_{k-1} A_1^T + v \tag{5.33}$$

d. Detecting the Contour by the Deformable Model (Snake)

After the second order dynamic model predicts the contour, in this stage, the deformable model (Snake) will evolve the control points to the boundaries of the LV from the current frame of the image sequence giving the contour. At the same time, the Jacobian matrix will be computed using the formula (5.34) as follows:

$$H = \begin{bmatrix} \frac{\partial C_1}{\partial x_1} & \frac{\partial C_1}{\partial x_2} & \cdots & \frac{\partial C_1}{\partial x_n} \\ \vdots & \ddots & \vdots & \vdots \\ \frac{\partial C_n}{\partial x_1} & \frac{\partial C_n}{\partial x_2} & \cdots & \frac{\partial C}{\partial x_n} \end{bmatrix} \tag{5.34}$$

The Jacobian matrix or the measurement vector H will be used later in the next step to compute other important variables.

e. Measurement Stage

The second stage in the tracking system is the measurement where the LV boundaries are estimated by utilizing the BM model (x_k^{BM}). (x_k^{BM}) represents the measurements obtained in the k^{th} frame. In this stage also, we will calculate the matrix R, which will be used later to calculate the Kalman gain. The matrix R represents the uncertainty in the measurement process. The uncertainty of measurement represents the doubt that exists about the contour that was obtained from the BM model. There are two methods of calculating the uncertainty; Type A and Type B estimations. Type A uncertainty estimation is used by applying statistics to estimate the uncertainty when there are multiple readings. . In Type B estimations, the uncertainty is evaluated from any other information like past experience of the measurements, calibration certificates, from calculations, from published data and from common sense [132, 133]. In our case, only a single measurement is available at each frame, so Type A is not applicable. In Type B the real value of the contour of LV is unknown to us, so it is not applicable for use either. To overcome this difficulty, an auto covariance, least squares estimation method will be used to calculate uncertainty in the BM model contour calculation. In this approach, it is assumed that the initial estimation for the uncertainty of measurement R is given R_0. R will be estimated by the following formula:

$$R_k = E\left[e_k e_k^T\right] = H\bar{P}H^T + R_{k-1} \tag{5.35}$$

where

$$e_k = x_k^{BM} - x_k^{Snake} \tag{5.36}$$

f. Correction Stage

After deriving the measurement value, the correction step takes place to get the actual contour. The most important factor is the Kalman gain, which will be calculated by utilizing formula (5.29). After obtaining the Kalman gain, we will be able to obtain the final contour for LV endocardial by using the correction formula written as:

$$\hat{x}_k = x_k^{Snake} + K_k(x_k^{Snake} - x_k^{BM}) \tag{5.37}$$

After this step, we need to update the error covariance P_{k+1} to a new value using the new value of Kalman gain by utilizing the following formula:

$$P_k = (I - K_k H)\bar{P}_k \tag{5.38}$$

5.6 Tracking the LV Boundaries using Averaging Framework

An alternative approach is used to get more accurate results. Improvements are done to the EKF framework by replacing the EKF fusion with an averaging approach. The BM model and Snake control points are averaged to create the fusion contour. The fused contour is then followed by the Level set deformable model at the end of the framework to improve the final contour after fusion process. Figure (5.3) illustrates the block diagram of the framework.

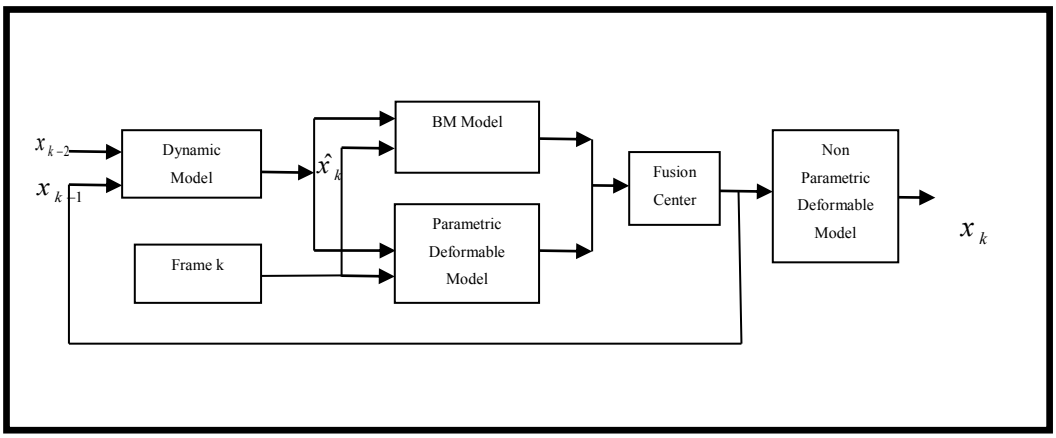

Figure (5.3) Framework of the averaging approach

a. Fusion using Averaging Technique

This procedure is based on establishing one-to-one correspondence between the control points of the Snake and BM model contours [134]. The control points of each contour start at the base of LV at the left side of the image and the last point is at the right side of the base of the LV. This means the correspondence is already established between the control points of the Snake and BM contours. The first step in the averaging fusion technique is to compute the average contour C_{avg} using the following formula:

$$y_i = \frac{1}{M}\sum_{j=1}^{M} x_{ji} \tag{5.39}$$

After getting the average curve at each point on this curve, a normal to the curve is calculated. An efficient method is used to compute the normal given by [135], based on a 2×2 scatter matrix given as follows:

$$A = \begin{bmatrix} a_{11} & a_{12} \\ a_{21} & a_{22} \end{bmatrix} \tag{5.40}$$

The matrix A is given by following formula:

$$A = \frac{1}{\sum_i \left[(x_i - \bar{x})^2 + (y_i - \bar{y})^2 \right]} \begin{bmatrix} \sum_i (x_i - \bar{x})^2 & \sum_i (x_i - \bar{x})(y_i - \bar{y}) \\ \sum_i (x_i - \bar{x})(y_i - \bar{y}) & \sum_i (y_i - \bar{y})^2 \end{bmatrix} \quad (5.41)$$

First, the eigen values of the matrix are calculated and represented as α_M *and* α_m . After that, the orthonormal eigenvectors (a_M,a_m) are calculated using the following formula:

$$a_M = \frac{(a_{12}, \alpha_M - a_{11})}{\sqrt{a_{12}^2 + (\alpha_M - a_{11})^2}} \quad (5.42)$$

$$a_m = \frac{(a_{11} - \alpha_m, a_{12})}{\sqrt{a_{12}^2 + (\alpha_M - a_{11})^2}} \quad (5.43)$$

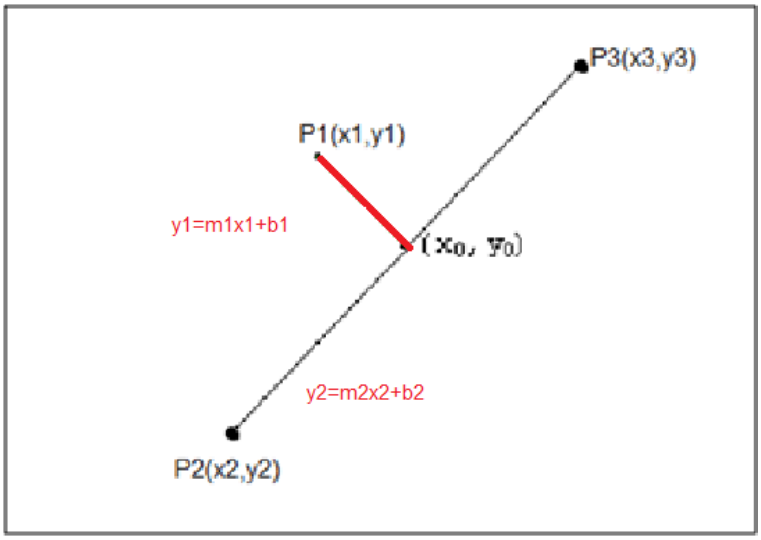

Figure (5.4) - Computing the intersection point

After computing the normal, the intersection between the normal vector with BM and Snake contours will be computed. Let the point P_1 on the C_{avg} contour, the normal is a_m (estimated from the Eigen vector above), so the equation at P_1 is given by:

$$y_1 = a_m x_1 + b_1 \quad (5.44)$$

The constant b_1 will be computed from $P_1(x_1, y_1)$ as follows:

$$b_1 = y_1 - a_m x_1 \quad (5.45)$$

In order to find the point where the two contours intersect with the normal line, the difference between the interpolations of the normal with each contour must first be calculated. Then, again using the interpolation, the value of x will be located at the position where the difference is equal to zero (the point of the intersection is where the two lines are equal). From x value, the y axis point will also be computed using interpolation. These intersection points give us a new correspondence between the Snake and BM contours, which will be averaged again using Equation (5.38). This procedure will be iterated until we find there is no change in the computed averaged points. Usually the iteration process takes five iterations to compute the final averaged contour.

The same procedure will be done with the Snake contour to find the intersection with the C_{avg} contour. These intersection points give us a new correspondence between BM and Snake contours which will be averaged again using Equation (5.38). This procedure will be iterated until we find there is no change in the computed averaged points of the Snake and BM contours. Usually the iteration process takes five iterations to compute the final averaged contour [134].

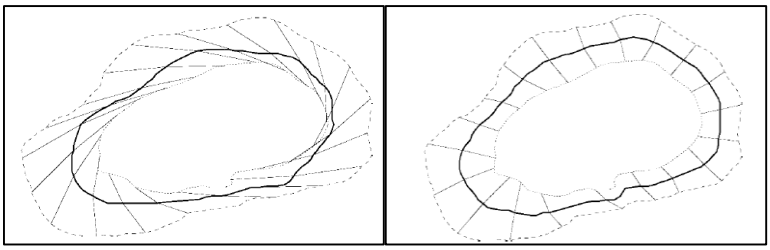

Figure (5.5) Averaging steps, firstly: finding the correspondence between each control points in both contours and lastly, the averaged contour with the bold line [134]

5.7 Level Set Deformable Model

As mentioned in section 2.5, Level set method is a non-parametric deformable model (no control points). It is chosen as a correction stage after the fusion center due to its ability to detect the topologies of objects. A level set introduced by Li *et al.* [136] is used in this framework. The following vibrational formulation is introduced by the authors:

$$\varepsilon(\phi) = \mu\rho(\phi) + \varepsilon_{g,\lambda,\nu}(\phi) \tag{5.46}$$

The first term is the penalization term that characterizes how is close the function ϕ to the signed distance function. The parameter μ controls this term. The first term is given by the following formula:

$$\rho(\phi) = \int_{\Omega} \frac{1}{2}\left(|\nabla\phi| - 1\right)^2 dxdy \tag{5.47}$$

The second term is the amount of energy that drives the motion of the zero level curve of ϕ, and is given as follows:

$$\varepsilon_{g,\lambda,\nu} = \lambda L_g(\phi) + \nu \mathrm{A}_g(\phi) \tag{5.48}$$

The parameters, $\lambda > 0$ and ν are constants. The terms L_g and A_g are given as follows:

$$L_g(\phi) = \int_{\Omega} g\,\delta(\phi)\left|\nabla(\phi)\right| dxdy \tag{5.49}$$

and

$$A_g = \int_{\Omega} gH(-\phi)\,\mathrm{dxdy}$$

The edge indicator function is represented by letter *g* and is given as follows:

$$g = \frac{1}{1 + \left|\nabla \mathrm{G}_{\sigma} * I\right|^2} \tag{5.50}$$

H here represents the Heaviside function. The gradient flow that minimizes the function ε is given as: $\frac{\partial\phi}{\partial t} = -\frac{\partial\varepsilon}{\partial t}$.

The level set will run for a few iterations because the fused contour is too close to the real contour and it corrects only the parts that have a small error. . In most cases, the contour of the level set is too close to the fused contour. In cases where neither Snake nor BM can follow the LV contour, the level set completes the job and detects the LV contour precisely.

5.8 SUMMARY

This chapter presents detailed information about the deformable model (Snake), its energy functions and the solution for minimizing its function using variations of calculus. A brief description of the Kalman filter is presented. The extended Kalman filter as an fusion center for nonlinear systems, along with its equations, is also introduced. The tracking framework and the dynamic equation for the predication stage are given in detail. The combination process is first given by using the EKF framework with its shortcomings. The averaging framework is introduced as alternative solution to the EKF framework.

CHAPTER 6 CREATING GOLD STANDARD, EXPERIMENTAL RESULTS AND EVALUATION

6.1 INTRODUCTION

In the area of medical image analysis, researchers developed a lot of segmentation algorithms to extract the contours of different body organs from different medical image modalities. These segmentation algorithms need to be evaluated on a large set of clinical data. This step is important to validate the segmentation algorithms and to be clinically applicable. In the literature, very few researchers evaluate their algorithms on a large number of clinical data sets [134].

If we know the expected result then we can use it as gold-standard segmentation. The segmentation output from the computer will be compared with this gold standard. The output of the segmentation algorithm must be compared with a large number of clinical data sets to test and make sure it is not statistically different from the gold standard [134]. The gold standard was created by manual plotting of three cardiologists. The evaluation of the biomechanical model and the whole framework performance against the gold standard is also given.

6.2 DIFFICULTIES FACING THE EVALUATION OF MEDICAL IMAGE SEGMENTATION

The evaluation of medical image segmentation is not an easy task. The difficulties can be summarised in the following points [134]:

1- There are no standard criteria to define the gold standard. In medical image segmentation, the only way to proceed with evaluation is to compare the automated results against the manual outlining of the experts. The manual outlining of the experts alone cannot be taken as the gold standard due to observer bias and inter and intra observer variability.

2- There is difficulty in defining a metric to compare the automated with manual results. In medical image segmentation, the complexity of multidimensional segmentation data makes the definition of metric very difficult.

3- There are no standardized statistical protocols to judge the performance of automated algorithms. The difficulty in defining standard statistical protocols comes from the lack of gold standard and the lack of metrics.
4- Collecting large data with expert manual outlining is very tedious and time consuming work.

6.3 CREATING THE GOLD STANDARD

To overcome the problem of the lack of a gold standard, Chalana *et al.* [134] developed a method to create a gold standard for comparing an automated contour with manually plotted contours.

a. Creating Manually Plotted Contours

The automated contour will be compared and tested with three manually plotted contours, traced by different cardiologists. Comparing the results of the automated contours to only one observer's outline may not be sufficient, because a single observer's tracing may be subjected to the observer's bias or inter-observer variability.

b. Creating the Gold Standard

To create the gold standard, the manually plotted contours are averaged by the same method that we used in averaging the Snake and BM models; as introduced in section 5.6.1. The methodology explained above is applied to ten samples from five different patients. In each case, an image of EDS and ESS are chosen so we can compute the ejection fraction for the patient. All the images are outlined by three observers. The three contours of each sample are used to create the gold standard of that sample. The following figures show the tracing of each observer and the created gold standard after applying the mentioned methodology. In each image, Observer_1 is represented by the green color; observer_2 is represented by the blue color and observer_3 is represented by the yellow color. The gold standard is depicted in red color.

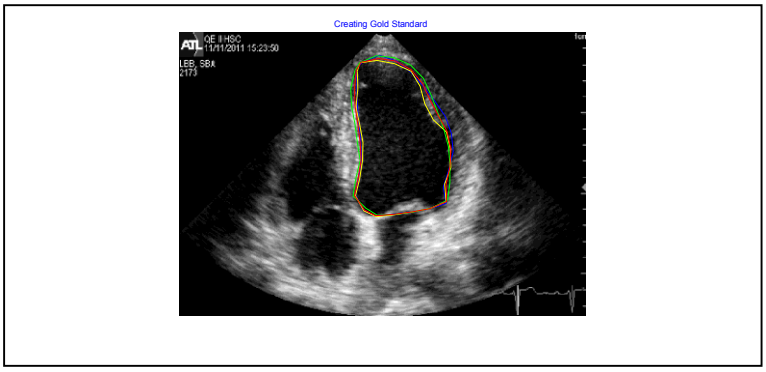

Figure (6.1) – Sample No. 1 ED, Observer_1 (green), observer_2 (blue), observer_3 (yellow) and gold standard (red)

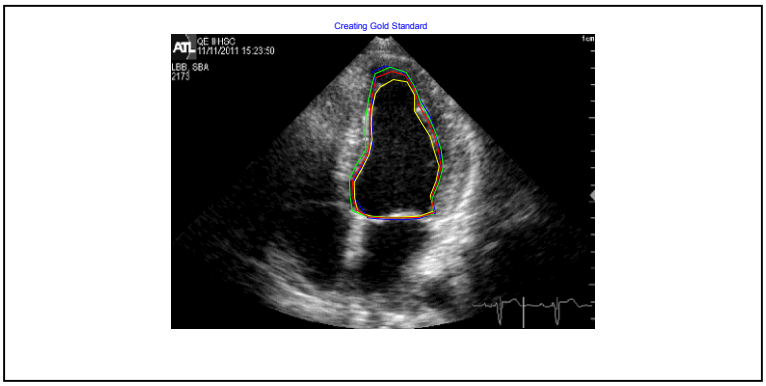

Figure (6.2) – Sample No. 2 ES, Observer_1 (green), observer_2 (blue), observer_3 (yellow) and gold standard (red)

In the first sample, Figure (6.1) shows the EDS and Figure (6.2) shows the ESS for the same patient where a four chamber view is used in this case.

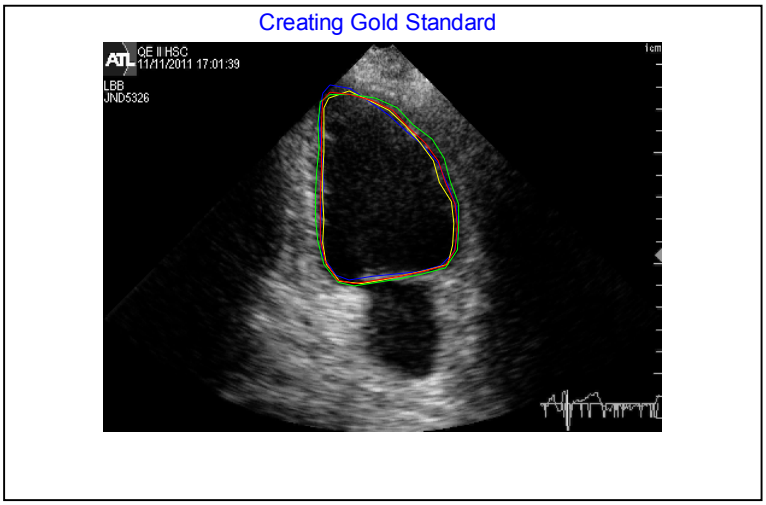

Figure (6.3) – Sample No. 3 ED, Observer_1 (green), observer_2 (blue), observer_3 (yellow) and gold standard (red)

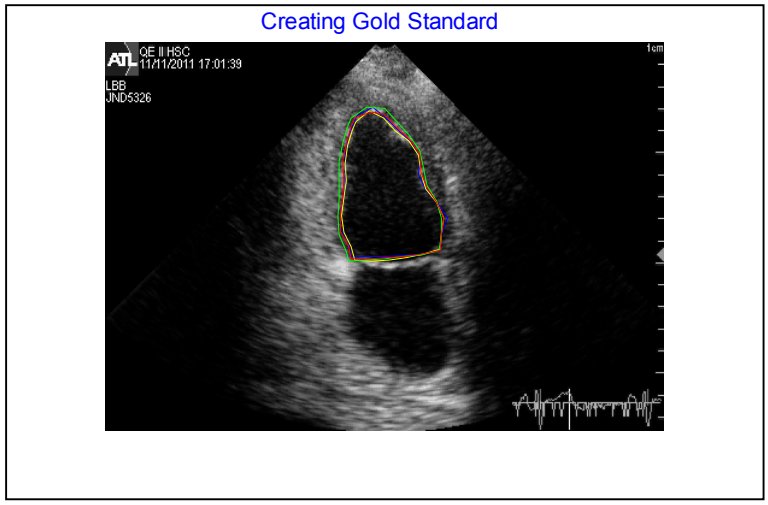

Figure (6.4) – Sample No. 4 ES, Observer_1 (green), observer_2 (blue), observer_3 (yellow) and gold standard (red)

In the second sample, Figure (6.3) shows the EDS and Figure (6.4) shows the ESS for the same patient where a two chamber view is used in this case.

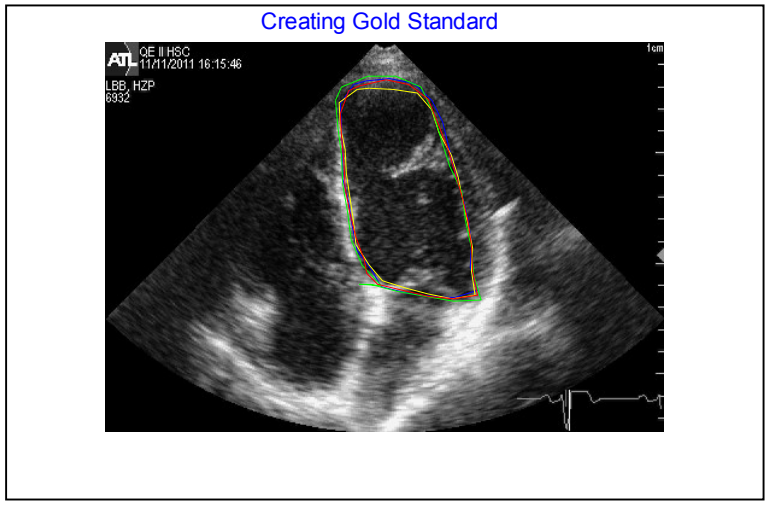

Figure (6.5) – Sample No. 5 ED, Observer_1 (green), observer_2 (blue), observer_3 (yellow) and gold standard (red)

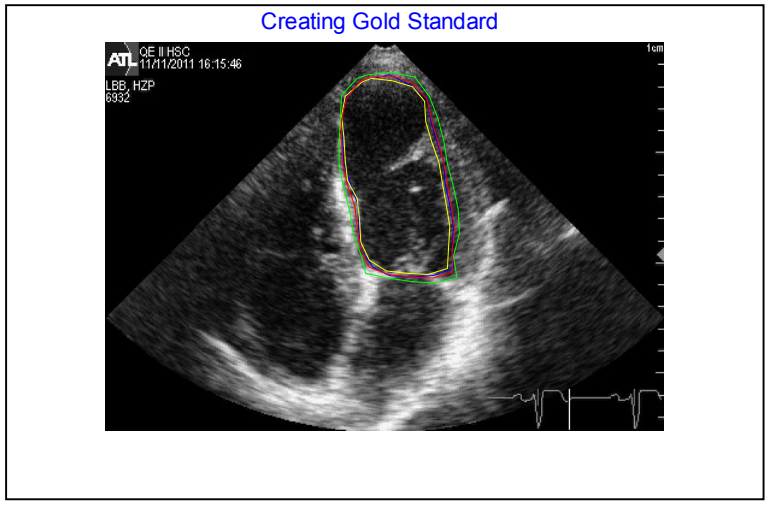

Figure (6.6) – Sample No. 6 ES, Observer_1 (green), observer_2 (blue), observer_3 (yellow) and gold standard (red)

In the third sample, Figure (6.5) shows the EDS and Figure (6.6) shows the ESS for the same patient where a four chamber view is used in this case. This patient is suffering from severe abnormality and dysfunction.

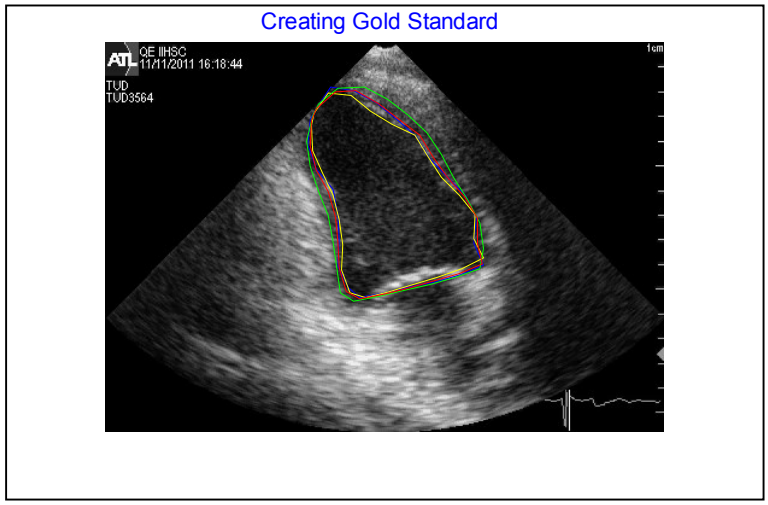

Figure (6.7) – Sample No. 7 ED, Observer_1 (green), observer_2 (blue), observer_3 (yellow) and gold standard (red)

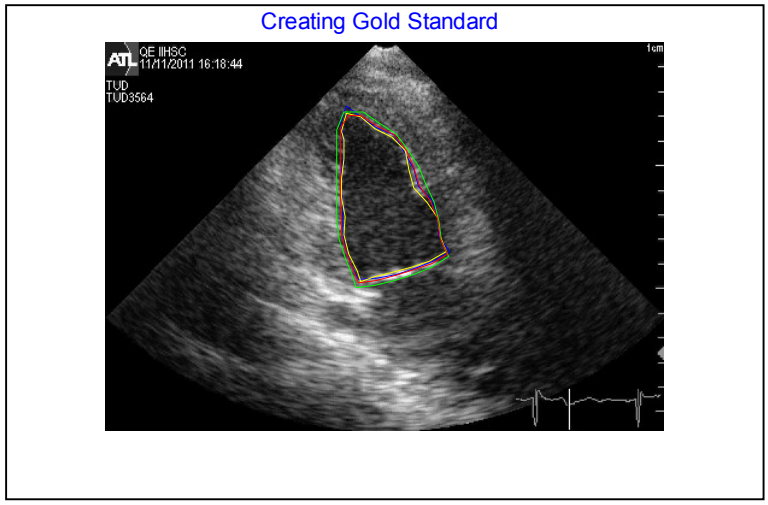

Figure (6.8) – Sample No. 8 ES, Observer_1 (green), observer_2 (blue), observer_3 (yellow) and gold standard (red)

In the forth sample, Figure (6.7) shows the EDS and Figure (6.8) shows the ESS for the same patient where a two chamber view is used in this case. This sample is noisy and the images have signal dropout at the boundaries of the LV.

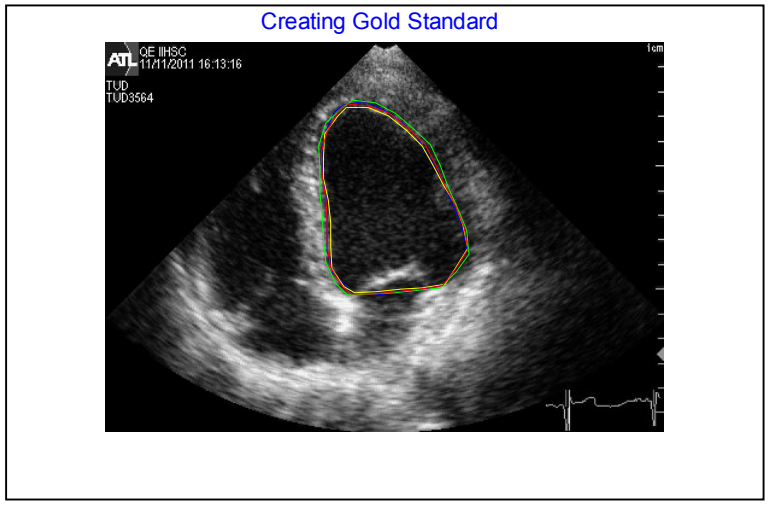

Figure (6.9) – Sample No. 9 ED, Observer_1 (green), observer_2 (blue), observer_3 (yellow) and gold standard (red)

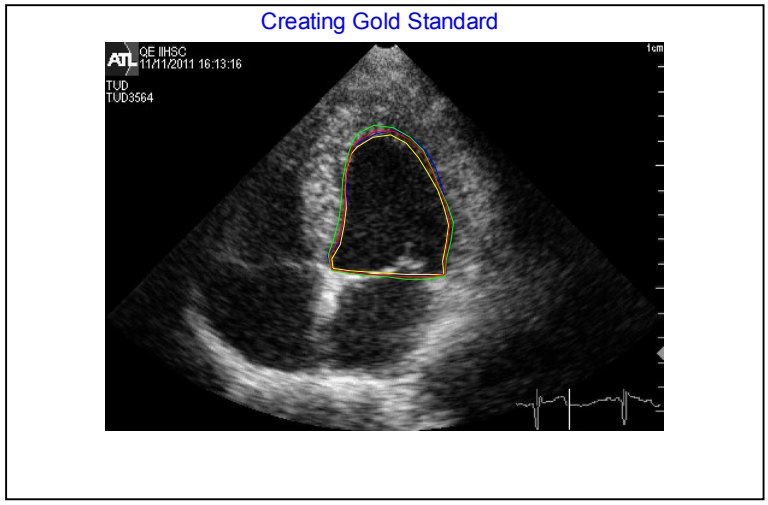

Figure (6.10) – Sample No. 10 ES, Observer_1 (green), observer_2 (blue), observer_3 (yellow) and gold standard (red)

In the fifth sample, Figure (6.9) shows the EDS and Figure (6.10) shows the ESS for the same patient where a four chamber view is used in this case.

In the all cases and images, there is mismatch between all the observers outlining which is called intra observer variability [137]. All the X-Y coordinates' data of the ten samples are given in the listed ten tables in appendix IV.

6.4 Error Metric

In medical image segmentation, the first step is choosing which parameter will be compared. The comparison can be done on the boundaries or in the parameters that will be derived from the boundaries, such as the enclosed area. For the LV tracking and segmentation, the most important derived parameters are the enclosed area at the end of the systole and the end of the diastole. Evaluation based on these derived parameters will not be accurate because in some cases the automated derived parameters are in complete agreement with the manually measured parameters; but the boundaries from which these measurements were derived were not in agreement. To avoid this complication, the comparison of the automated contour with gold standard will be based on the absolute difference as a distance metric. The Average Perpendicular Distance (APD) will be used to evaluate the detected contour of the framework by comparing it to a gold standard created from three manual outlined contours traced by three cardiologists.

APD measures the match between two segmented contours by finding the average of the perpendicular distances between two corresponding points in the contours. A high value indicates that the two contours do not match closely. APD is chosen due to its ability to detect very small variations in the compared contours without computational complexity. APD uses distance as a measure of shape matching, unlike the other methods that use area. This is because two contours can have an almost identical area but quite different shapes. APD satisfies the following requirements to be a metric distance:

1. $e(A, A) = 0 \; and \; e(A, B) \geq 0$
2. $e(A, B) = e(B, A)$
3. $Triangle \; inequality: e(A, C) \leq e(A, B) + e(B, C)$

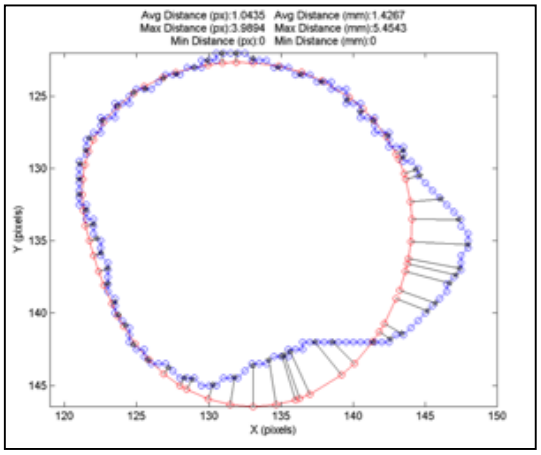

Figure (6.11) - Average perpendicular distance [138]

To calculate the APD at each point in the automated contour, $P_{auto}(x, y)$, the first step is finding the intersection points between the automated contour and the gold standard. We used the same procedure as mentioned in section 5.6.1. After finding the intersection point $P_{intersect}(x_0, y_0)$, the distance will be measured between the automated contour and the intersection point using the following formula:

$$APD = \sqrt{(x - x_0)^2 + (y - y_0)2} \tag{6.1}$$

6.5 EXPERIMENTAL RESULTS

Many experimental results are conducted to verify the output of the BM model, deformable models and the fused contour.

a. BM Model Experimental Results

As mentioned in Chapter 4, the tracking started at the end of the QRS of the ECG signal which represents the end of diastole and starting of the systole phase.

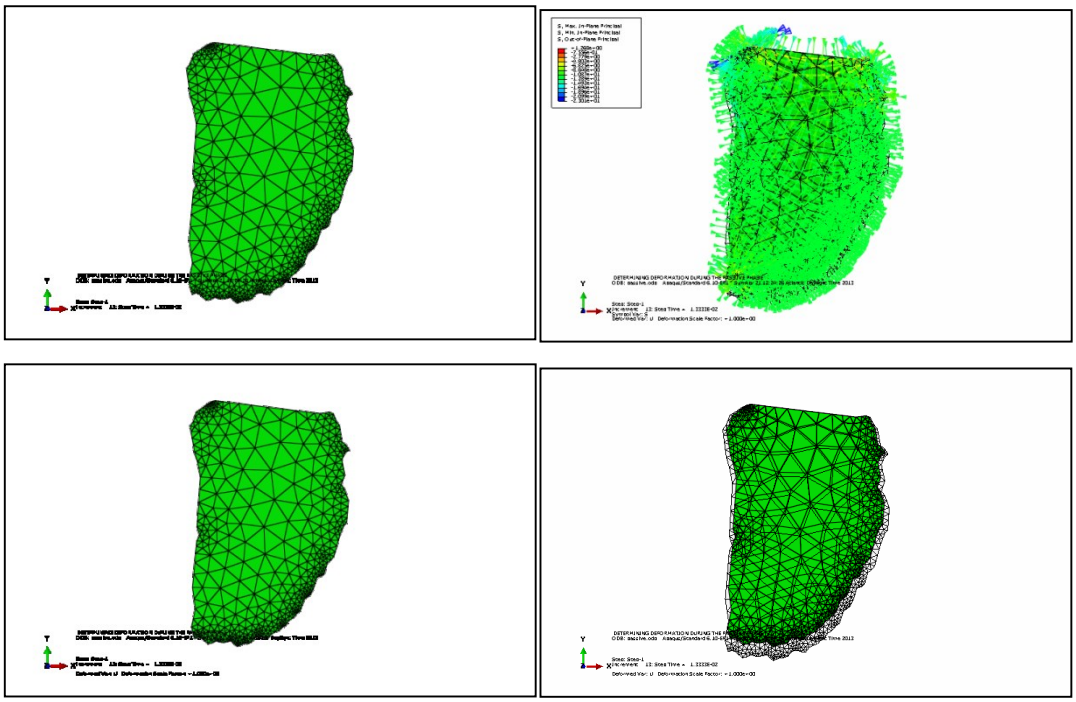

Figure (6.12) - Undeformed shape, applied load, deformed and superimposed shape of the LV at the contraction phase for the four chamber view

The FEM will run for a certain time and a certain pressure (load) applied to the LV boundaries according to the frame number. In Figure (6.12), the load is positive in the contraction phase and applied at all the faces of the elements at the boundary of the LV. This positive pressure (symbols pointing toward the LV boundaries) will let the LV boundaries contract and the area of the LV will be less in the deformed shape. No pressure is applied at the base because it is not part of LV muscles and this area should be kept fixed to avoid the rigid body motion, as explained in Chapter 4.

After the end of running of FEM, the LV will contract and the deformed shape will be as shown in the third image of Figure (6.12). A sample of the resulted LV deformation values during the contraction phase in given in the appendix II. As illustrated in the list, some deformations have negative values and others have positive values according to position of the nodes at the LV boundaries. The zero deformations are located at the base as mentioned in chapter 4 to avoid the rigid body motion. The forth image shows a superposition of the undeformed and deformed shapes of the LV before and after contraction. As in the real LV, additional contractions will occur at the apex and lateral wall, while fewer contractions will occur at the septal.

The next images show the results of applying the BM model in the passive phase. The first image in Figure (6.13) shows the undeformed shape before applying the load.

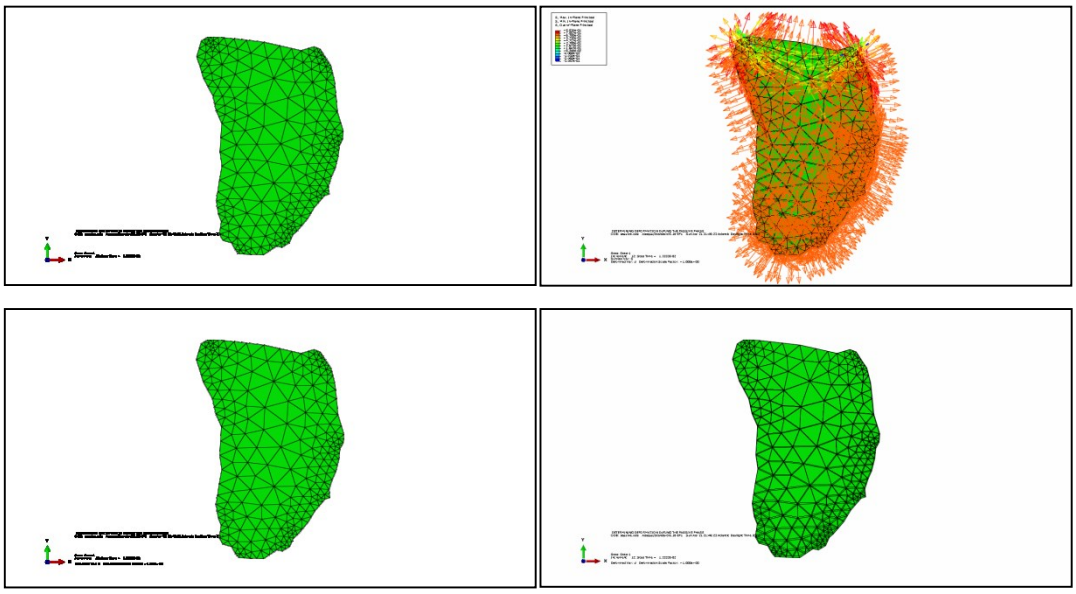

Figure (6.13) - Undeformed shape, applied load, deformed and superimposed shape of the LV at the relaxation phase for the four chamber view

In the second image, the load is applied to the undeformed shape to let it relax to simulate the passive phase. As shown in the figure, the pressure in this case is negative (arrows are pointing outward), to let the LV boundaries expand to simulate the relaxation of the LV muscles in the passive phase. As mentioned in the contraction results, no

pressure is applied at the base; pressure is only applied to the faces of the elements at the LV boundaries. The third image in the figure shows the LV shape after applying the load. Appendix III shows the list of LV deformations after the completion of the running of ABAQUS. The deformation values in the passive phase are less than the deformations in contraction phase. The reason behind this is the force of the contraction and the applied load is more during the contraction to let the LV has the enough power to eject the blood to the whole body. This will result to have more deformations than in the passive where the LV is just relaxing and expand during the filling stage.

In fourth image, the undeformed and the deformed shapes are superimposed together to show the amount of deformation that happened after applying the load.

Two chamber view results are given in the next figure to show the performance of the BM model in the active phase. Figure (6.14) shows two chamber views for the LV before applying the load, which represents the undeformed shape of the LV for the BM model.

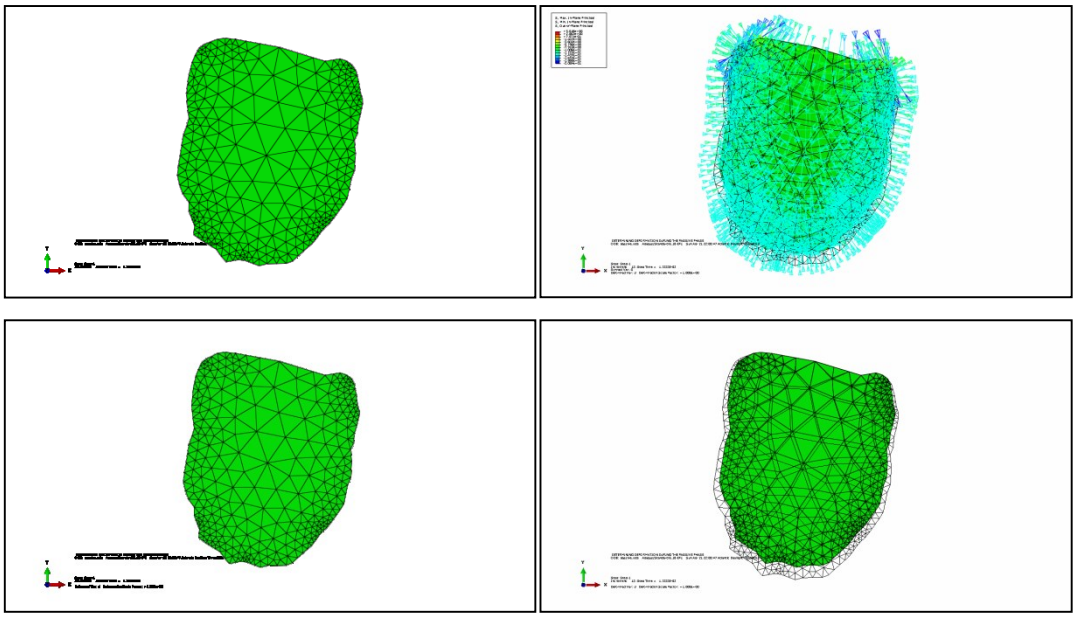

Figure (6.14) - Undeformed shape, applied load, deformed and superimposed shape of the LV at the contraction phase for the two chamber view

The second image in Figure (6.14) shows the load applied to all the element faces at the LV boundaries to let the LV contract. The next image in the figure shows the

deformed shape of the LV after applying the load. In the last image, both the undeformed and deformed shapes of LV are represented in one figure to show the amount of deformation that occurred during the contraction of the LV.

At the passive phase, the same two chamber view image is used to show the deformation measured by the BM model.

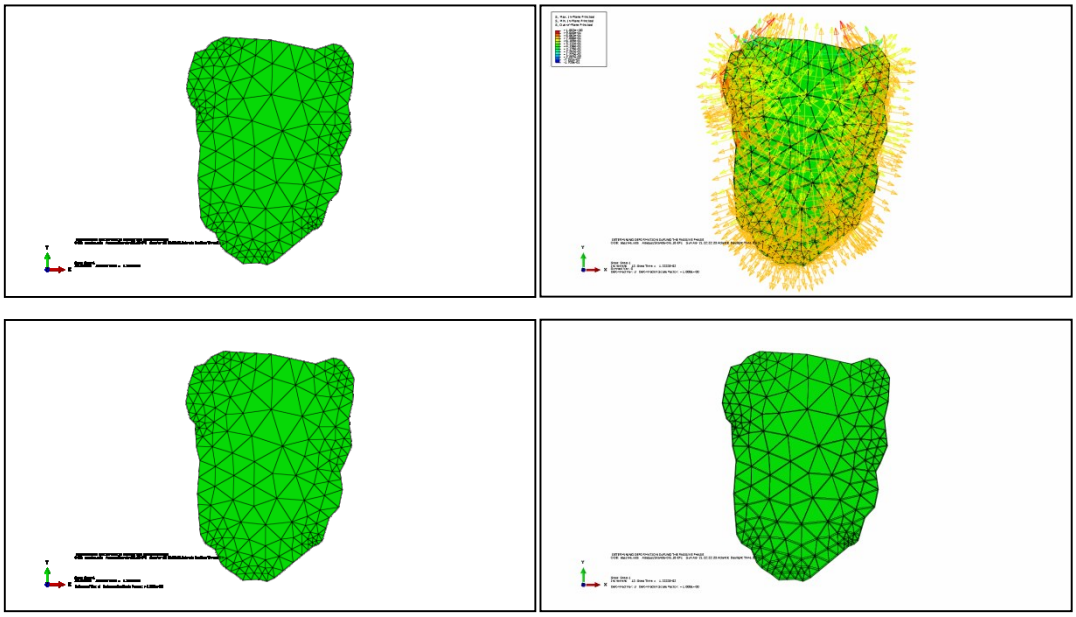

Figure (6.15) – Undeformed shape, applied load, deformed and superimposed shape of the LV at the relaxation phase for the two chamber view

b. BM, Snake, Fused and Level Set Contours Experimental Results

In this section, the results of applying the BM, the Snake and the final contour will be shown as superimposed in the ultrasound images of the echocardiographic images. The same images that were used in the previous section will be used here to show all of the contours. In all cases of the experimental results, the BM model contour will appear blue, the Snake contour will appear red, while the final contour will appear green in the EKF frame work; and yellow in the averaging framework.

c. EKF Framework Experimental Results

In this section, the experimental results achieved by using the EKF framework will be shown and discussed.

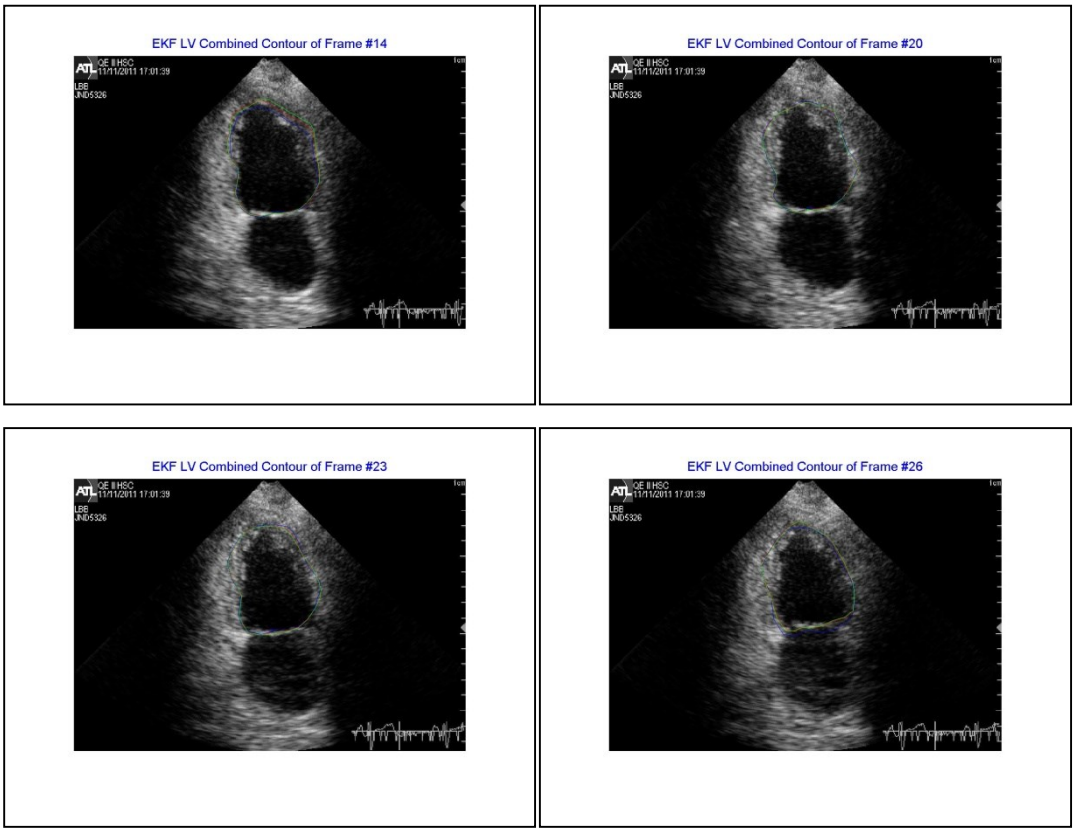

Figure (6.16) – EKF framework results for two chamber view plotting contours

In Figure (6.16), one sample of using the EKF framework to track the LV is shown. The Snake, BM model and the fused contours are always away from the real boundaries of the LV. There is no improvement in the Snake contour or in the fused one. Especially, when we approach the end of systole, as shown in the first image of the figure, all the contours are outside the ROI. After the end of systole, when the LV starts to expand, the contours are still away from the real contours, as shown in the last three images.

d. Limitations of EKF to Improve the Fused Contour

The results from EKF framework are unacceptable. The EKF could not improve the fusion contour for the following reasons:

- "The EKF is an approximate technique for Bayesian filtering of nonlinear models with Gaussian noises. It is known to work well when the nonlinearities are not severe and the distribution of the disturbances is a mutually independent zero-mean Gaussian with known variance. When these conditions are not met, the filter is known to fail" [139, 140].
- The mean and variance state vector should be known in advance to start the recursive algorithm and there is general assent to find these initial values [141] .
- The covariance matrices of EKF need to be tuned [139, 140].
- If the initial estimate is wrong, the filter is quickly diverged.
- The Kalman filter framework assumes that the uncertainty of the measurement (BM model contour) and covariance error of the model (Snake) are known and given. These values cannot be calculated, especially the uncertainty of BM, contour because the real contour is unknown to us.
- The assumption of local linear localization is not always valid. The linearization process produces a highly unstable filter, which leads to divergence phenomena [142-144] .
- The EKF framework consists of a system model (Snake) and a measurement model (BM model). According to Equation (5.36), the Snake dominates the fused contour and the BM model functionality controlled by the Kalman gain after subtracting the Snake from it. Thus in a fused contour the BM model will have limited effect.

e. Averaging Framework Experimental Results

Due to the un-acceptable results of EKF framework, an averaging approach is used to tackle the difficulties and challenges of the noisy echocardiographic images. In Figure (6.17), samples of results of the framework in the active phase while the LV is contracting are presented. In this figure, the Snake passes the real boundaries of the LV due to the signal drop out. The BM contracts more than the real LV. From the earlier results we see that the estimated contour does not match the real contour of the LV. It is known that tissue mechanics can be quite complex and many assumptions must be made

when deriving a constitutive equation. It is not possible to derive a particular constitutive equation that would accurately model all aspects of tissue behavior under any type of loading. Therefore, during the development of a constitutive equation to model a tissue, there is a trade-off between accurately modeling the tissue behavior and the need to have a constitutive equation that is simple enough to be in a numerical model and to experimentally measure all the constants in the constitutive equation. This gives us the interpretation as to why the biomechanical model does not follow accurately the LV deformation. In Figure (6.18), four samples are given for the passive phase during the relaxation of the LV.

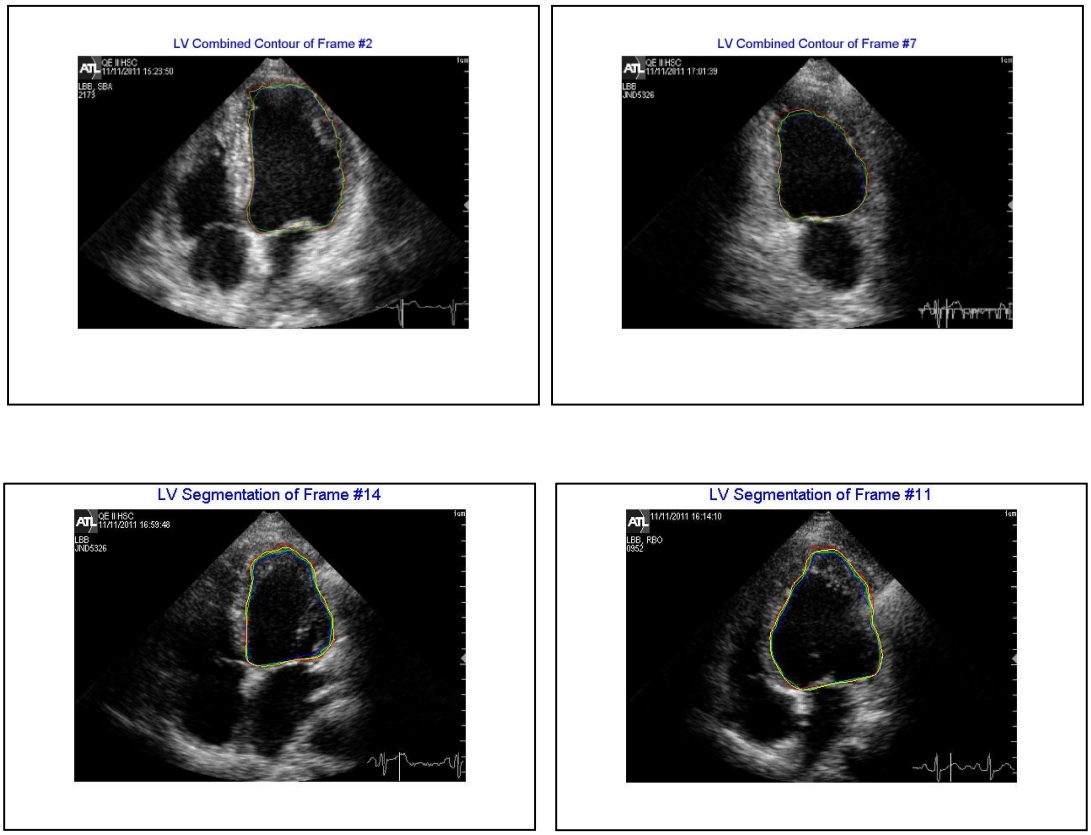

Figure (6.17) – Four samples for the extraction of the LV contour during the active phase

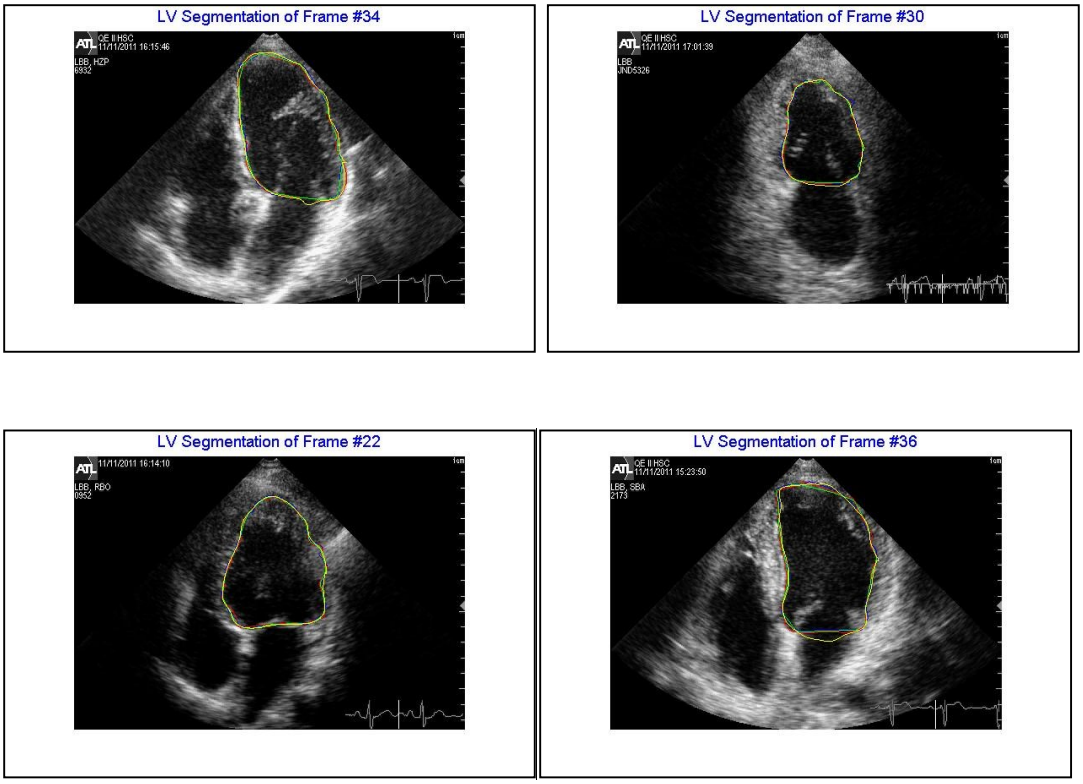

Figure (6.18) – Four samples for the extraction of the LV contour during passive phase

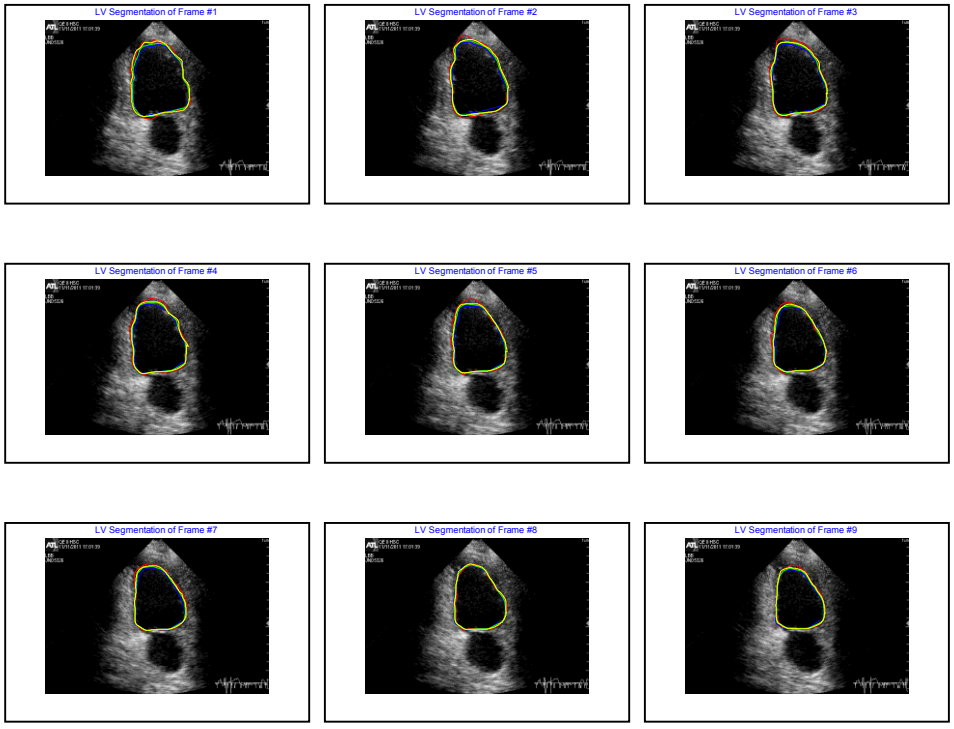

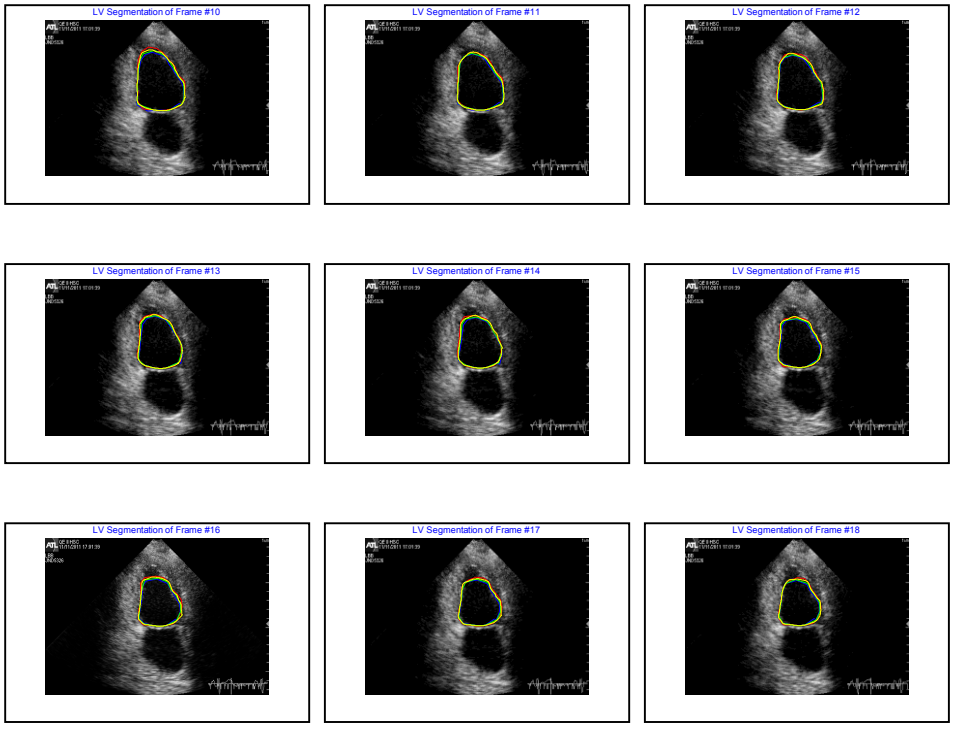

Figure (6.19) – Contour tracking of 18 frames of two chamber view starting from the end of diastole to the end of systole

In Figure (6.20), a sample of tracking the LV in two chamber view case is shown. In this sample, the LV is tracked from the end of diastole when the LV is fall of blood until the end of systole after the completion of pumping blood to whole the body. This period of time is the most important part of the cardiac cycle because it shows the ability of the LV to contract to push the blood to the body. Moreover, tracking LV boundaries in this period enables the cardiologist to extract and obtain all the measured patient data like the regional wall thickness and ejection fraction.

The tracking shows the ability of the framework to detect the LV boundaries in this important period of the cardiac cycle. In all the tracked images, the fused and the final contour are too close to the real LV boundaries. This shows the robustness of integrating the BM model in the tracking framework.

In Figure (6.21), the segmentation and the extraction of the LV area is shown and presented.

The extraction and segmentation removes other parts from the image and shows only the required part that the cardiologists focus to monitor and observe.

As mentioned earlier, tracking the LV in this period provide the cardiologist with a valuable data about the patient. Extracting and segmenting the LV area from the ED to the ES stages enables the cardiologist to view the LV myocardium motion and contraction and the changes in area in each frame by monitoring only the LV area.

In each frame, the LV area is segmented and extracted smoothly by the framework starting from the first frame in the EDS to the last frame in the ESS. Regardless to the image quality, the framework has the ability to extract and segment the LV area in all the 2D echocardiographic image sequence will all the difficulties and challenges that mentioned in the first chapter.

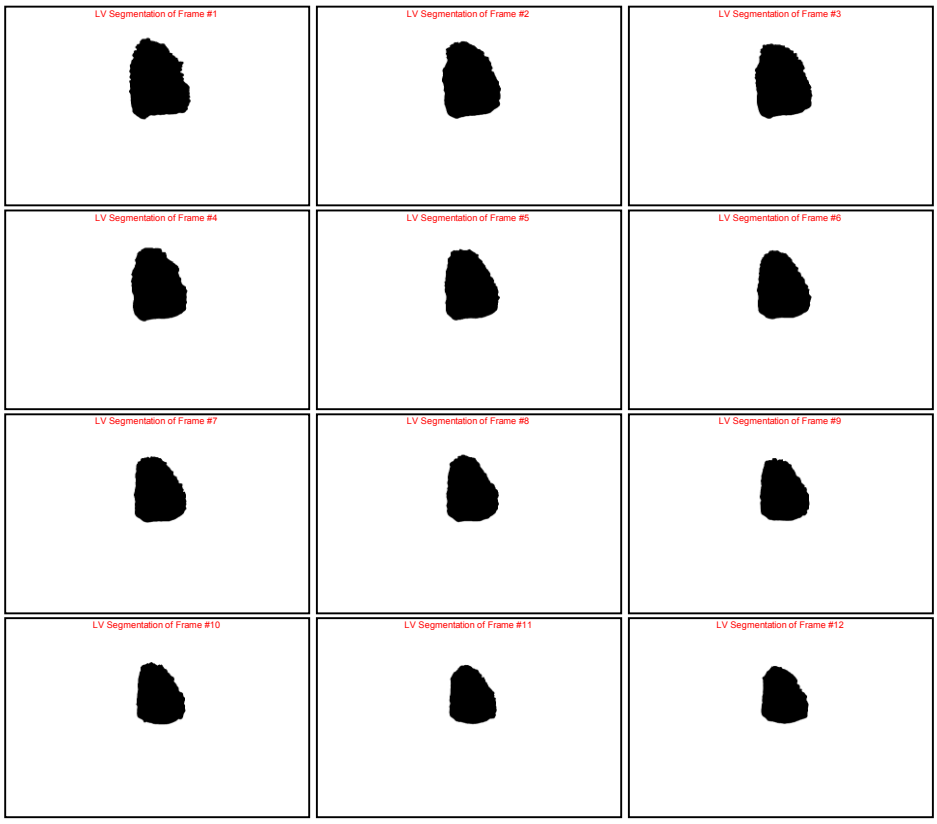

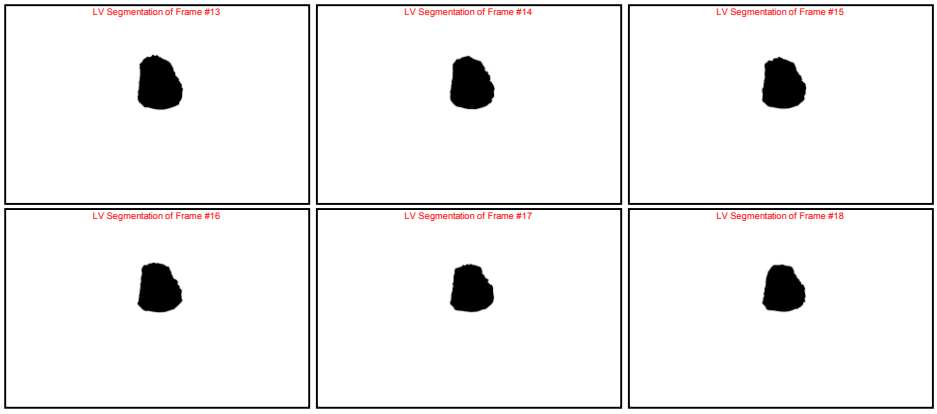

Figure (6.20) – Segmentation of 18 frames of two chamber view starting from the end of diastole to the end of systole

f. Why Averaging Fusion technique?

The averaging fusion technique is used to fuse the Snake and the BM contours due to the following reasons:

In the Active Phase

- The Snake curve moves in the normal direction of the LV domain and usually it passes the real contour of the LV, especially at the parts where the echo image has a drop out in its signal or there are missing parts of the LV.
- At the apex, the image has artifacts and the Snake will stay at the apex area during the LV contraction due to the higher image energy. It will stay there until the end of systole phase.
- The LV rotates suddenly at certain frames of the echo image sequence. The dynamic model will predict the position of the next frame and the Snake will start from this prediction, which is far away from the real contour due to the rotation. Snake will move at the normal direction, leaving the real contour in the opposite direction behind it.

Unlike the Snake, the BM works independently from the image and it has consistent behavior, regardless of the image quality or condition. The contraction of the BM contour

is greater than the real LV. The reason is, the constitutive equations will not simulate the behavior of the myocardium. This shortcoming can be converted to advantage by taking the average value at each control point in the Snake and BM contours. The real contour will be closer to the fused contour than both contours of the BM and the Snake. By deducting the wrong values from its contour points we ensure that the Snake will not pass or stick at any point in the echo image by pulling it down. During the next frame, we also ensure that Snake starts from a position whereby it has the ability to detect the real contour because deformable models exhibit the best performance if they are initialized from a position close the objective contour. As shown in Figures (6.17), (6.18) and (6.19), the Snake passes the real boundaries of the LV due to low intensity values of the pixels. The Snake will treat these pixels as noise and they will be removed from the image. On the other hand, the BM model contour will be less than the Snake contour, especially at the apex where the ultrasound image has maximum drop out and artifacts. By taking the average contour, the resulting contour will be closer to the real boundaries. The level set deformable model will refine the average contour and the final contour will be the accurate one, as shown in the images.

In the Passive Phase:

During the passive phase, the BM resembles the movement of the real LV, as mentioned before and as shown in the images given in Figures (6.17), (6.18) and (6.19). In this phase, the Snake and the BM are very close to each other and the fused contour will obviously be approximately the same in most frames. In the other frames, as shown in the previous figures , both the Snake and the BM cannot follow the LV contour, thus the level set will detect the contour starting from the fusion point as the best approximation.

6.6 RESULTS EVALUATION

In this section, the assessment and the evaluation of the results will be carried out in order to ascertain the accuracy of the obtained results. First, the detected contours will be evaluated using the APD. Then, the computed area enclosed by the LV and the computed EF is evaluated using Bland Altman plot.

a. Evaluating the Computed Contours, Area and EF

- **Computing the APD for the sample No.1**

Table (6.1) – Computing the APD for the sample No. 1

Method	APD (mm)
BM Model	1.887
Snake	0.648
AVG	0.990
Level set	0.636

- **Computing LV enclosed area for the sample No. 1**

Table (6.2) – Computing the LV enclosed area for the sample No. 1

Method	AREA (cm^2)
BM Model	9.285
Snake	11.093
AVG	10.139
Level set	10.784
Gold Standard	11.0358

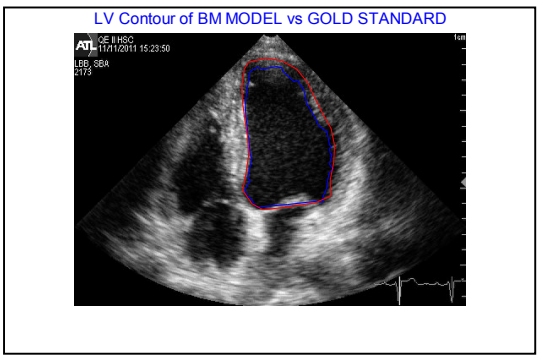

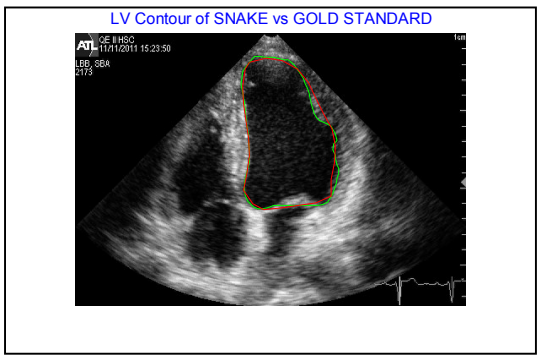

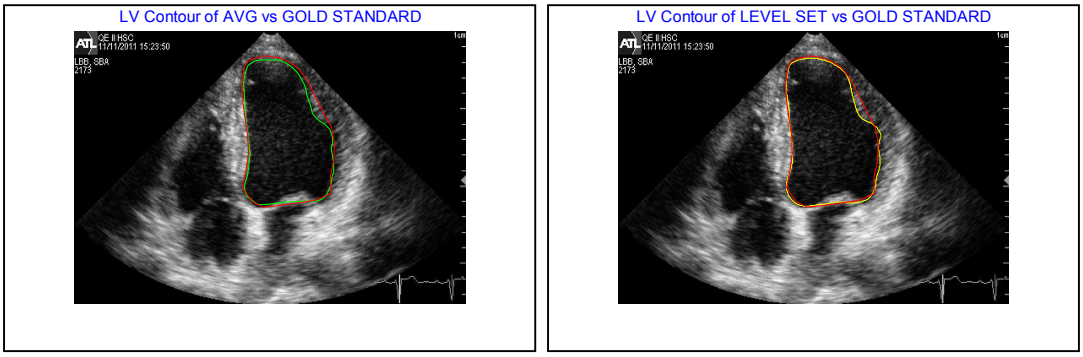

Figure (6.21) – Plotting the BM, Snake, AVG and Level set contours vs. their gold standard for the sample No.1

- **Computing the APD for the sample No.2**

Table (6.3) – Computing the APD for sample No. 2

Method	APD (mm)
BM Model	1.849
Snake	1.598
AVG	1.490
Level set	1.555

- **Computing LV enclosed area for the sample No. 2**

Table (6.4) – Computing LV enclosed area for the sample No. 2

Method	AREA (cm^2)
BM Model	5.813
Snake	6.645
AVG	6.216
Level set	6.670
Gold Standard	7.748

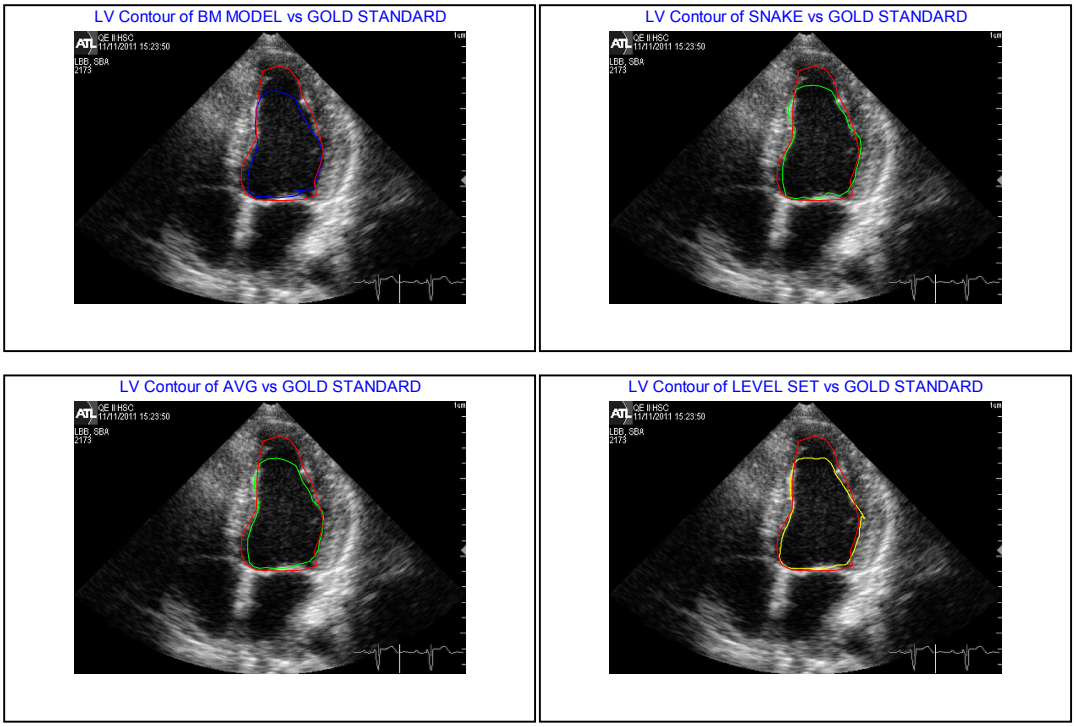

Figure (6.22) – Plotting the BM, Snake, AVG and Level set contours vs. their gold standard for the sample No. 2

- **Computing the EF for the first case**

Table (6.5) – Computing the EF for the case No. 1

Method	EF
BM Model	0.373
Snake	0.4
AVG	0.386
Level set	0.381
Gold Standard	0.297

- **Computing the APD for the sample No. 3**

Table (6.6) – Computing the APD for the sample No. 3

Method	APD (mm)
BM Model	1.541
Snake	1.607
AVG	1.854
Level set	1.167

- **Computing LV enclosed area for the sample No. 3**

Table (6.7) – Computing LV enclosed area for the sample No. 3

Method	AREA (cm^2)
BM Model	7.982
Snake	9.233
AVG	8.574
Level set	9.149
Gold Standard	9.896

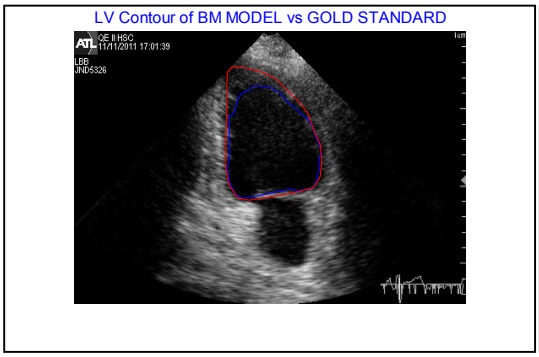

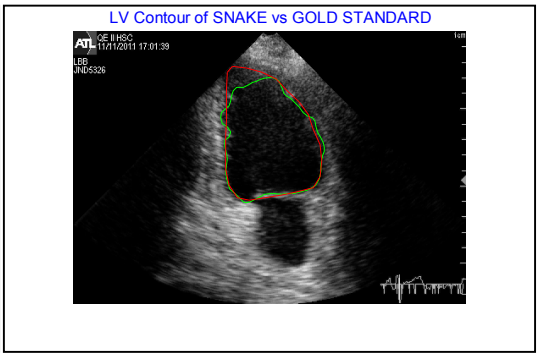

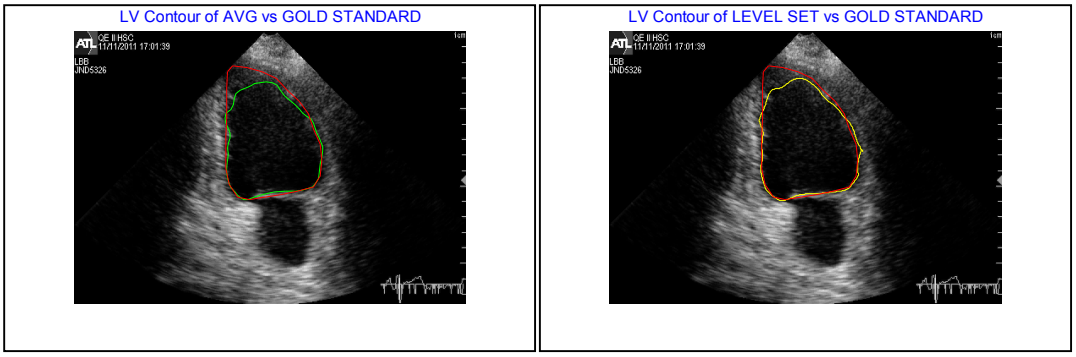

Figure (6.23) – Plotting the BM, Snake, AVG and Level set contours vs. their gold standard for the sample No. 3

- **Computing APD for the sample No. 4**

Table (6.8) – Computing the APD for sample No. 4

Method	APD (mm)
BM Model	1.502
Snake	1.591
AVG	1.487
Level set	1.515

- **Computing LV enclosed Area for the sample No. 4**

Table (6.9) – Computing LV enclosed area the sample No. 4

Method	AREA (cm^2)
BM Model	5.0
Snake	5.573
AVG	5.283
Level set	5.755
Gold Standard	5.505

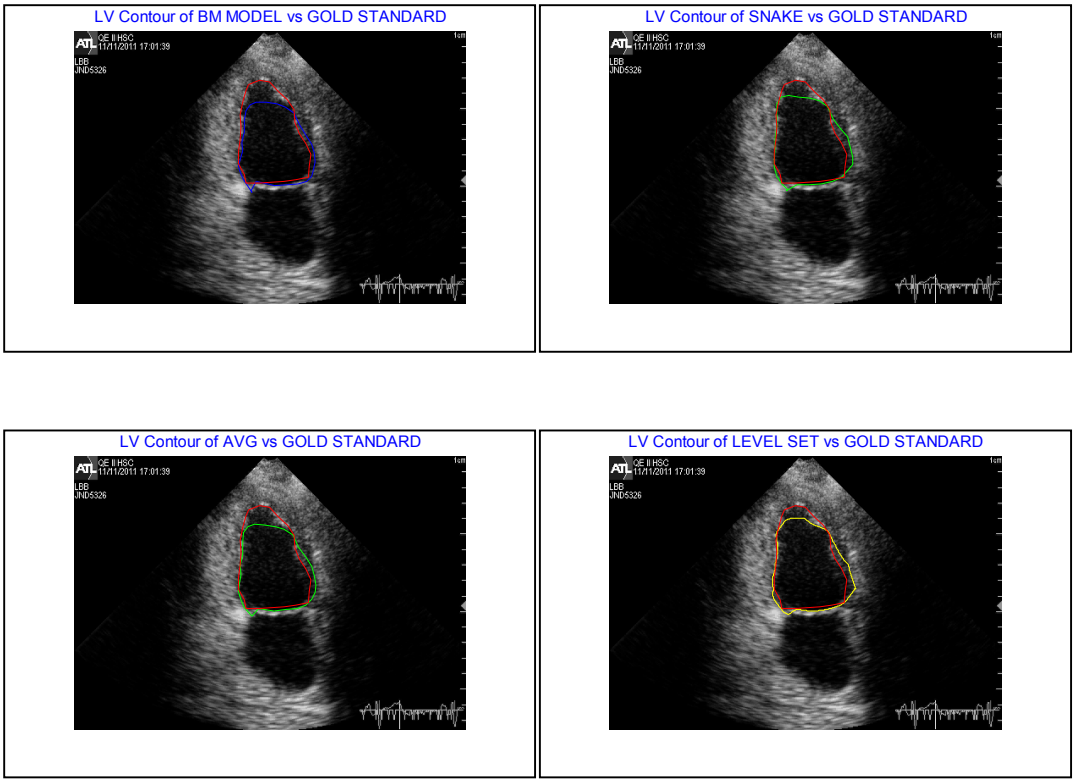

Figure (6.24) – Plotting the BM, Snake, AVG and Level set contours vs. their gold standard for the sample No. 4

- **Computing the ejection fraction for case No. 2**

Table (6.10) – Computing the EF for case No. 2

Method	EF
BM Model	0.373
Snake	0.396
AVG	0.391
Level set	0.371
Gold Standard	0.443

- **Computing APD for sample No. 5**

Table (6.11) – Computing the APD for sample No. 5

Method	APD (mm)
BM Model	1.557
Snake	0.954
AVG	1.039
Level set	1.0

- **Computing LV enclosed Area for sample No.5**

Table (6.12) – Computing LV enclosed area for sample No. 5

Method	AREA (cm^2)
BM Model	9.541
Snake	10.704
AVG	10.239
Level set	10.908
Gold Standard	10.583

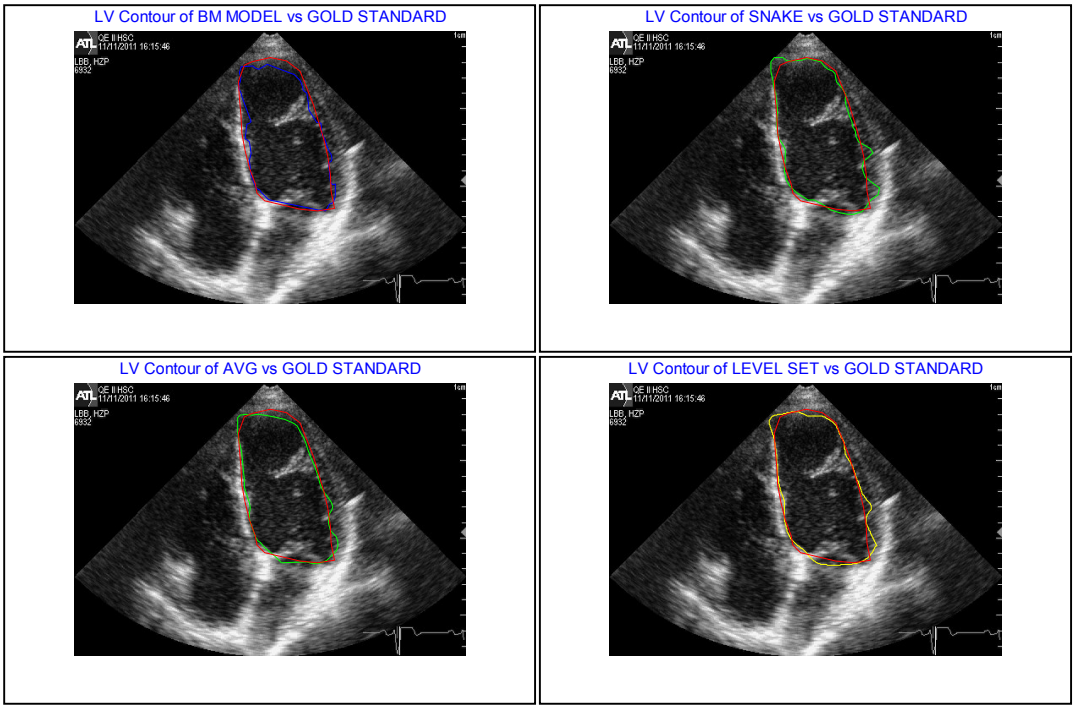

Figure (6.25) – Plotting the BM, Snake, AVG and level set contours vs. their gold standard for sample No. 5

- **Computing the APD for sample No. 6**

Table (6.13) – Computing the APD for sample No. 6

Method	APD (mm)
BM Model	1.451
Snake	1.688
AVG	1.887
Level set	1.954

- **Computing LV enclosed area for sample No. 6**

Table (6.14) – Computing LV enclosed area for sample No.6

Method	AREA (cm^2)
BM Model	5.927
Snake	6.482
AVG	6.234
Level set	7.142
Gold Standard	8.606

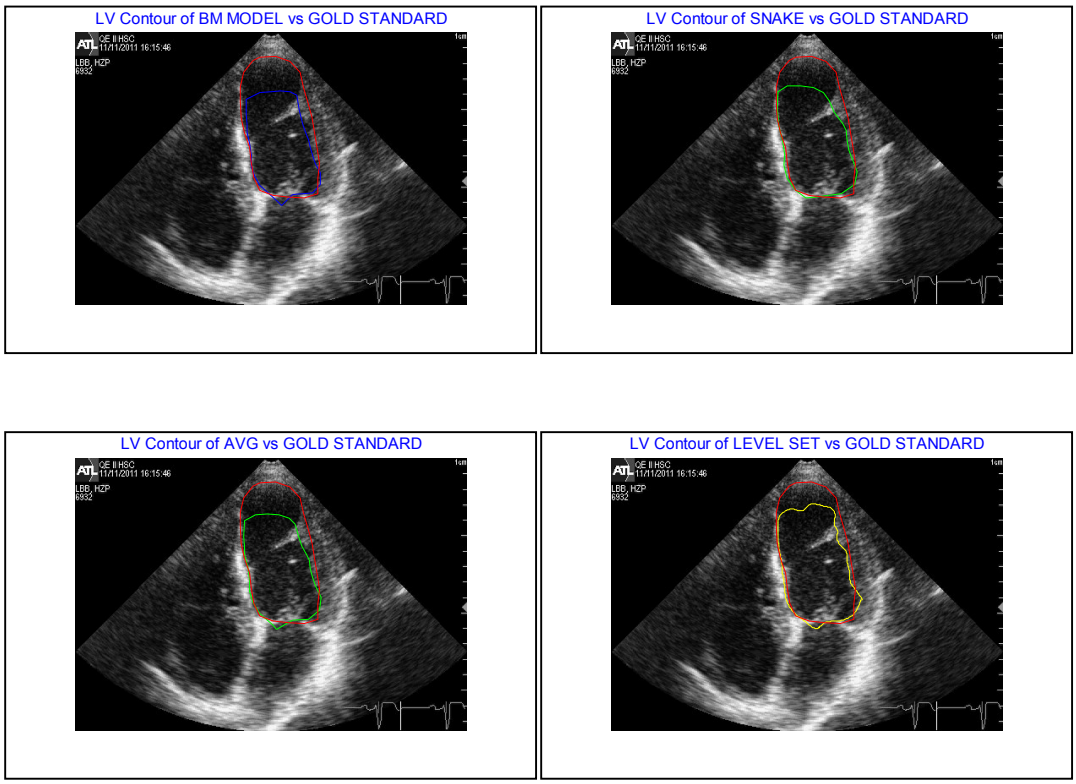

Figure (6.26) – Plotting the BM, Snake, AVG and Level set contours vs. their gold standard for sample No.6

- **Computing the ejection fraction for case No. 3**

Table (6.15) – Computing the EF for case No. 3

Method	EF
BM Model	0.378
Snake	0.394
AVG	0.391
Level set	0.345
Gold Standard	0.186

- **Computing APD for sample No. 7**

Table (6.16) – Computing the APD for sample No. 7

Method	APD (mm)
BM Model	1.556
Snake	1.544
AVG	1.704
Level set	1.40

- **Computing LV enclosed Area for sample No. 7**

Table (6.17) – Computing LV enclosed area for sample No. 7

Method	AREA (cm^2)
BM Model	9.594
Snake	10.829
AVG	10.341
Level set	11.129
Gold Standard	11.1354

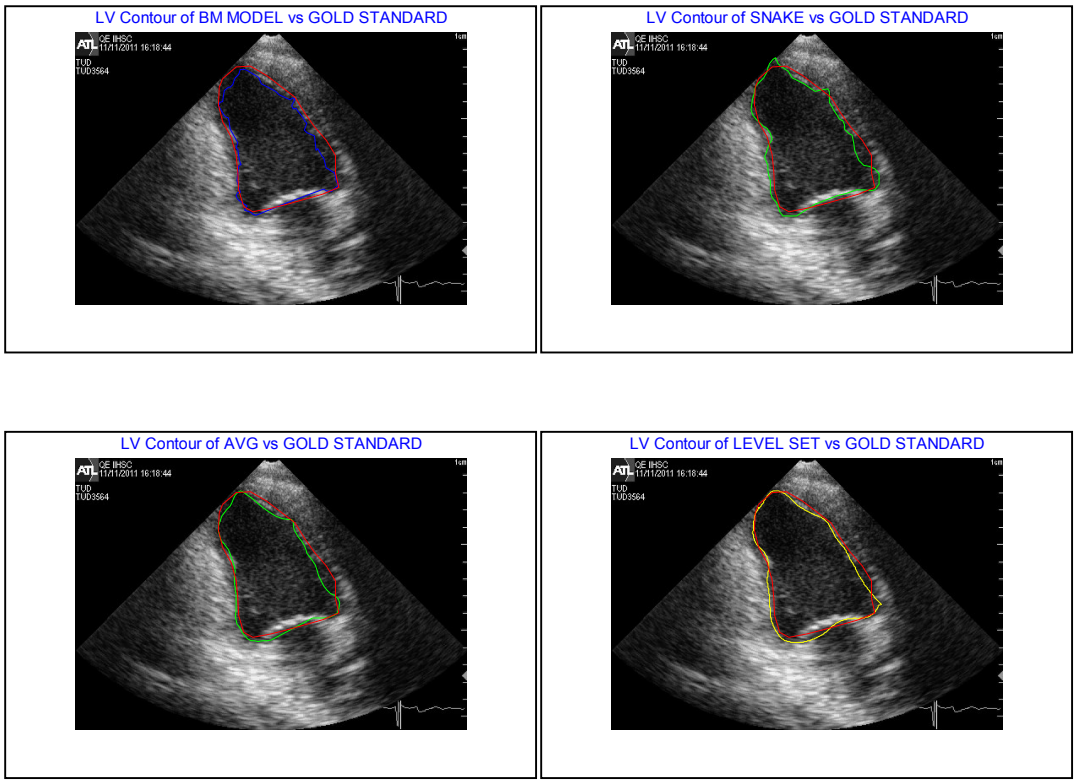

Figure (6.27) – Plotting the BM, Snake, AVG and Level set contours vs. their gold standard for sample No. 7

- **Computing APD for the sample No. 8**

Table (6.18) – Computing the APD for sample No. 8

Method	APD (mm)
BM Model	1.329
Snake	1.606
AVG	1.590
Level set	1.524

- **Computing LV enclosed area for sample No. 8**

Table (6.19) – Computing LV enclosed area for sample No. 8

Method	AREA (cm^2)
BM Model	5.780
Snake	6.270
AVG	6.007
Level set	6.360
Gold Standard	5.948

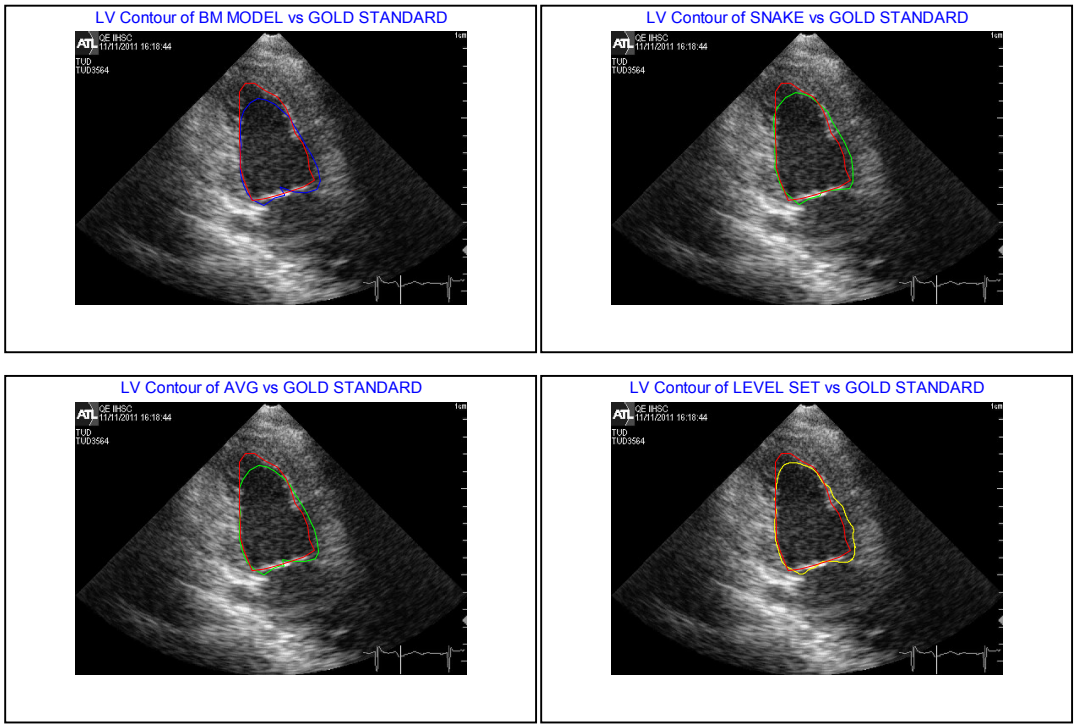

Figure (6.28) – Plotting the BM, Snake, AVG and Level set contours vs. their gold standard for sample No. 8

- **Computing the ejection fraction for case No. 4**

Table (6.20) – Computing EF for case No. 4

Method	EF
BM Model	0.397
Snake	0.420
AVG	0.419
Level set	0.428
Gold Standard	0.465

- **Computing APD for sample No.9**

Table (6.21) – Computing the APD for sample No. 9

Method	APD (mm)
BM Model	1.534
Snake	1.187
AVG	1.379
Level set	1.057

- **Computing LV enclosed area for sample No. 9**

Table (6.22) – Computing LV enclosed area for sample No. 9

Method	AREA (cm^2)
BM Model	8.830
Snake	9.919
AVG	9.438
Level set	10.114
Gold Standard	10.124

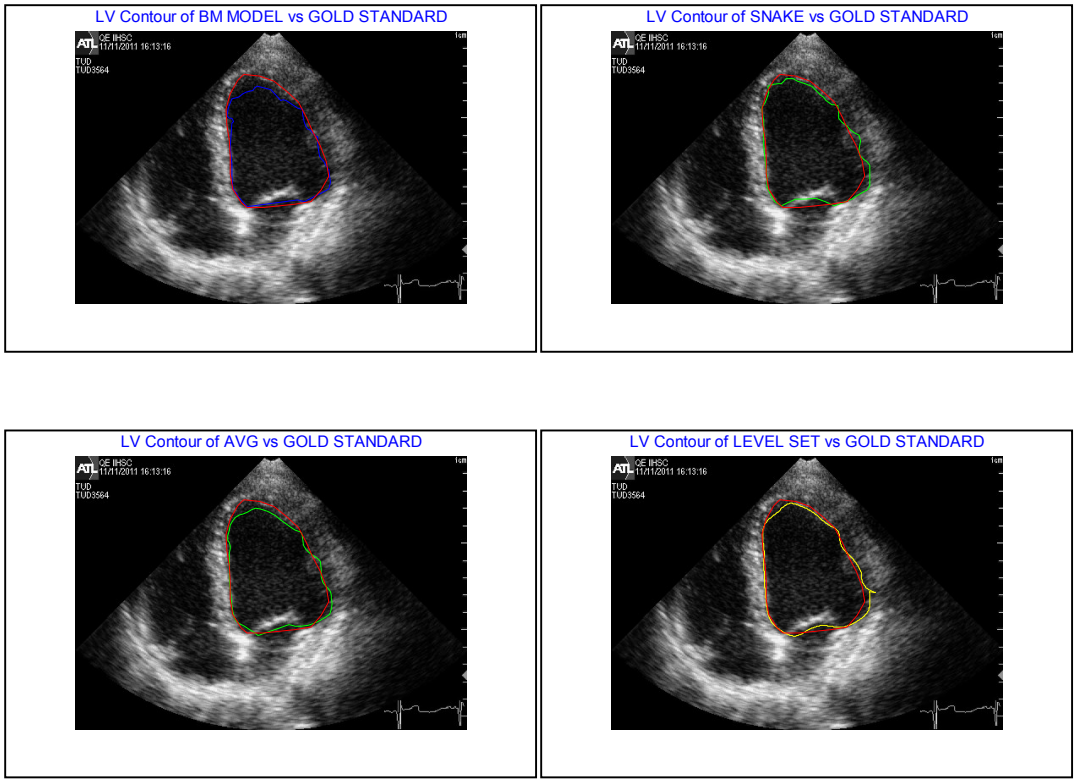

Figure (6.29) – Plotting the BM, Snake, AVG and Level set contours vs. their gold standard for sample No. 9

- **Computing APD for sample No. 10**

Table (6.23) – Computing the APD for sample No.10

Method	APD (mm)
BM Model	1.454
Snake	0.964
AVG	1.321
Level set	0.834

- **Computing LV enclosed area for sample No. 10**

Table (6.24) – Computing LV enclosed area for sample No. 10

Method	AREA (cm^2)
BM Model	5.310
Snake	6.254
AVG	5.767
Level set	6.315
Gold Standard	6.465

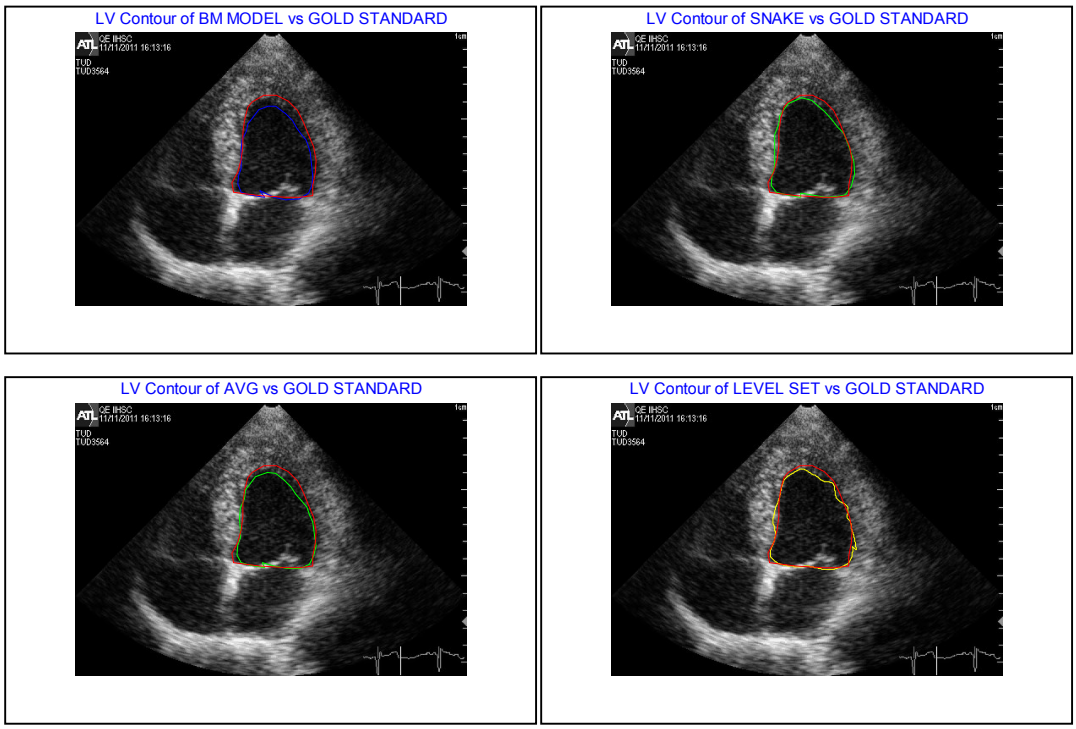

Figure (6.30) – Plotting the BM, Snake, AVG and level set contours vs. their gold standard for sample No. 10

- **Computing the ejection fraction for case No.5**

Table (6.25) – Computing the EF for case No. 5

Method	EF
BM Model	0.398
Snake	0.369
AVG	0.388
Level set	0.375
Gold Standard	0.361

b. Statistical Analysis

In order to provide a concise summary of the results, a statistical analysis is created depending on the following parameters: mean, standard deviation, standard error, and 95% confidence interval, to evaluate the computed results compared to the gold standard

- **Computing the mean of the Measured APD**

Table (6.26) – Computing the mean of the measured APDs

Method	Mean (mm)
BM Model	1.566
Snake	1.313
AVG	1.515
Level set	1.277

- **Computing the Standard Deviation**

Table (6.27) – Computing the standard deviation of the measured APDs

Method	Standard deviation (*s)*
BM Model	0.173
Snake	0.358
AVG	0.333
Level set	0.407

- **Computing the Standard Error**

The standard error is a good estimate of the standard deviation of the given distribution.

The standard error is calculated using the following formula:

$$StErr = \frac{s}{\sqrt{n}} \tag{6.2}$$

Where s is the standard deviation and n is the number of samples.

Table (6.28) – Computing the standard error of the measured APDs

Method	Standard error
BM Model	0.054
Snake	0.113
AVG	0.105
Level set	0.128

- **95% Confidence Interval**

The standard error can be used to calculate confidence intervals for the true population mean. For a 95% 2-sided confidence interval, the Upper Confidence Limit (UCL) and Lower Confidence Limit (LCL) are calculated as follows (units in mm as noted in the tables):

$$95\%UCL = mean + 2.228 \times StErr = mean + 2.228\frac{s}{\sqrt{n}}$$

$$95\%LCL = mean - 2.228 \times StErr = mean - 2.228\frac{s}{\sqrt{n}} \tag{6.3}$$

Table (6.29) – Computing the 2-sided confidence interval

Method	LCL (mm)	UCL (mm)
BM Model	1.446	1.686
Snake	1.061	1.564
AVG	1.281	1.749
Level set	0.992	1.562

c. Bland and Altman Statistical Analysis

The Bland-Altman plot is a method that measures the degree of agreement between two different measuring techniques to find out if they are in sufficient agreement to allow the old technique to be replaced by the new one [145]. The Bland-Altman plot is done by plotting the difference of the two techniques in the *Y* axis and the mean of them in the X axis, as in the following formula, if *data1* and *data2* are the measurements of the two techniques:

$$data(x, y) = \left(\frac{data1 + data2}{2}, data1 - data2 \right) \tag{6.4}$$

Two red lines are shown in the graph, the above red line represents (mean+2× standard deviation) and the lower red line represents (mean-2× standard deviation). The black line represents the mean difference. The difference between the two techniques will be accepted if they are located between the red lines.

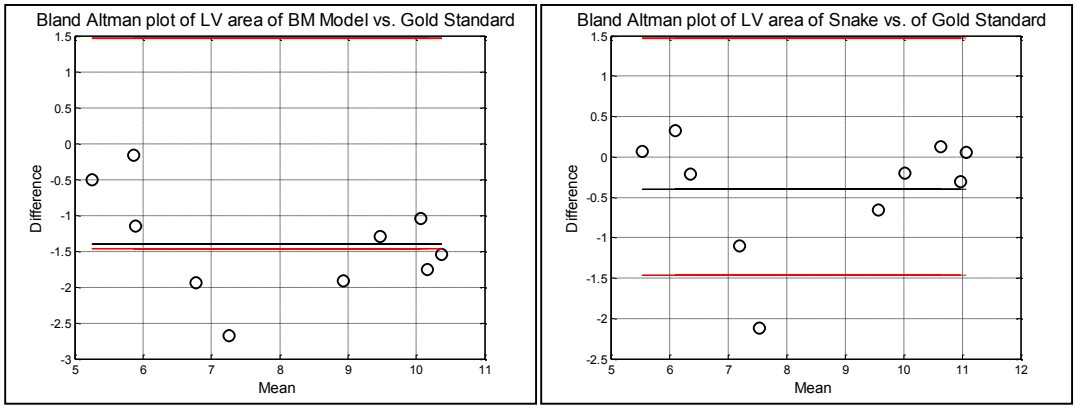

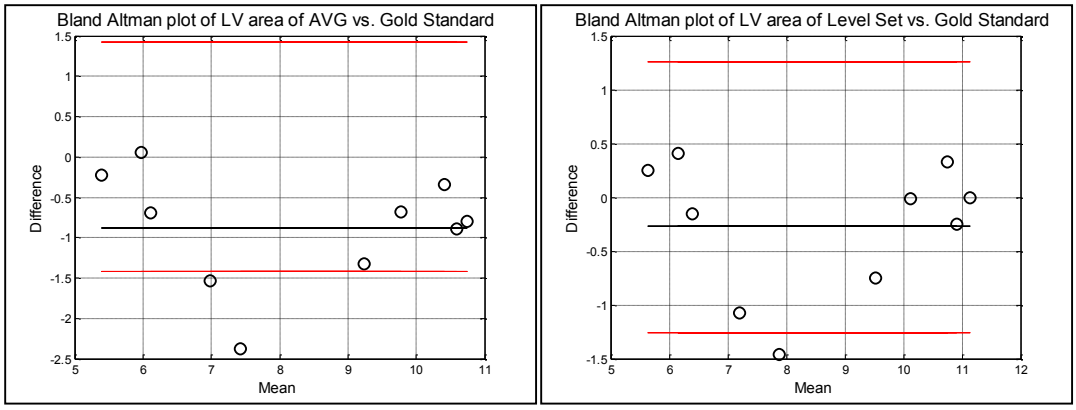

Figure (6.31) – Bland Altman plot for LV area computed vs. gold standard

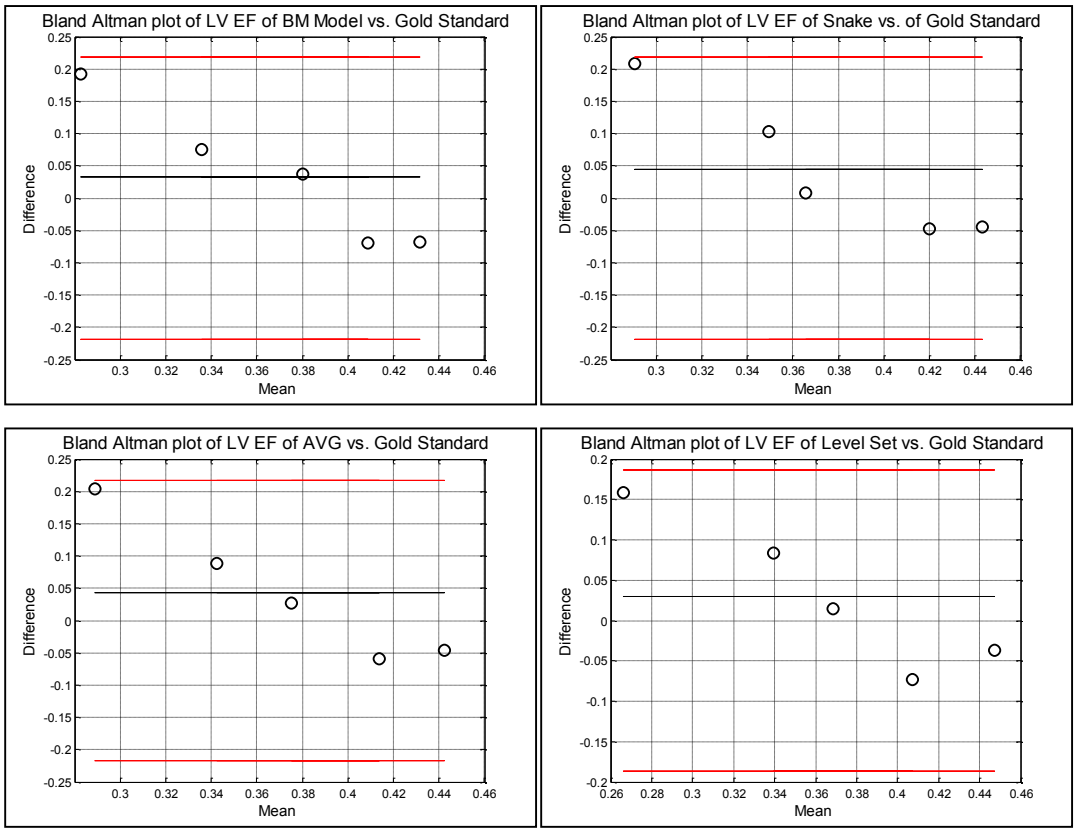

Figure (6.32) – Bland Altman plot for LV computed EF vs. gold standard

6.7 DISCUSSION AND RESULTS ANALYSIS

By incorporating the BM model in the averaging fusion technique framework, the framework can achieve the following features:

- Robustness and stability over all the samples during the cardiac cycle.
- The closeness of the results to the gold standard.
- Keeping the deformable models inside the ROI (Region of Interest) by overcoming the difficulties of twisting and rotation of the LV.
- Preventing the deformable models from leaking outside the ROI when there are missing parts of LV boundaries or signal drop out.
- The BM model plays a dominant rule in the framework by providing the concrete base that the framework stands on during the cardiac cycle. The BM model works independently from the ultrasound images and can provide accurate detection to the LV boundaries where the deformable models fail to do so.
- By employing averaging fusion techniques, we always ensure that the fused contour is close to the boundaries of the LV by removing the outliers in the deformable models and by modifying the BM model contour.
- The fused contour and the dynamic model provide robustness and an accurate starting point by initializing the current frame with a close contour to the desired one. This accurate initialization ensures the quality of the contour detection and reduces the required running time for the deformable models by reducing the number of iterations that the deformable models require.
- The contours become closer to each other as the cardiac cycle approaches the end of systole. This indicates that the framework has performed well enough to keep all the contours inside the ROI. As we approach the end of systole, the LV contracts and the size of the heart becomes smaller. The concentration of the pixels around the LV increases with approximately the same intensity value and there are no missing parts in the boundary. In this situation, the deformable models will not leak out from the ROI and the BM model will have close performance to the deformable models, due to the reduction in the applied pressure as we approach the end of systole phase.

- When the Snake control points are redistributed by removing the closed control points and inserting a new control point in the position where the control points are very far from each other; the performance of the Snake becomes more robust. This is because the entire LV contour is covered, satisfying the snake algorithm's condition of equidistance.
- Within this framework and the feature mentioned above, the Snake exhibits significant improvement and great performance over the cardiac cycle and we can achieve very accurate results.
- The constitutive equations of the BM model resemble and simulate the intact heart. From the results above, the BM model and the overall framework accurately detect the contour, area and ejection fraction for cases in which the heart is normal or suffers from fewer complications and abnormality. In cases where the patient has a severe heart abnormality (like in cases 1 and 3), the heart of patient does not contract as normal (dysfunction case) and the stroke volume is also less than normal. In this situation, the BM contour will not be an exact match for the real contour, which will affect the overall contour of the frame work.
- From the APD data and the statistical analysis, the last contour (level set) scores the highest accurate results and is the closet contour to the gold standard. If we look at the mean of the four contours, which tells us about the central tendency of the data, the level set contour has the lowest value, which means the high accuracy with less error. The BM model has the most consistent performance, which scores the lowest standard deviation also with less value for the standard error.
- The level set contour has outstanding results in computing the area and ejection fraction values. In calculating the area, 90% of the computed area is located in the acceptance range (between the two red lines), while the tenth sample is too close to the acceptance range.
- For the ejection fraction, 100% of the computed values are located in acceptance range.
- The acceptance range for the level set is too narrow compared to other methods. It is located between ± 1.256 mean differences for the area and ±0.186 for the EF.

- The area computed by the BM enclosed contour is affected by the end systole phases, where the BM model has less area than the sample case when the patient has a severe abnormality. In the area plot in Figure (6.32), these computed areas are located outside the acceptance range. This computation can be compensated when estimating the EF by using its formula where the end of systole phase dominates the computation as illustrated in Figure (6.33).

6.8 SUMMARY

In this Chapter, the difficulties facing the evaluation of segmentation and tracking in medical images are presented. The method and steps of creating the gold standard from three manually tracing of cardiologists are presented. APD as an error metric is presented. Experimental results for the BM model and the deformable models are given. The evaluation of the computed contours, enclosed area and the ejection fraction is made comparing to the created gold standard. The discussion and analysis of the results are given.

CHAPTER 7 CONCLUSION AND FUTURE WORK

7.1 CONCLUSION

Unlike the previous work done in tracking the LV through the cardiac cycle of the 2D echocardiographic image sequence, instead of depending on imaging based techniques alone, in this thesis the LV mechanical properties are utilized through the BM model. FEM is utilized to obtain the LV contour and exact pressure and time is provided at each frame of the cardiac cycle to obtain the precise LV boundaries. The objective is to achieve significant improvement in detecting and tracking the boundaries and segmenting the LV area for the complete cardiac cycle.

In this thesis, the implemented framework is based on the fusion of the BM model and the Snake followed by the level set method.

In the BM model, to mimic the LV function and motion, two different strain energy functions are used to simulate the LV deformations in the active and passive phases.

FBEM is used to solve the constitutive equations of the BM model using an incremental iterative procedure. The results are not acceptable due to the lack incorporation of the load (pressure) and time in the solution.

FEM is used in this thesis instead of FBEM to get the deformations of the LV in each frame in a timely fashion as the real LV is deformed during the cardiac cycle.

The pressure (load) is simulated in each frame through the cardiac cycle to let the LV deform in both the active and passive phases.

The ABAQUS FEA is used and linked with MATLAB through the PYTHON language program to transfer the LV deformations estimated by ABAQUS to MATLAB's main program.

The parametric deformable model (Snake) is used and the detected contour is fused with the BM model contour by two different techniques. First, the EKF is used however the results are not acceptable due to the many shortcomings of this fusion technique. The averaging fusion technique is used as an alternative solution to the EKF, followed by the non-parametric deformable model (level set method). The averaging framework can detect the contour of the LV with acceptable accuracy.

To evaluate the results and tackle the problem of the lack of gold standard, a gold standard is created in this thesis from three different manual outlines from three different cardiologists. APD is used as an error metric to evaluate the computed contour and the Bland and Altman plot is used to evaluate the computed area and EF. Successful segmentation was achieved in all cases, with limits of agreement for average perpendicular distance of 1.277 ±0.267 mm compared to the created gold standard.

From the evaluation and statistical analysis, the data shows highly accurate results for normal and abnormal heart patients. Less accurate results are obtained for patients with severe abnormality complications, but still the results fall within the acceptance range.

7.2 Future Work

The analysis of the difficulties in tracking and segmenting the 2D echocardiographic image sequence and the challenges due to the heart movement and the proposed solution methods presented in this thesis can be further extended and enhanced. The following subjects may shed some light on the intended work extensions:

- According to the promising results with the 2D echocardiographic images, the framework and the solution scheme can be further extended to 3D echocardiographic images.
- Instead of a 2D solution, a 3D BM model will be used for tracking the volume of the LV.
- An alternative deformable model will be incorporated instead of the Snake and level set method to extract and correct the LV contour.
- The gold standard also needs to be updated from 2D to 3D to evaluate the results of 3D solution scheme.

REFERENCES

[1] H. Ketout, J. Gu and G. Horne, "MVN_CNN and FCNN For Endocardial Edge Detection," *1st Middle East Conference on Biomedical Engineering (MECBME),* 2011, pp. 208-212.

[2] V. Chalana, D. Linker, D. Haynor and Y. Kim, "A Multiple Active Contour Model For Cardiac Boundary Detection On Echocardiographic Sequences," *IEEE Transactions on Medical Imaging*, vol. 15, no. 3, 1996, pp. 290-298.

[3] J. Bosch, S. Mitchell, B. Lelieveldt, F. Nijland, O. Kamp, M. Sonka and J. Reiber, "Automatic Segmentation Of Echocardiographic Sequences By Active Appearance Motion Models," *IEEE Transactions on Medical Imaging*, vol. 21, no. 11, 2002, pp. 1374-1383.

[4] C. Chu, E. Delp and A. Buda, "Detecting Left Ventricular Endocardial And Epicardial Boundaries By Digital Two-Dimensional Echocardiography," *IEEE Transactions on Medical Imaging*, vol. 7, no. 2, 1988, pp. 81-90.

[5] U. Bharali and D. Ghosh, "Cardiac Motion Estimation From Echocardiographic Image Sequence Using Unsupervised Active Contour Tracker," *ICARCV '06. 9th International Conference on Control, Automation, Robotics and Vision,* 2006, pp. 1-6.

[6] C. Corsi, C. Lamberti, S. Cerutti, J. Laulom, O. Bailliart, B. Cholley, A. Capderou, P. Vaida and E. Caiani, "Quantification Of Left Ventricular Modification In Weightlessness Conditions From The Spatio-temporal Analysis Of 2D Echocardiographic Images," *Medical and Biological Engineering and Computing*, vol. 42, no. 5, 2004, pp. 610-617.

[7] H. Ketout, J. Gu and G. Horne, "Improved Dempster And Shafer Theory To Fuse Fuzzy Inference System, Neural Networks And CNN Endocardial Edge Detection," *The Mediterranean Journal of Electronics and Communications*, vol. 7, no. 3, 2011, pp. 267-275.

[8] G. Sainarayanan, N. Murugan and S. Chan, "A Novel Method for Echocardiogram Boundary Detection Using Adaptive Neuro -Fuzzy Systems," *International Conference on Computational Intelligence and Multimedia Applications,* 2007, vol. 3, pp. 415-419.

[9] H. Ketout, J. Gu and G. Horne, "MVN_CNN and UBN_CNN for endocardial edge detection," *Natural Computation (ICNC), 17th International Conference on*, vol. 2, 2011,pp. 781-785.

[10] L. Zhang and E. Geiser, "An Effective Algorithm for Extracting Serial Endocardial Borders from 2-Dimensional Echocardiograms," *IEEE Transactions on Biomedical Engineering*, vol. BME-31, no. 6, 1984, pp. 441-447.

[11] P. Bansod, U. Desai and N. Burkule, "Multi Frame Guided Local Search For Semiautomatic Endocardial Contour Estimation In Echocardiography Sequences," *6th International Conference on Information, Communications & Signal Processing, 2007*, pp. 1-5.

[12] J. Noble and D. Boukerroui, "Ultrasound Image Segmentation: A Survey," *IEEE Transactions on Medical Imaging*, vol. 25, no. 8, 2006, pp. 987-1010.

[13] Y. Fung, "Biomechanics: Mechanical Properties of Living Tissues,", Springer, 1st Edition, 1981.

[14] D. Lin and F. Yin, "A Multiaxial Constitutive Law For Mammalian Left Ventricular Myocardium In Steady-State Barium Contracture Or Tetanus," *J.Biomech.Eng.*, vol. 120, no. 4, 1998, pp. 504-517.

[15] M. Sacks and W. Sun, "Multiaxial Mechanical Behavior Of Biological Materials," *Annu.Rev.Biomed.Eng.*, vol. 5, no. 1, 2013, pp. 251-284.

[16] H. Ketout, J. Gu and G. Horne, "Improved Dempster and Shafer Theory To Fuse Region And Edge Based Level Set For Endocardial Contour Detection," *10th World Congress on Intelligent Control and Automation (WCICA),* 2012, pp. 5013-5018.

[17] J. Kittler, M. Hatef, R. Duin and J. Matas, "On Combining Classifiers," *IEEE Transactions on Pattern Analysis and Machine Intelligence*, vol. 20, no. 3, 1998, pp. 226-239.

[18] N. Senthilkumaran and R. Rajesh, "Edge Detection Techniques For Image Segmentation – A Survey Of Soft Computing Approaches," *International Journal of Recent Trends in Engineering*, vol. 1, no. 2, 2009 Academy Publisher, pp. 250-254.

[19] R. Maini and H. Aggarwal, "Study and Comparison Of Various Image Edge Detection Techniques," *International Journal of Image Processing (IJIP)*, vol. 3, no. 1, 2009, pp. 1-12.

[20] G. Narendra and S. Hareesh, "Study And Comparison Of Various Image Edge Detection Techniques Used In Quality Inspection And Evaluation Of Agricultural And Food Products By Computer Vision," *Int J Agric & Biol Eng*, vol. 4, no. 2, 2011, pp. 83-90.

[21] D. Wilson, E. Geiser and J. Li, "Feature Extraction In Two-Dimensional Short-Axis Echocardiographic Images," *Journal of Mathematical Imaging and Vision*, vol. 3, no. 3, 1993, pp. 285-298.

[22] L. Herlin and G. Giraudon, "Performing Segmentation Of Ultrasound Images Using Temporal Information," *IEEE Computer Society Conference on Computer Vision and Pattern Recognition,* 1993, pp. 373-378.

[23] M. Baroni and G. Barletta, "Contour Definition and Tracking in Cardiac Imaging Through the Integration of Knowledge and Image Evidence," *Ann.Biomed.Eng.*, vol. 32, no. 5, 2004, pp. 688-695.

[24] H. Ketout, J. Gu and G. Horne, "Fuzzy Inference System For Endocardial Edge Detection," *Seventh International Conference on Fuzzy Systems and Knowledge Discovery (FSKD), 2010*, vol. 2, pp. 555-559.

[25] H. Ketout, J. Gu and G. Horne, "MVN_CNN and UBN_CNN For Endocardial Edge Detection," *7th International Conference on Natural Computation (ICNC),* vol. 2, *2011,* pp. 781-785.

[26] M. Choy and J. Jin, "Extracting Endocardial Boarders From Sequential Echocardiographic Images," *Engineering in Medicine and Biology Magazine, IEEE*, vol. 7, no. 1, 1998, pp. 116-121.

[27] S. Narang and M. Lal, "Adaptive Image Enhancement of Echocardiographic Images Using Automatic ROI," *International Journal of Application or Innovation in Engineering & Management (IJAIEM)*, vol. 2, July 2013, pp. 148-154.

[28] J. McEachen II and J. Duncan, "Shape-Based Tracking Of Left Ventricular Wall Motion," *IEEE Transactions on Medical Imaging*, vol. 16, no. 3, 1997, pp. 270-283.

[29] J.C. McEachen II, A. Nehorai and J. Duncan, "Estimating Cardiac Motion From Image Sequences Using Recursive Comb Filtering," *International Conference on Image Processing,* 1995, vol. 2, pp. 496-499.

[30] S. Yeo, L. Zhong, Y. Su, R. Tan and D. Ghista, "Analysis Of Left Ventricular Surface Deformation During Isovolumic Contraction," *29th Annual International Conference of the IEEE Engineering in Medicine and Biology Society,* 2007, pp. 787-790.

[31] J. McEachen II and J. Duncan, "A Constrained Analytic Solution For Tracking Non-Rigid Motion Of The Left Ventricle," *Eighteenth IEEE Annual Northeast Bioengineering Conference,* 1992, pp. 137-138.

[32] A. Mishra, P. Dutta and M. Ghosh, "A GA based approach for boundary detection of left ventricle with echocardiographic image sequences," *Image Vision Comput.*, vol. 21, no. 11, 2003, pp. 967.

[33] M. Kass, A. Witkin and D. Terzopoulos, "Snakes: Active Contour Models," *International Journal Of Computer Vision*, vol. 1, no. 4, 1988, pp. 321-331.

[34] S. Malassiotis and M. Strintzis, "Tracking The Left Ventricle In Echocardiographic Images By Learning Heart Dynamics," *IEEE Transactions on Medical Imaging*, vol. 18, no. 3, 1999, pp. 282-290.

[35] C. Sheng, Y. Xin, Y. Liping and S. Kun, "Segmentation In Echocardiographic Sequences Using Shape-Based Snake Model Combined With Generalized Hough Transformation," *The International Journal of Cardiovascular Imaging (formerly Cardiac Imaging)*, vol. 22, no. 1, 2006, pp. 33-45.

[36] J. Cheng, S. Foo and S. Krishnan, "Echocardiographic Image Sequence Segmentation By Multiscale Directional Snake," *Proceedings of the Fourth IEEE International Symposium on Signal Processing and Information Technology,* 2004, pp. 26-29.

[37] I. Mikic, S. Krucinski and J. Thomas, "Segmentation And Tracking In Echocardiographic Sequences: Active Contours Guided By Optical Flow Estimates," *IEEE Transactions on Medical Imaging*, vol. 17, no. 2, 1998, pp. 274-284.

[38] M. Berger, G. Winterfeldt and J. Lethor, "Contour Tracking in Echocardiographic Sequences Without Learning Stage: Application To The 3D Reconstruction of the Beating Left Ventricle,", vol. 1679, 1999, pp. 508-515.

[39] J. Cheng, S. Foo and S. Krishnan, "Water-Shed-Presegmented Snake For Boundary Detection And Tracking of Left Ventricular In Echocadiographic Images," *IEEE Transactions on Information Technology in Biomedicine*, vol. 10, no. 2, 2006, pp. 414-416.

[40] S. Osher and J. Sethian, "Fronts Propagating With Curvature-Dependent Speed: Algorithms Based On Hamilton-Jacobi Formulations," *Journal of Computational Physics*, vol. 79, no. 1, 1988, pp. 12-49.

[41] H. Ketout, J. Gu and G. Horne, "Extracting Left Ventricular Contour by MVN_CNN, UBN_CNN and Region Based Level Set Method," *C3S2E '12 Proceedings of the Fifth International C* Conference on Computer Science and Software Engineering*, 2012, pp. 80-85.

[42] J. Cheng and S. Foo, "Markovian LevelSet: A New Method For Boundary Detection For Echocardiographic Images," *IEEE International Conference on Acoustics, Speech and Signal Processing,* 2006, vol. 2, 14-19 May 2006, pp. 2.

[43] K. Saini, M. Dewal and M. Rohit, "Level Set Based on New Signal Pressure Force Function For Echocardiographic Image Segmentation," *International Journal of Innovation and Applied Studies*, vol. 3, 2013, pp. 560-569.

[44] J. Barron and N. Thacker, "Tutorial: Computing 2D And 3D Optical Flow, http://www.tina-vision.net/docs/memos/2004-012.pdf,", 2004.

[45] N. Sahba, V. Tavakoli, A. Ahmadian, M. Abolhassani and M. Fotouhi, "Hybrid Local/Global Optical Flow And Spline Multi-Resolution Analysis Of Myocardial Motion In B-Mode Echocardiography Images," *Electronic Journal «Technical Acoustics»*, 2008.

[46] V. Tavakoli, M. Nambakhsh, N. Sahba and A. Makinian, "A New Variational Technique For Combining Affine Registration And Optical Flow In Echocardiography Images," *30th Annual International Conference of the IEEE Engineering in Medicine and Biology Society,* 2008, pp. 205-208.

[47] V. Tavakoli, N. Sahba, A. Ahmadian, M. Abolhassani, F. Rizi and A. Amini, "Adaptive Multi-Resolution Myocardial Motion Analysis of B-Mode Echocardiography Images Using Combined Local/Global Optical Flow," *2nd International Conference on Bioinformatics and Biomedical Engineering,* 2008, pp. 2303-2306.

[48] M. Unser, G. Pelle, P. Brun and M. Eden, "Automated Extraction Of Serial Myocardial Borders From M-Mode Echocardiograms," *IEEE Transactions on Medical Imaging,* vol. 8, no. 1, 1989, pp. 96-103.

[49] M. Suhling, M. Arigovindan, C. Jansen, P. Hunziker and M. Unser, "Myocardial Motion Analysis From B-Mode Echocardiograms," *IEEE Transactions on Image Processing*, vol. 14, no. 4, 2005, pp. 525-536.

[50] Y. Chunke, K. Terada and S. Oe, 'Motion Analysis Of Echocardiograph Using Optical Flow Method," *IEEE International Conference on Systems, Man, and Cybernetics,* 1996, vol. 1, 1996, pp. 672-677.

[51] G. Mailloux, F. Langlois, P. Simard and M. Bertrand, "Restoration Of The Velocity Field Of The Heart From Two-Dimensional Echocardiograms," *IEEE Transactions on Medical Imaging*, vol. 8, no. 2, 1989, pp. 143-153.

[52] D. Boukerroui, J. Noble and M. Brady, "Velocity Estimation in Ultrasound Images: A Block Matching Approach,", vol. 2732, 2003, pp. 586-598.

[53] P. Baraldi, A. Sarti, C. Lamberti, A. Prandini and F. Sgallari, "Evaluation Of Differential Optical Flow Techniques On Synthesized Echo Images," *IEEE Transactions on Biomedical Engineering*, vol. 43, no. 3, 1996, pp. 259-272.

[54] A. Giachetti, "On-Line Analysis Of Echocardiographic Image Sequences," *Med.Image Anal.*, vol. 2, no. 3, 1998, pp. 261-284.

[55] S. Riyadi, N. Zakaria, M. Mustafa, A. Hussain and O. Maskon I, "Cardio-Spatial Profile Extraction Using Optical Flow Of Echocardiographic Images," *International Association of Engineers*, 2009.

[56] S. Riyadi, M.M. Mustafa, A. Hussain, O. Maskon and I.F.M. Noh, "Segmental Boundary Profile Of Myocardial Motion To Localize Cardiac Abnormalities," *WCE 2010 - World Congress on Engineering,* vol. 1, 2010, pp. 692-697.

[57] S. Riyadi, M. Mustafa, A. Hussain, O. Maskon and I. Nor, "Myocardial Motion Analysis Using Modified Radial Direction Distribution Based on Magnitude Criteria,"

Third International Conference on Intelligent Systems, Modelling and Simulation (ISMS), 2012, pp. 209-213.

[58] M. Suhling, M. Arigovindan, P. Hunziker and M. Unser, "Motion Analysis Of Echocardiograms Using A Local-Affine, Spatio-Temporal Model," *IEEE International Symposium on Biomedical Imaging,* 2002, pp. 573-576.

[59] Q. Duan, E. Angelini, S. Herz, O. Gérard, P. Allain, C. Ingrassia, K. Costa, J. Holmes, S. Homma and A. Laine, "Tracking of LV Endocardial Surface on Real-Time Three-Dimensional Ultrasound with Optical Flow,", 2005, pp. 434-445.

[60] G. Hamarneh, K. Althoff and T. Gustavsson, "Snake Deformations Based on Optical Flow Forces for Contrast Agent Tracking in Echocardiography," *Proceedings of the Swedish Symposium on Image Analysis, SSAB 2000*, 2000.

[61] R. Szeliski, "Computer Vision: Algorithms and Applications,", Springer, 1st Edition, 2010.

[62] I. Herlin and N. Ayache, "Features Extraction And Analysis Methods For Sequences Of Ultrasound Images,", vol. 588, 1992, pp. 43-57.

[63] I.L. Herlin, C. Nguyen and C. Graffigne, "A Deformable Region Model Using Stochastic Processes Applied To Echocardiographic Images," *IEEE Computer Society Conference on Computer Vision and Pattern Recognition,* 1992, pp. 534-539.

[64] N. Friedland and D. Adam, "Automatic Ventricular Cavity Boundary Detection From Sequential Ultrasound Images Using Simulated Annealing," *IEEE Transactions on Medical Imaging*, vol. 8, no. 4, 1989, pp. 344-353.

[65] J. Dias and J. Leitao, "Wall Position And Thickness Estimation From Sequences Of Echocardiographic Images," *IEEE Transactions on Medical Imaging*, vol. 15, no. 1, 1996, pp. 25-38.

[66] T. Cootes, C. Taylor, D. Cooper and J. Graham, '"Active Shape Models-Their Training and Application," *Comput.Vision Image Understanding*, vol. 61, no. 1, 1995, pp. 38-59.

[67] G. Hamarneh and T. Gustavsson, "Deformable Spatio-Temporal Shape Models: Extending Active Shape Models To 2D+Time," *Image Vision Comput.*, vol. 22, no. 6, 2004, pp. 461-470.

[68] D. Comaniciu, X. Zhou and S. Krishnan, "Robust Real-Time Myocardial Border Tracking For Echocardiography: An Information Fusion Approach," *IEEE Transactions on Medical Imaging*, vol. 23, no. 7, 2004, pp. 849-860.

[69] K. Leung and J. Bosch, "Local Wall-Motion Classification in Echocardiograms Using Shape Models And Orthomax Rotations,", vol. 4466, 2007, pp. 1-11.

[70] J. Nascimento and J. Marques, "Robust Shape Tracking With Multiple Models in Ultrasound Images," *IEEE Transactions on Image Processing*, vol. 17, no. 3, 2008, pp. 392-406.

[71] T. Cootes, "Active Appearance Models," *IEEE Transactions on Pattern Analysis and Machine Intelligence*, vol. 23, 2006, pp. 681-685.

[72] G. Jacob, J. Noble, C. Behrenbruch, A. Kelion and A. Banning, "A Shape-Space-Based Approach To Tracking Myocardial Borders And Quantifying Regional Left-Ventricular Function Applied In Echocardiography," *IEEE Transactions on Medical Imaging*, vol. 21, no. 3, 2002, pp. 226-238.

[73] G. Jacob, J. Noble, M. Mulet-Parada and A. Blake, "Evaluating A Robust Contour Tracker On Echocardiographic Sequences," *Med. Image Anal.*, vol. 3, no. 1, 1999, pp. 63-75.

[74] G. Jacob, J. Noble, A. Kelion and A. Banning, "Quantitative Regional Analysis Of Myocardial Wall Motion," *Ultrasound Med.Biol.*, vol. 27, no. 6, 2001, pp. 773-784.

[75] A. Blake, R. Curwen and A. Zisserman, "A Framework For Spatiotemporal Control In The Tracking Of Visual Contours," *International Journal of Computer Vision*, vol. 11, no. 2, 1993, pp. 127-145.

[76] F. Orderud, "A Framework For Real-Time Left Ventricular Tracking In 3D+T Echocardiography, Using Nonlinear Deformable Contours And Kalman Filter Based Tracking," *Computers in Cardiology,* 2006, pp. 125-128.

[77] F. Orderud and S.I. Rabben, "Real-time 3D Segmentation Of The Left Ventricle Using Deformable Subdivision Surfaces," *IEEE Conference on Computer Vision and Pattern Recognition,* 2008, pp. 1-8.

[78] F. Orderud, G. Kiss, S. Langeland, E. Remme, H. Torp and S. Rabben, "Real-time Left Ventricular Speckle-Tracking in 3D Echocardiography With Deformable Subdivision Surfaces," *Proceedings of the MICCAI workshop on Analysis of Medical Images*, 2008, pp. 41-48.

[79] E. Dikici and F. Orderud, "Generalized Step Criterion Edge Detectors for Kalman Filter Based Left Ventricle Tracking in 3D+T Echocardiography," *Statistical Atlases and Computational Models of the Heart.Imaging and Modelling Challenges*, vol. 7746, 2013, pp. 261-269.

[80] T. McInerney and D. Terzopoulos, "A Finite Element Model for 3D Shape Reconstruction And Nonrigid Motion Tracking," *IEEE proceedings on Computer vision*, 1993, pp. 518-523.

[81] S. Choi and M. Kim, "Motion Visualization Of Human Left Ventricle With A Time-Varying Deformable Model For Cardiac Diagnosis," *The Journal Of Visualization And Computer Animation*, vol. 12, 2001, pp. 55-66.

[82] A. Young, D. Kraitchman, L. Dougherty and L. Axel, "Tracking And Finite Element Analysis Of Stripe Deformation In Magnetic Resonance Tagging," *IEEE Transactions on Medical Imaging*, vol. 14, no. 3, 1995, pp. 413-421.

[83] Jinah Park, D. Metaxas and L. Axel, "Deformable Models With Parameter Functions For Left Ventricle 3-D Wall Motion Analysis And Visualization," *Computers in Cardiology,* 1995, pp. 241-244.

[84] C. Conti1, E. Votta, C. Corsi, D. De Marchi, G. Tarroni, M. Stevanella, M. Lombardi, O. Parodi, Caiani E. and Redaelli A., "Left Ventricular Modelling:A Quantitative Functional Assessment Tool Based On Cardiac Magnetic Resonance Imaging," *Interface Focus*, 2011, pp. 384-395.

[85] X. Wang, J. Schaerer, S. Huh, Z. Qian, D. Metaxas, T. Chen and L. Axel, "Reconstruction of Detailed Left Ventricle Motion from tMRI Using Deformable Models," *Functional Imaging and Modeling of the Heart*, vol. 4466, 2001, pp. 60-69.

[86] A. Schwartz., "MRI: Advantages and Disadvantages;" *http://www.anapolschwartz.com/practices/gadolinium-nsf/blog/mri-side-effects.html;*, 07/05/2013.

[87] Brain Imaging, "MRI and CT scan Imaging," *http://faculty.washington.edu/chudler/image.html*, 01/05/2011.

[88] Texas Heart Institute at St. Lakes Episcopal Hospital, "http://www.texasheart.org/HIC/Anatomy/index.cfm,", 11/07/2012.

[89] D. Burkhoff, "cardiovascular physiology concepts, http://www.cvphysiology.com/,", 24/10/2012.

[90] R. Klabunde, "Cardiovascular Physiology Concepts, http://www.cvphysiology.com/,", 08/10/2010.

[91] Short Axis View of Left Ventricular, "http://www.yale.edu/imaging/echo_atlas/views/short_axis_lv.html,", 10/07/1999.

[92] P. Sengupta, J. Korinek, M. Belohlavek, J. Narula, M. Vannan, A. Jahangir and B. Khandheria, "Left Ventricular Structure And Function: Basic Science For Cardiac Imaging," *J.Am.Coll.Cardiol.*, vol. 48, no. 10, 2006, pp. 1988-2001.

[93] R. Kaulfers, http://www.as.miami.edu/chemistry/2086/new-chap20/new-chapter%2020_part1-class.htm, 21/03/2010.

[94] M. Nash and P. Hunter, "Computational Mechanics of the Heart," *Journal of Elasticity*, vol. 61, no. 1, 2000, pp. 113-141.

[95] Y. Fung, '"Biomechanics : Mechanical Properties Of Living Tissues,", Springer, 2nd edition,1993.

[96] S. Hollister, "Computational Modeling of Biological Tissue," *http://www.umich.edu/~bme456/ch0overview/bme456overview.htm*. 01/04/2011.

[97] C. Marcucci, R. Lauer and A. Mahajan, "New Echocardiographic Techniques for Evaluating Left Ventricular Myocardial Function," *Seminars in Cardiothoracic and Vascular Anesthesia*, vol. 12, no. 4, 2008, pp. 228-247.

[98] D. Terzopoulos, J. Platt, A. Barr and K. Fleis, "Elastically Deformed Models," *Computer Graphics*, vol. 21, no. 4, 1987, pp. 205-214.

[99] J. Weiss, B. Maker and S. Govindjee, "Finite Element Implementation Of Incompressible, Transversely Isotropic Hyperelasticity," *Comput.Methods Appl.Mech.Eng.*, vol. 135, no. 1, 1996, pp. 107-128.

[100] J. Humphrey, R. Strumpf and F. Yin, "Determination Of A Constitutive Relation For Passive Myocardium: II. Parameter Estimation," *J.Biomech.Eng.*, vol. 112, no. 3, 1990, pp. 340-346.

[101] J. Humphrey, R. Strumpf and F. Yin, "Determination Of A Constitutive Relation For Passive Myocardium: A New Functional Form," *ASME Journal of Biomechanical Engineering*, vol. 112, 1990, pp. 333-339.

[102] H. Ghaemi, K. Behdinan and A. Spence, "In Vitro Technique In Estimation Of Passive Mechanical Properties Of Bovine Heart: Part II. Constitutive Relation And Finite Element Analysis," *Med. Eng.Phys.*, vol. 31, no. 1, 2009, pp. 83-91.

[103] F. Dorri, P. Niederer and P. Lunkenheimer, "A Finite Element Model Of The Human Left Ventricular Systole," *Comput.Methods Biomech.Biomed.Engin.*, vol. 9, no. 5, 2006, pp. 319-341.

[104] S. Hollister, "BME 456: Biosolid Mechanics: Modeling And Applications,", http://www.umich.edu/~bme456/ch0overview/bme456overview.htm, 16/04/2012.

[105] D. Van Campen, J. Huyghe, P. Bovendeerd and T. Arts, "Biomechanics Of The Heart Muscle," *Eur. J. Mech.,A/Solids*, vol. 13, no. 4, 1994, pp. 19-41.

[106] M. Greminger and B. Nelson, "Deformable Object Tracking Using The Boundary Element Method," *IEEE Computer Society Conference on Computer Vision and Pattern Recognition, 2003*, vol. 1, pp. I-289-I-294 vol.1.

[107] G. Beer, I. Smith and C. Duenser, "The Boundary Element Method For Engineering And Scientists,", Springer, 1st Edition, NewYork, 2008.

[108] C. Brebbia and J. Dominguez, "Boundary Elements an Introductory Course,", WIT press, Computational Mechanics Publications, 2nd Edition,1998.

[109] M. Greminger and B. Nelson, "A Deformable Object Tracking Algorithm Based on the Boundary Element Method that is Robust to Occlusions and Spurious Edges," *International Journal of Computer Vision*, vol. 78, no. 1, 2008, pp. 29-45.

[110] A. Foerster and G. Kuhn, "A Field Boundary Element Formulation For Material Nnonlinear Problems At Finite Strains," *Int.J.Solids Structures*, vol. 31, no. 12–13, 1994, pp. 1777-1792.

[111] H. Al-Gahtani and N. Altiero, "Application Of The Boundary Element Method To Rubber-Like Elasticity," *Appl.Math.Model.*, vol. 20, no. 9, 1996, pp. 654-661.

[112] F. Dinan, P. Mosayebi, H. Moghadam, M. Giti and S. Kermani, "A Fully 3D System for Cardiac Wall Deformation Analysis in MRI Data," *Functional Imaging and Modeling of the Heart*, vol. 4466, 2007, pp. 12-21.

[113] X. Papademetris, A. Sinusas, D. Dione, R. Constable and J. Duncan, "Estimation Of 3-D Left Ventricular Deformation From Medical Images Using Biomechanical Models," *IEEE Transactions on Medical Imaging*, vol. 21, no. 7, 2002, pp. 786-800.

[114] G. Karami and D. Derakhshan, "Field Boundary Element Method for Large Deformation Analysis of Hyperelastic Problems," *Scientific Iranica*, vol. 8, no. 2, 2001, pp. 110-122.

[115] P. Persson and G. Strang, "A Simple Mesh Generator in MATLAB," *SIAM Rev*, vol. 46, 2004.

[116] X. Gao, "Numerical Evaluation Of Two-Dimensional Singular Boundary Integrals—Theory and Fortran Code," *J.Comput.Appl.Math.*, vol. 188, no. 1, 2006, pp. 44-64.

[117] J. Singh, H. Klein, D. Huang, S. Reek, M. Kuniss, A. Quesada, D. Huang, D. Cannom, I. Goldenberg, M. Scott McNitt, J. Daubert, W. Zareba and A. Moss, "Left Ventricular Lead Position And Clinical Outcome In The Multicenter Automatic

Defibrillator Implantation Trial–Cardiac Resynchronization Therapy (MADIT-CRT) Trial," *Circulation, American Heart Association*, vol. 123, no. 11, 2011, pp. 1159-1166.

[118] Dassault Systèmes Simulia Corp., Providence, RI, USA, "ABAQUS Theory Manual,", 2010.

[119] Dassault Systèmes Simulia Corp., Providence, RI, USA, "ABAQUS Analysis User's Manual, Vol. 1 : Introduction, Spatial Modeling, Execution and Output,",2010.

[120] Dassault Systèmes Simulia Corp., Providence, RI, USA, "ABAQUS Scripting User's Manual,",2010.

[121] Dassault Systèmes Simulia Corp., Providence, RI, USA, "ABAQUS User Subroutines Reference Manual,", 2010.

[122] L. Cohen, "'On Active Contour Models And Balloons," *CVGIP: Image Understanding, vol. 53,no. 2,1991, pp. 211-218*.

[123] C. Xu and J. Prince, "Gradient VectorFlow: A new External Force For Snakes," *IEEE Computer Society Conference on Computer Vision and Pattern Recognition,* 1997, pp. 66-71.

[124] M. Nixon and A. Aguado, "Feature Extraction and Image Processing,", Newns, 1st Edition, 2002.

[125] R. Kalman, "A New Approach To Linear Filtering And Prediction Problems," *Transactions of the ASME " Journal of Basic Engineering*, no. 82, 1960, pp. 35-45.

[126] G. Welch and G. Bishop, "An Introduction To Kalman Filter, http://www.cs.unc.edu/~welch/media/pdf/kalman_intro.pdf," *University of North Carolina at Chapel Hill, Department of Computer Science*, 08/03/ 2007.

[127] D. Simon, "Optimal State Estimation: Kalman, H Infinity and Nonlinear Approaches,", John Wiley & Sons, 1st Edition, 2006.

[128] Y. Shalom, R. Li and T. Kirubarajan, "Estimation with Applications to Tracking and Navigation: Theory, Algorithms and Software,", John Wiley & Sons, 1st Edition, 2003.

[129] A. Blake and M. Isard, "Active Contours,", Springer, 1st Edition, 2000.

[130] A. Blake, M. Isard and D. Reynard, "Learning To Track The Visual Motion Of Contours," *Artif.Intell.*, vol. 78, no. 1, 1995, pp. 179-212.

[131] M. Irfan, Z. Muhammad, A. Abid, Y. Mohd and R. Arshad, "An Implementation of Active Contour and Kalman Filter for Road Tracking," *International Association of Engineers*, vol. 37, no. 2, 2007.

[132] JCGM, "Evaluation Of Measurement Data — Guide To The Expression Of Uncertainty In Measurement," *http://www.bipm.org/utils/common/documents/jcgm/JCGM_100_2008_E.pdf*, 2008.

[133] S. Bell, "Measurement Good Practice Guide, A Beginner's Guide to Uncertainty of Measurement,", NPL: National Physical Library, no.11, 2001, pp. 1-41.

[134] V. Chalana and Y. Kim, "A Methodology For Evaluation Of Boundary Detection Algorithms On Medical Images," *IEEE Transactions on Medical Imaging*, vol. 16, no. 5, 1997, pp. 642-652.

[135] I. Anderson and J. Bezdek, "Curvature and Tangential Deflection of Discrete Arcs: A Theory Based on the Commutator of Scatter Matrix Pairs and Its Application to Vertex Detection in Planar Shape Data," *IEEE Transactions on Pattern Analysis and Machine Intelligence*, vol. PAMI-6, no. 1, 1984, pp. 27-40.

[136] C. Li, C. Xu, C. Gui and M. Fox, "Level Set Evolution Without Re-initialization: A New Variational Formulation," *IEEE Computer Society Conference on Computer Vision and Pattern Recognition,* vol. 1, *2005*, pp. 430-436.

[137] S. Strauss, E. Gavish and K. Katsnelson, "Interobserver and Intraobserver Variability in the Sonographic Assessment of Fatty Liver," *Am.J.Roentgenol.*, vol. 189, no. 6, 2013, pp. 320-323.

[138] The MICCAI 2009 workshop, September 2009, "LV Segmentation Challenge, Evaluation Methods," *http://smial.sri.utoronto.ca/LV_Challenge/Evaluation.html*, 5/5/2013.

[139] Z. Peroutka, V. Smidl and D. Vosmik, "Challenges And Limits Of Extended Kalman Filter Based Sensorless Control Of Permanent magnet Synchronous Machine Drives," *13th European Conference on Power Electronics and Applications,* 2009, pp. 1-11.

[140] B. Ristic, S. Arulampalam and N. Gordon, "Beyond the Kalman Filter: Particle Filters For Tracking Applications," *Artech House Publishers*, 2004.

[141] B. Martínez, "Speech Enhancement using Kalman Filtering," *Helsinki University of Technology*, 2008, pp. 1-81.

[142] J. LaViola, "A Comparison Of Unscented And Extended Kalman Filtering For Estimating Quaternion Motion," *American Control Conference,* vol. 3, 2003*,* pp. 2435-2440.

[143] J. Ambadan and Y. Tang, "Sigma-Point Kalman Filter Data Assimilation Methods for Strongly Nonlinear Systems," *J.Atmos.Sci.*, vol. 66, no. 2, 2013, pp. 261-285.

[144] R. Capua and A. Bottaro, "Implementation of the Unscented Kalman Filter and a simple Augmentation System for GNSSSDR receivers,", 2012, pp. 2398-2407.

[145] J. Bland and D. Altman, "Statistical Methods For Assessing Agreement Between Two Methods Of Clinical Measurement," *Lancet*, vol. 1, no. 8476, 1986, pp. 307-310.

APPENDIX I

Tracking of Complete Cardiac Cycle

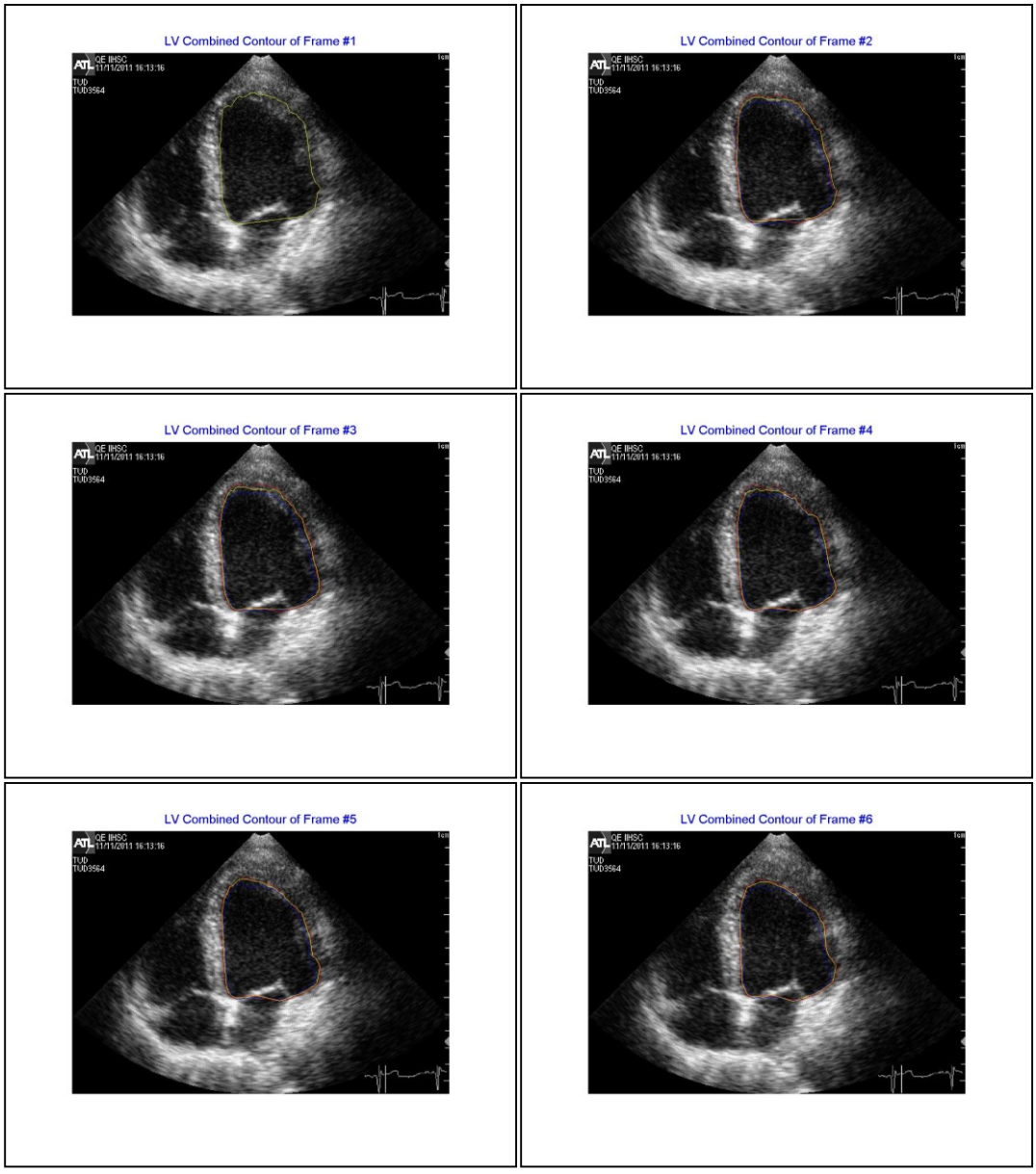

LV Combined Contour of Frame #7

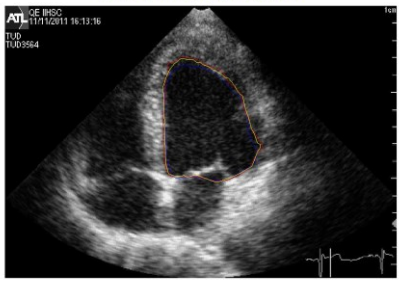

LV Combined Contour of Frame #8

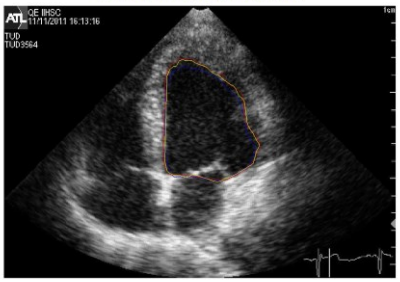

LV Combined Contour of Frame #9

LV Combined Contour of Frame #10

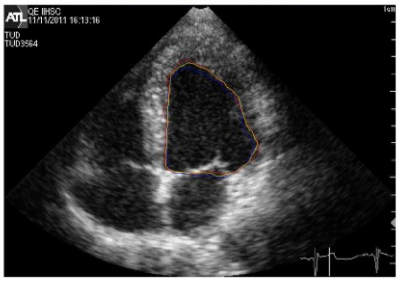

LV Combined Contour of Frame #11

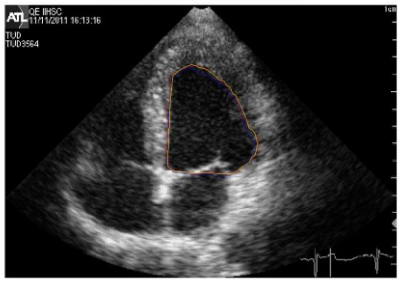

LV Combined Contour of Frame #12

LV Combined Contour of Frame #13

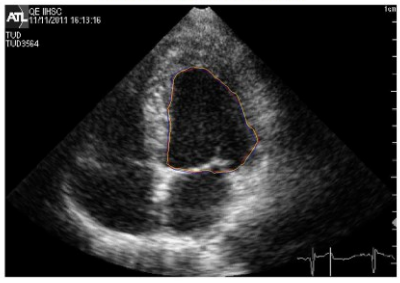

LV Combined Contour of Frame #14

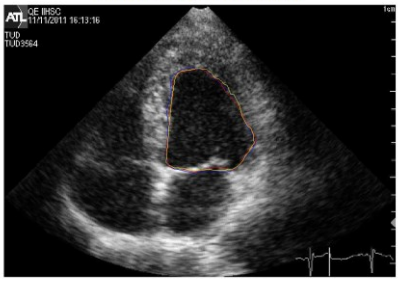

LV Combined Contour of Frame #15

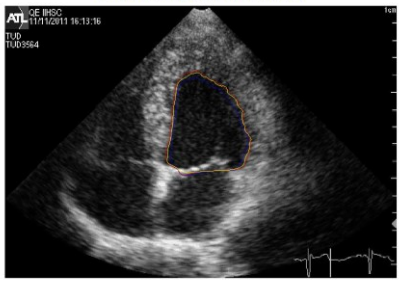

LV Combined Contour of Frame #16

LV Combined Contour of Frame #17

LV Combined Contour of Frame #18

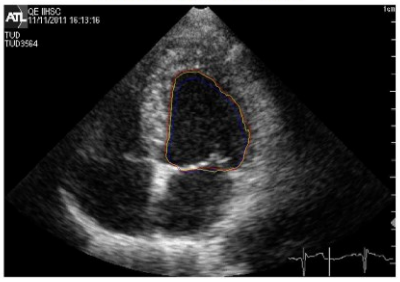

LV Combined Contour of Frame #19

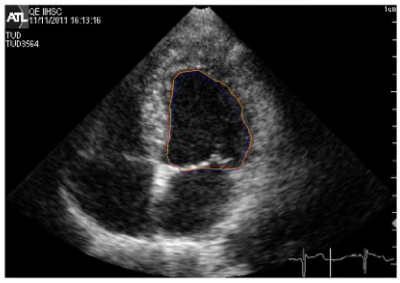

LV Combined Contour of Frame #20

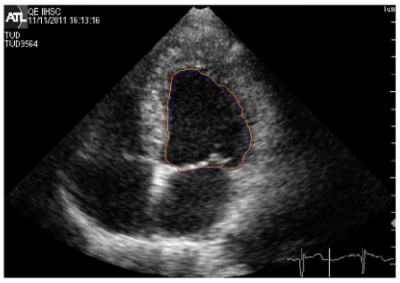

LV Combined Contour of Frame #21

LV Combined Contour of Frame #22

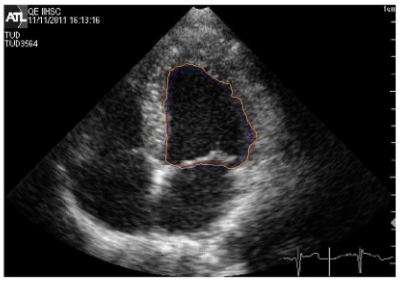

LV Combined Contour of Frame #23

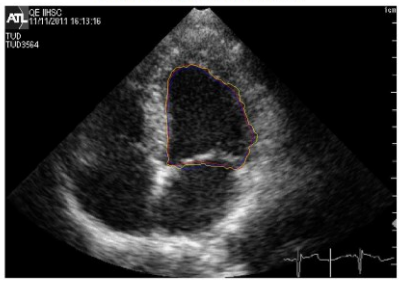

LV Combined Contour of Frame #24

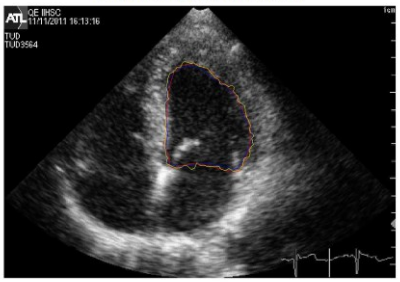

LV Combined Contour of Frame #25

LV Combined Contour of Frame #26

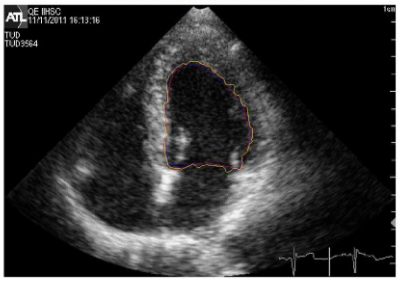

LV Combined Contour of Frame #27

LV Combined Contour of Frame #28

LV Combined Contour of Frame #29

LV Combined Contour of Frame #30

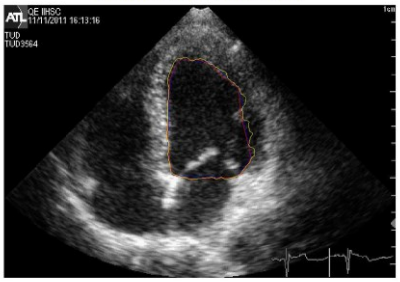

LV Combined Contour of Frame #31

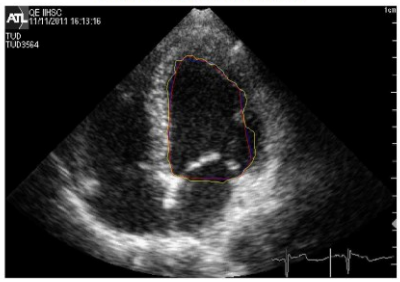

LV Combined Contour of Frame #32

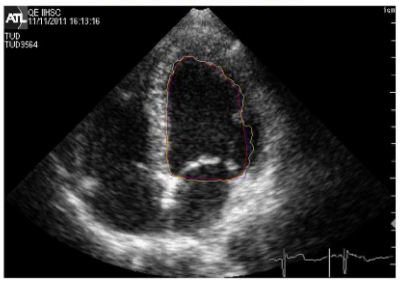

LV Combined Contour of Frame #33

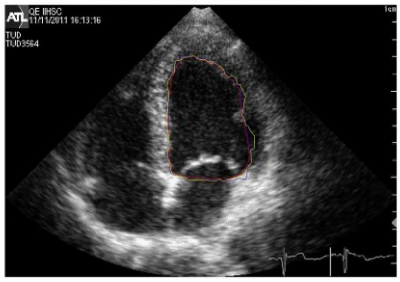

LV Combined Contour of Frame #34

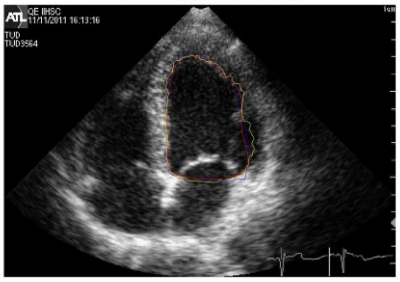

LV Combined Contour of Frame #35

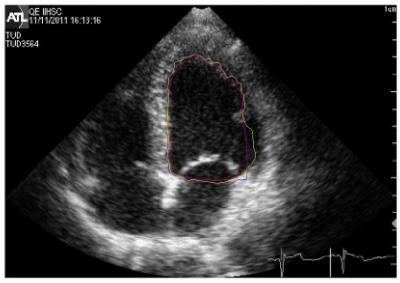

LV Combined Contour of Frame #36

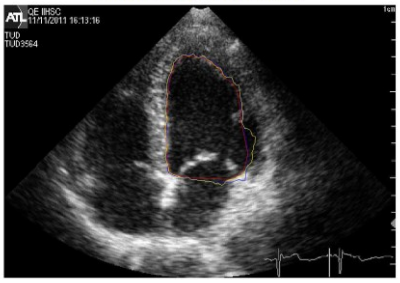

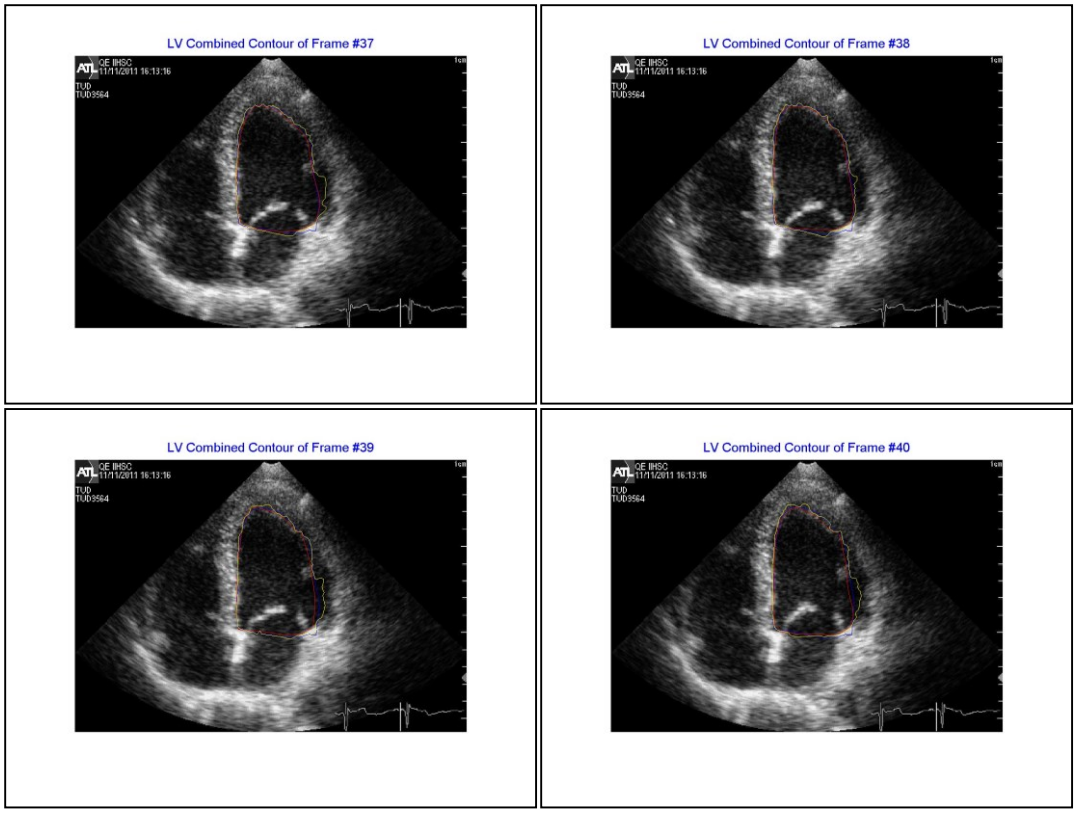

Forty frames for the complete cardiac cycle starting from the QRS signal at the EDS up to the appearance of the next QRS signal

APPENDIX II

Computed Deformations of the LV during Contraction Phase (unit in cm)

Node = 1 U[x] = 0.0743	U[y] = -0.0073
Node = 2 U[x] = 0.0786	U[y] = 0.0002
Node = 3 U[x] = 0.1116	U[y] = 0.1749
Node = 4 U[x] = 0.0693	U[y] = -0.0102
Node = 5 U[x] = 0.0835	U[y] = 0.0097
Node = 6 U[x] = 0.1109	U[y] = 0.1807
Node = 7 U[x] = 0.1125	U[y] = 0.2224
Node = 8 U[x] = 0.0648	U[y] = -0.0129
Node = 9 U[x] = 0.1101	U[y] = 0.1872
Node = 10 U[x] = 0.0881	U[y] = 0.0207
Node = 11 U[x] = 0.1107	U[y] = 0.2199
Node = 12 U[x] = 0.1110	U[y] = 0.2283
Node = 13 U[x] = 0.1085	U[y] = 0.1707
Node = 14 U[x] = 0.1093	U[y] = 0.1931
Node = 15 U[x] = 0.1079	U[y] = 0.1662
Node = 16 U[x] = 0.1074	U[y] = 0.1612
Node = 17 U[x] = 0.1087	U[y] = 0.1984
Node = 18 U[x] = 0.1066	U[y] = 0.1548
Node = 20 U[x] = 0.1089	U[y] = 0.2174
Node = 21 U[x] = 0.1096	U[y] = 0.2342
Node = 23 U[x] = 0.1058	U[y] = 0.1472
Node = 24 U[x] = 0.0573	U[y] = -0.0150
Node = 26 U[x] = 0.0912	U[y] = 0.0347
Node = 27 U[x] = 0.1079	U[y] = 0.2131
Node = 28 U[x] = 0.1047	U[y] = 0.1376
Node = 30 U[x] = 0.1070	U[y] = 0.2089
Node = 32 U[x] = 0.1029	U[y] = 0.1250

Node = 33 U[x] = 0.1061	U[y] = 0.2047
Node = 34 U[x] = 0.0931	U[y] = 0.0446
Node = 36 U[x] = 0.1052	U[y] = 0.2006
Node = 37 U[x] = 0.0495	U[y] = -0.0176
Node = 38 U[x] = 0.1003	U[y] = 0.1068
Node = 41 U[x] = 0.1061	U[y] = 0.2379
Node = 42 U[x] = 0.0950	U[y] = 0.0519
Node = 48 U[x] = 0.0978	U[y] = 0.0917
Node = 50 U[x] = 0.0457	U[y] = -0.0178
Node = 55 U[x] = 0.0958	U[y] = 0.0846
Node = 57 U[x] = 0.0427	U[y] = -0.0180
Node = 60 U[x] = 0.0936	U[y] = 0.0575
Node = 61 U[x] = 0.1033	U[y] = 0.2416
Node = 64 U[x] = 0.0942	U[y] = 0.0802
Node = 68 U[x] = 0.0932	U[y] = 0.0770
Node = 70 U[x] = 0.0395	U[y] = -0.0180
Node = 78 U[x] = 0.0916	U[y] = 0.0763
Node = 79 U[x] = 0.0361	U[y] = -0.0180
Node = 87 U[x] = 0.0994	U[y] = 0.2442
Node = 88 U[x] = 0.0900	U[y] = 0.0754
Node = 89 U[x] = 0.0899	U[y] = 0.0611
Node = 91 U[x] = 0.0328	U[y] = -0.0175
Node = 95 U[x] = 0.0889	U[y] = 0.0731
Node = 100 U[x] = 0.0293	U[y] = -0.0170
Node = 103 U[x] = 0.0872	U[y] = 0.0701
Node = 110 U[x] = 0.0253	U[y] = -0.0169
Node = 118 U[x] = 0.0951	U[y] = 0.2427
Node = 119 U[x] = 0.0857	U[y] = 0.0656
Node = 125 U[x] = 0.0186	U[y] = -0.0159
Node = 134 U[x] = 0.0908	U[y] = 0.2428

Node = 142 U[x] = 0.0109	U[y] = -0.0108
Node = 145 U[x] = 0.0884	U[y] = 0.2419
Node = 151 U[x] = 0.0865	U[y] = 0.2413
Node = 157 U[x] = 0.0000	U[y] = -0.0000
Node = 160 U[x] = 0.0848	U[y] = 0.2412
Node = 163 U[x] = 0.0830	U[y] = 0.2411
Node = 167 U[x] = 0.0000	U[y] = 0.0000
Node = 168 U[x] = 0.0813	U[y] = 0.2418
Node = 176 U[x] = 0.0795	U[y] = 0.2425
Node = 185 U[x] = 0.0776	U[y] = 0.2409
Node = 186 U[x] = 0.0000	U[y] = 0.0000
Node = 190 U[x] = 0.0751	U[y] = 0.2387
Node = 195 U[x] = 0.0707	U[y] = 0.2366
Node = 196 U[x] = 0.0000	U[y] = 0.0000
Node = 200 U[x] = 0.0679	U[y] = 0.2403
Node = 209 U[x] = 0.0639	U[y] = 0.2415
Node = 214 U[x] = 0.0000	U[y] = 0.0000
Node = 215 U[x] = 0.0601	U[y] = 0.2393
Node = 222 U[x] = 0.0566	U[y] = 0.2358
Node = 229 U[x] = 0.0524	U[y] = 0.2379
Node = 234 U[x] = 0.0000	U[y] = 0.0000
Node = 235 U[x] = 0.0491	U[y] = 0.2356
Node = 241 U[x] = 0.0460	U[y] = 0.2329
Node = 248 U[x] = 0.0440	U[y] = 0.2314
Node = 250 U[x] = 0.0426	U[y] = 0.2302
Node = 255 U[x] = 0.0410	U[y] = 0.2306
Node = 259 U[x] = 0.0393	U[y] = 0.2309
Node = 262 U[x] = 0.0373	U[y] = 0.2329
Node = 266 U[x] = 0.0354	U[y] = 0.2348
Node = 270 U[x] = 0.0339	U[y] = 0.2356

Node = 274 U[x] = 0.0000	U[y] = 0.0000
Node = 275 U[x] = 0.0324	U[y] = 0.2364
Node = 281 U[x] = 0.0303	U[y] = 0.2367
Node = 287 U[x] = 0.0282	U[y] = 0.2370
Node = 290 U[x] = 0.0265	U[y] = 0.2361
Node = 295 U[x] = 0.0248	U[y] = 0.2352
Node = 297 U[x] = 0.0238	U[y] = 0.2328
Node = 300 U[x] = 0.0223	U[y] = 0.2298
Node = 302 U[x] = 0.0206	U[y] = 0.2260
Node = 308 U[x] = 0.0168	U[y] = 0.2229
Node = 309 U[x] = 0.0000	U[y] = 0.0000
Node = 315 U[x] = 0.0137	U[y] = 0.2202
Node = 320 U[x] = 0.0105	U[y] = 0.2161
Node = 325 U[x] = 0.0090	U[y] = 0.2124
Node = 327 U[x] = 0.0079	U[y] = 0.2096
Node = 329 U[x] = 0.0069	U[y] = 0.2073
Node = 335 U[x] = 0.0051	U[y] = 0.2068
Node = 339 U[x] = 0.0033	U[y] = 0.2063
Node = 342 U[x] = 0.0017	U[y] = 0.2057
Node = 344 U[x] = -0.0000	U[y] = 0.0000
Node = 349 U[x] = 0.0002	U[y] = 0.2050
Node = 353 U[x] = -0.0015	U[y] = 0.2047
Node = 357 U[x] = -0.0031	U[y] = 0.2045
Node = 359 U[x] = -0.0042	U[y] = 0.2025
Node = 362 U[x] = -0.0056	U[y] = 0.2000
Node = 366 U[x] = -0.0074	U[y] = 0.1967
Node = 375 U[x] = -0.0106	U[y] = 0.1942
Node = 377 U[x] = -0.0000	U[y] = 0.0000
Node = 380 U[x] = -0.0116	U[y] = 0.1901
Node = 382 U[x] = -0.0127	U[y] = 0.1849

Node = 384 U[x] = -0.0139	U[y] = 0.1796
Node = 386 U[x] = -0.0149	U[y] = 0.1754
Node = 392 U[x] = -0.0168	U[y] = 0.1718
Node = 396 U[x] = -0.0187	U[y] = 0.1682
Node = 399 U[x] = -0.0205	U[y] = 0.1650
Node = 404 U[x] = -0.0223	U[y] = 0.1619
Node = 405 U[x] = 0.0000	U[y] = 0.0000
Node = 416 U[x] = -0.0252	U[y] = 0.1572
Node = 420 U[x] = -0.0265	U[y] = 0.1539
Node = 422 U[x] = -0.0277	U[y] = 0.1505
Node = 432 U[x] = -0.0286	U[y] = 0.1468
Node = 437 U[x] = -0.0289	U[y] = 0.1442
Node = 440 U[x] = -0.0000	U[y] = 0.0000
Node = 441 U[x] = -0.0275	U[y] = 0.1411
Node = 443 U[x] = -0.0165	U[y] = 0.0033
Node = 447 U[x] = -0.0247	U[y] = 0.0093
Node = 449 U[x] = -0.0270	U[y] = 0.1392
Node = 452 U[x] = -0.0310	U[y] = 0.0154
Node = 454 U[x] = -0.0356	U[y] = 0.0212
Node = 456 U[x] = -0.0281	U[y] = 0.1403
Node = 459 U[x] = -0.0310	U[y] = 0.1380
Node = 464 U[x] = -0.0351	U[y] = 0.1365
Node = 467 U[x] = -0.0455	U[y] = 0.1002
Node = 468 U[x] = -0.0380	U[y] = 0.1342
Node = 470 U[x] = -0.0393	U[y] = 0.0241
Node = 472 U[x] = -0.0405	U[y] = 0.1314
Node = 474 U[x] = -0.0445	U[y] = 0.0330
Node = 477 U[x] = -0.0480	U[y] = 0.1050
Node = 478 U[x] = -0.0493	U[y] = 0.0964
Node = 481 U[x] = -0.0486	U[y] = 0.0421

Node = 484 U[x] = -0.0446	U[y] = 0.1297
Node = 490 U[x] = -0.0467	U[y] = 0.1273
Node = 491 U[x] = -0.0520	U[y] = 0.0472
Node = 492 U[x] = -0.0530	U[y] = 0.0925
Node = 493 U[x] = -0.0488	U[y] = 0.1249
Node = 494 U[x] = -0.0518	U[y] = 0.1081
Node = 495 U[x] = -0.0521	U[y] = 0.1115
Node = 497 U[x] = -0.0542	U[y] = 0.0534
Node = 498 U[x] = -0.0551	U[y] = 0.0873
Node = 499 U[x] = -0.0524	U[y] = 0.1149
Node = 501 U[x] = -0.0527	U[y] = 0.1183
Node = 502 U[x] = -0.0566	U[y] = 0.0603
Node = 503 U[x] = -0.0529	U[y] = 0.1218
Node = 504 U[x] = -0.0571	U[y] = 0.0820
Node = 505 U[x] = -0.0584	U[y] = 0.0651
Node = 506 U[x] = -0.0596	U[y] = 0.0690
Node = 507 U[x] = -0.0599	U[y] = 0.0732
Node = 508 U[x] = -0.0602	U[y] = 0.0770

APPENDIX III

Computed Deformations of the LV during Passive Phase (unit in cm)

Node = 1 U[x] = -0.0056	U[y] = 0.0004
Node = 2 U[x] = -0.0066	U[y] = -0.0010
Node = 3 U[x] = -0.0043	U[y] = 0.0011
Node = 4 U[x] = -0.0073	U[y] = -0.0024
Node = 5 U[x] = -0.0030	U[y] = 0.0017
Node = 6 U[x] = -0.0077	U[y] = -0.0035
Node = 7 U[x] = -0.0079	U[y] = -0.0043
Node = 8 U[x] = -0.0081	U[y] = -0.0049
Node = 9 U[x] = -0.0017	U[y] = 0.0011
Node = 16 U[x] = -0.0076	U[y] = -0.0059
Node = 17 U[x] = -0.0000	U[y] = 0.0000
Node = 21 U[x] = -0.0075	U[y] = -0.0071
Node = 23 U[x] = -0.0000	U[y] = -0.0000
Node = 28 U[x] = -0.0072	U[y] = -0.0085
Node = 30 U[x] = 0.0000	U[y] = -0.0000
Node = 34 U[x] = -0.0068	U[y] = -0.0101
Node = 35 U[x] = -0.0034	U[y] = -0.0253
Node = 36 U[x] = -0.0037	U[y] = -0.0237
Node = 38 U[x] = -0.0027	U[y] = -0.0277
Node = 40 U[x] = -0.0039	U[y] = -0.0225
Node = 41 U[x] = -0.0000	U[y] = -0.0000
Node = 42 U[x] = -0.0022	U[y] = -0.0290
Node = 43 U[x] = -0.0041	U[y] = -0.0216
Node = 44 U[x] = -0.0019	U[y] = -0.0300
Node = 45 U[x] = -0.0062	U[y] = -0.0117
Node = 48 U[x] = -0.0046	U[y] = -0.0185
Node = 49 U[x] = -0.0041	U[y] = -0.0206

Node = 50 U[x] = -0.0044	U[y] = -0.0191
Node = 51 U[x] = -0.0015	U[y] = -0.0306
Node = 52 U[x] = -0.0045	U[y] = -0.0181
Node = 53 U[x] = -0.0041	U[y] = -0.0197
Node = 55 U[x] = -0.0054	U[y] = -0.0134
Node = 56 U[x] = -0.0011	U[y] = -0.0310
Node = 58 U[x] = -0.0044	U[y] = -0.0176
Node = 61 U[x] = 0.0000	U[y] = -0.0000
Node = 62 U[x] = -0.0044	U[y] = -0.0169
Node = 63 U[x] = -0.0049	U[y] = -0.0148
Node = 65 U[x] = -0.0007	U[y] = -0.0312
Node = 69 U[x] = -0.0043	U[y] = -0.0161
Node = 78 U[x] = -0.0003	U[y] = -0.0314
Node = 86 U[x] = 0.0003	U[y] = -0.0315
Node = 92 U[x] = 0.0000	U[y] = -0.0000
Node = 100 U[x] = 0.0010	U[y] = -0.0317
Node = 110 U[x] = 0.0019	U[y] = -0.0318
Node = 116 U[x] = -0.0000	U[y] = -0.0000
Node = 121 U[x] = 0.0032	U[y] = -0.0320
Node = 132 U[x] = 0.0050	U[y] = -0.0322
Node = 133 U[x] = -0.0000	U[y] = -0.0000
Node = 145 U[x] = -0.0000	U[y] = -0.0000
Node = 146 U[x] = 0.0071	U[y] = -0.0301
Node = 154 U[x] = 0.0000	U[y] = -0.0000
Node = 160 U[x] = 0.0092	U[y] = -0.0281
Node = 163 U[x] = 0.0000	U[y] = -0.0000
Node = 169 U[x] = 0.0000	U[y] = -0.0000
Node = 172 U[x] = 0.0103	U[y] = -0.0265
Node = 177 U[x] = 0.0000	U[y] = -0.0000
Node = 185 U[x] = 0.0000	U[y] = -0.0000

Node = 191 U[x] = 0.0112	U[y] = -0.0253
Node = 192 U[x] = 0.0000	U[y] = -0.0000
Node = 195 U[x] = 0.0113	U[y] = -0.0244
Node = 200 U[x] = 0.0000	U[y] = -0.0000
Node = 203 U[x] = 0.0115	U[y] = -0.0236
Node = 206 U[x] = 0.0025	U[y] = 0.0004
Node = 214 U[x] = 0.0120	U[y] = -0.0227
Node = 216 U[x] = 0.0042	U[y] = 0.0001
Node = 218 U[x] = 0.0052	U[y] = -0.0005
Node = 224 U[x] = 0.0060	U[y] = -0.0010
Node = 226 U[x] = 0.0125	U[y] = -0.0218
Node = 227 U[x] = 0.0065	U[y] = -0.0014
Node = 231 U[x] = 0.0070	U[y] = -0.0017
Node = 232 U[x] = 0.0126	U[y] = -0.0202
Node = 234 U[x] = 0.0077	U[y] = -0.0026
Node = 235 U[x] = 0.0125	U[y] = -0.0192
Node = 236 U[x] = 0.0123	U[y] = -0.0181
Node = 239 U[x] = 0.0084	U[y] = -0.0036
Node = 240 U[x] = 0.0122	U[y] = -0.0170
Node = 242 U[x] = 0.0121	U[y] = -0.0160
Node = 243 U[x] = 0.0092	U[y] = -0.0049
Node = 245 U[x] = 0.0099	U[y] = -0.0063
Node = 246 U[x] = 0.0104	U[y] = -0.0072
Node = 247 U[x] = 0.0122	U[y] = -0.0145
Node = 248 U[x] = 0.0114	U[y] = -0.0106
Node = 249 U[x] = 0.0108	U[y] = -0.0081
Node = 250 U[x] = 0.0121	U[y] = -0.0132
Node = 251 U[x] = 0.0117	U[y] = -0.0112
Node = 252 U[x] = 0.0115	U[y] = -0.0101
Node = 253 U[x] = 0.0112	U[y] = -0.0090

APPENDIX IV

Tables of the X-Y coordinate for the ten samples and their created gold standard

Table (1) – Computing the gold standard for the Sample No. 1

Observer_1		Observer_2		Observer_3		Gold Standard	
X	Y	X	Y	X	Y	X	Y
203.16	40.73	203.6	44.75	201.25	44	202.67	43.16
203.03	61.47	204.21	65.26	196.41	64.24	200.48	63.78
203.71	82.44	202.25	85.57	197.11	85.02	201.02	84.34
205.36	103.35	206.36	105.76	201.17	105.44	204.29	104.85
207.47	124.22	210.11	126.02	203.7	126.11	207.09	125.45
208.37	145.08	209.37	146.55	206.77	146.7	208.17	146.11
205.36	165.79	206.42	166.93	201.91	166.8	204.56	166.51
201.44	186.08	201.69	186.84	198.79	186.87	200.64	186.6
210.77	203.81	211.22	204.52	213.5	201.14	211.83	203.16
223.09	209.38	225.34	210.72	226.1	208.98	224.84	209.69
244.01	207.89	245.81	208.34	246.93	207.9	245.59	208.04
264.86	205.57	266.21	205.45	267.65	205.43	266.24	205.48
285.59	202.35	286.46	201.63	288.07	201.17	286.71	201.72
305.15	195.61	304.83	193.32	306.31	191.79	305.43	193.57
301.85	176.68	303.15	173.66	308.99	172.19	304.66	174.18
308.31	156.95	310.5	154.55	309.03	151.55	309.28	154.35
312.73	136.47	309.99	134.01	307.59	130.98	310.1	133.82
311.04	115.64	305.18	114.1	302.16	110.83	306.13	113.52
303.84	95.95	290.11	100.24	295.23	91.19	296.39	95.79
291.83	78.88	280.89	82.09	287.58	71.78	286.77	77.58
278.85	62.41	275.55	62.21	279	52.81	277.8	59.14
265.18	46.49	264.85	44.83	264.69	37.83	264.91	43.05
248.92	33.56	246.28	36.43	245.83	29.09	247.01	33.02
229.22	26.43	226.06	32.43	225.21	26.95	228.02	30.22
210.79	33.71	206.6	35.16	206.48	35.03	207.96	34.63

Table (2) – Computing the gold standard for the Sample No. 2

Observer_1		Observer_2		Observer_3		Gold Standard	
X	Y	X	Y	X	Y	X	Y
223.97	50.71	224.72	65.99	221.42	53	223.37	56.57
221.91	68.72	220.93	82.6	217.41	71.32	219.91	74.33
220.46	87.43	219.97	99.75	214.1	89.79	218.18	92.32
220.69	106.26	220.82	116.86	213.02	108.53	218.18	110.55
220.85	125.13	217.24	133.46	213.93	127.26	217.34	128.62
212.52	141.73	209.51	148.74	204.32	142.69	208.78	144.39
202.13	157.3	201	163.35	196.06	159.21	199.73	159.95
198.26	175.62	201.77	180.3	196.49	177.91	198.84	177.94
208.18	190.26	205.07	196.2	199.27	194.34	204.17	193.6
216.32	202.32	221.5	200.47	213.46	200.05	217.09	200.94
235.12	203.9	238.65	201.36	232.19	201.36	235.32	202.21
254.01	203.97	255.83	201.22	250.96	201.93	253.6	202.37
272.85	202.78	272.94	199.89	269.73	201.56	271.84	201.41
290.25	196.97	288.57	194.11	287.93	197.87	288.92	196.32
285.94	179.44	284.78	178.02	286.64	180.73	285.78	179.39
291.96	161.65	290.89	162.28	293.88	163.65	292.25	162.53
296.24	143.26	294.43	145.76	298.84	145.91	296.5	144.98
294.17	124.61	289.3	129.43	296.53	127.28	293.33	127.1
289.47	106.32	284.33	113.03	290.93	109.38	288.24	109.58
283.38	88.51	275.59	98.9	283.39	92.2	280.78	93.2
273.27	72.57	267.62	84.91	274.36	75.74	271.75	77.74
266.4	55.01	267.36	67.77	267.66	58.22	267.14	60.34
253.27	41.6	259.27	52.9	258.14	42.7	256.9	45.74
235.81	35.52	244.26	50.39	240.3	37.09	242.82	41.71
221.14	41.78	229.53	58.92	224.02	44.12	224.9	48.27

Table (3) – Computing the gold standard for the sample No. 3

Observer_1		Observer_2		Observer_3		Gold Standard	
X	Y	X	Y	X	Y	X	Y
182.62	43.07	184.06	55.36	181.36	49.77	182.6	49.4
180.32	62.06	184.02	73.88	179.29	68.83	181.53	68.38
180.53	81.39	184.12	92.47	180.23	88.34	181.63	87.4
183.27	100.53	183.12	111.03	178.11	107.77	181.5	106.45
183.88	119.84	183.24	129.62	177.07	127.29	181.39	125.59
182.33	139.12	183.67	148.21	176.65	146.83	180.88	144.72
181.12	158.43	183.32	166.79	179.2	166.2	181.21	163.81
183.21	177.57	186.13	184.84	184.18	185.08	184.51	182.5
193.68	193.63	196.58	199.5	195.69	200.14	195.32	197.76
205.1	197.53	214.69	201.12	208.65	203.06	209.48	200.57
224.33	195.41	233.03	198.08	227.93	199.85	228.43	197.78
243.53	193.11	251.24	194.31	247.2	196.55	247.32	194.66
262.7	190.53	269.33	190.01	266.43	192.99	266.15	191.18
281.47	186.16	287.17	184.83	285.19	187.72	284.61	186.24
291.92	174.66	291.22	169.49	295.17	173.46	292.77	172.54
295.63	155.98	291.76	150.93	296.32	154.03	294.57	153.65
293.76	136.75	289.64	132.65	295.58	134.73	292.99	134.71
286.75	118.86	280.12	116.69	289.18	116.26	285.35	117.27
278.86	101.24	274.54	98.99	284.44	97.3	279.28	99.18
266.54	86.71	263.78	83.91	273.95	81.08	268.09	83.9
251.78	74.27	251.59	69.87	258.47	69.15	253.95	71.09
238.21	60.52	237.91	57.3	245.48	54.63	240.53	57.48
221.82	50.29	221.54	48.61	227.44	47.37	223.6	48.76
206	39.31	204.86	40.7	208.2	44.04	206.35	43.71
189.22	36.18	188.05	47.09	189	43.81	188.76	42.36

Table (4) – Computing the gold standard for sample No. 4

Observer_1		Observer_2		Observer_3		Gold Standard	
X	Y	X	Y	X	Y	X	Y
207.03	68.25	206.3	73.87	202.08	70.66	205.14	70.93
202.49	82.26	201.79	87.47	198.31	85.39	200.52	85.08
199.68	96.66	200.37	101.73	195.11	100.23	198.39	99.54
200.46	111.37	200.6	116.08	195.15	115.46	198.74	114.3
199.91	126.06	198.62	130.29	195.42	130.69	197.98	129.01
196.24	140.33	196.89	144.51	193.92	145.82	195.68	143.56
196.03	154.5	198.5	158.72	194.95	160.84	196.49	158.02
202.86	167.47	204.7	171.48	200.63	174.59	202.73	171.18
205.48	178.55	208.12	182.29	202.8	183.37	205.47	181.4
220.18	179.26	222.42	182.78	217.98	181.99	220.19	181.35
234.92	178.95	236.73	181.67	233.15	180.67	234.93	180.43
249.64	178.17	250.97	179.84	248.32	179.25	249.64	179.09
264.32	176.9	265.1	177.33	263.46	177.6	264.3	177.28
278.7	173.96	278.68	172.91	278.31	174.48	278.56	173.78
280.48	161.01	279.95	160.35	279.55	161.65	279.99	161
285.21	147.24	282.31	146.6	279.87	147.46	282.46	147.1
277.24	135.14	276.19	133.72	276.02	132.85	276.48	133.9
267.44	124.16	267.18	122.55	267.99	120.15	267.54	122.29
261.49	111.5	262.65	109.19	264.9	105.35	263.01	108.68
261.76	96.83	261.34	94.97	261.73	90.59	261.61	94.13
254.85	84.01	253.14	83.39	253.33	77.97	253.77	81.79
243.83	74.26	241.75	74.65	242.67	67.21	242.75	72.04
233.71	63.72	232.01	64.17	232.57	56.47	232.76	61.45
222.73	55.07	219.81	58.19	217.59	55.26	221.27	58.86
210.22	61.63	209.3	67.36	205.33	63.82	208.28	64.27

Table (5) – Computing the gold standard for the sample No. 5

Observer_1		Observer_2		Observer_3		Gold Standard	
X	Y	X	Y	X	Y	X	Y
206.99	35.61	210.4	39.9	192.03	48.62	202.78	41.37
195.63	51.94	195	50.81	194.14	71.89	196.29	59.65
197.48	72.45	196.14	70.62	197.13	95.12	196.92	79.39
197.96	93.04	199.87	90.23	197.94	118.57	198.59	100.61
198.39	113.63	200.95	110.16	201.82	141.73	200.38	121.84
203.08	133.72	203.88	129.88	205.06	164.97	204	142.86
205.86	154.17	207.22	149.52	214.46	186.48	209.18	163.39
210.32	174.26	209.29	169.34	229.6	203.33	216.41	182.31
222.35	190.18	219.68	186.14	212	201.93	218.01	192.75
230.21	204.19	231.06	199.21	220.67	202.4	227.31	201.94
250.13	209.43	250.07	205.29	243.57	207.7	247.92	207.48
270.55	212.38	269.42	210.21	266.58	212.5	268.85	211.69
291.16	213.36	289.07	213.75	289.76	216.34	290	214.49
309.71	207.08	307.79	210.64	312.75	214.94	310.08	210.88
304.35	187.78	304.82	191.44	307.4	194.56	305.52	191.26
305.17	167.41	306.22	171.6	304.73	171.72	305.37	170.24
302.21	147.01	302.45	152.01	300.36	148.67	301.67	149.23
296.61	127.15	298.17	132.52	296.91	125.48	297.23	128.38
290.64	107.39	294.05	112.98	287.37	104.03	290.69	108.14
285.83	87.32	287.7	94.08	280.18	81.68	284.57	87.69
280.71	67.32	278.45	76.4	273.2	59.28	277.45	67.67
272.07	48.74	272.49	57.35	263.37	38.4	269.31	48.16
256.85	34.83	259.87	43.01	242.26	29.36	252.99	35.73
237.4	31.37	240.2	39.81	218.81	29.29	233.73	31.92
216.86	33.07	220.29	38.63	197.38	38.48	211.51	36.73

Table (6) – Computing the gold standard for the sample No. 6

Observer_1		Observer_2		Observer_3		Gold Standard	
X	Y	X	Y	X	Y	X	Y
211.2	35.43	213.67	34.26	210.26	31.48	211.71	33.72
199.39	48.58	200.44	45.67	196.79	45.13	201.39	48.21
197.11	66.56	196.9	62.84	195.84	64.61	196.62	64.67
198.37	84.73	199.03	80.39	194.73	84.22	197.38	83.11
199.36	102.91	199.8	98.06	195.25	103.83	198.14	101.6
204.59	120.3	202.17	115.52	199.21	123.05	201.99	119.62
211.18	137.17	209.75	131.48	204.19	142.05	208.37	136.9
210.52	155.36	211.57	149.05	207.48	161.41	209.85	155.27
213.02	173.37	212.72	166.71	213.66	179.84	213.13	173.31
222.63	187.51	220.33	181.95	217.14	193.38	220.03	187.61
236.78	194.69	233.69	191.13	236.45	196.96	235.64	194.26
254.96	195.75	251.28	193.09	255.91	199.58	254.05	196.14
273.17	195.2	268.97	193.52	275.48	201.27	272.54	196.66
289.5	189.1	285.3	188.5	293.49	197.31	289.43	191.64
289.4	171.49	286.35	171.1	290.28	178.64	288.68	173.75
289.97	153.8	286.82	153.54	294.91	160	290.57	155.78
287.06	135.84	284.04	136.05	293.54	140.43	288.21	137.44
283.23	118.05	281.38	118.55	289.62	121.25	284.74	119.28
282.03	99.88	277.94	101.18	284.63	102.3	281.53	101.12
276.5	82.56	272.43	84.38	281.78	82.88	276.9	83.27
270.7	65.33	267.44	67.41	276.91	63.85	271.68	65.53
267.64	47.47	266.5	49.78	269.97	45.53	268.03	47.59
253.41	36.44	255.75	38.38	257.73	30.41	255.63	35.08
237.22	28.46	238.98	32.73	238.94	25.88	238.89	29.25
219.44	31.56	221.73	30.68	219.46	28.12	220.08	30.12

Table (7) – Computing the gold standard for the sample No. 7

Observer_1		Observer_2		Observer_3		Gold Standard	
X	Y	X	Y	X	Y	X	Y
171.29	65.22	172.23	69.87	172.58	61.92	172.03	65.67
168.69	86.32	172.56	90.69	167.94	83.02	171.45	86.84
176.31	106.16	181.15	109.45	171.11	104.46	176.19	106.69
189.96	122.64	190.4	128.05	178.37	124.97	186.24	125.22
194.04	143.59	195.38	148.34	185.58	145.49	191.67	145.81
194.74	165.07	198.13	169.01	189.81	166.79	194.23	166.95
193.95	186.52	197.13	189.87	192.85	188.27	194.64	188.22
203.22	204.57	204.21	208.98	196.25	209.11	201.23	207.56
211.71	212.99	216.68	213.45	206.9	216.15	211.76	214.2
232.8	208.9	236.87	208.07	228.24	211.91	232.64	209.63
253.83	204.44	256.89	202.08	249.45	207.04	253.39	204.52
274.76	199.58	276.79	195.69	270.56	201.78	274.04	199.02
295.54	194.07	296.51	188.8	291.57	196.09	294.54	192.99
315.11	185.63	315.33	179.91	312.2	189.22	314.21	184.92
307.35	168.5	307.01	163.98	315.03	172.33	309.8	168.27
309.16	147.34	308.35	143.51	311.62	150.84	309.71	147.23
300.24	128.06	294.64	127.92	301.89	131.52	298.92	129.17
285.1	112.82	280.02	113.02	289.87	113.39	285	113.08
270.34	97.29	268.55	95.72	279.7	94.16	272.86	95.72
259.01	79.04	257.62	78.22	267.93	75.93	261.52	77.73
243.18	64.58	238.98	68.9	252.17	60.95	244.78	64.81
226.47	51.11	221.3	57.8	234.89	47.73	227.55	52.21
207.47	41.13	204.85	44.92	215.74	37.64	209.35	41.23
188.41	38.05	186.26	42.76	194.24	38.59	192.21	42.46
176.01	55.58	174.44	59.68	177.91	52.45	176.12	55.91

Table (8) – Computing the gold standard for the sample No. 8

Observer_1		Observer_2		Observer_3		Gold Standard	
X	Y	X	Y	X	Y	X	Y
197.62	76.42	198.78	82.48	192.9	82.35	196.44	80.42
198.73	92.33	199.18	98.3	192.7	98.84	196.05	96.48
197.31	108.27	197.44	114.09	192.74	115.33	195.83	112.56
197.25	124.26	197.36	129.93	192.75	131.82	195.79	128.67
197.66	140.26	199.95	145.58	192.67	148.31	196.76	144.72
197.74	156.26	199.1	161.42	194.85	164.62	197.23	160.77
200.41	171.94	202.96	176.62	199.61	180.36	201	176.31
205.13	186.44	210.03	190.61	206.48	194.69	207.22	190.58
211.47	198.44	213.1	200.3	208.79	205.38	211.12	201.37
227.32	197.37	224.27	196.49	225.06	202.86	225.55	198.91
242.87	193.63	239.54	192.15	241.05	198.83	241.16	194.87
258.14	188.82	254.76	187.62	256.81	193.97	256.57	190.14
273.07	183.06	269.85	182.67	272.23	188.14	271.71	184.62
286.6	174.83	283.81	175.43	285.88	179.3	285.43	176.52
278.34	162.9	278.53	162.27	279.68	165.99	278.85	163.72
276.51	147.22	276.62	146.63	277.52	150.13	276.88	147.99
271.83	132.14	267.82	133.61	274.4	134.19	271.35	133.31
261.11	120.95	257.27	121.82	267.48	119.23	261.95	120.67
257.04	105.61	253.1	106.63	260.8	104.16	256.98	105.47
249.28	91.64	249.87	91.18	252.38	89.99	250.51	90.94
240.76	78.45	238.95	79.92	242.31	77.02	240.67	78.46
226.36	71.52	224.77	72.81	228.45	68.1	226.53	70.81
212.97	62.88	212.65	62.76	214.87	58.87	213.5	61.5
201.26	54.34	200.94	59.74	198.96	59.2	203.16	62.06
195.99	68.59	197.11	74.72	193.4	74.12	195.5	72.48

Table (9) – Computing the gold standard for the sample No. 9

Observer_1		Observer_2		Observer_3		Gold Standard	
X	Y	X	Y	X	Y	X	Y
190.77	59.4	194.33	61.7	197.68	54.93	194.26	58.68
183.39	77.38	183.05	76.59	183.76	68.39	184.56	75.08
180.5	96.56	181.96	95.22	178.11	86.89	180.19	92.89
182.42	115.95	182.42	114	178.62	106.37	181.15	112.1
184.83	135.28	186.36	132.36	179.35	125.86	183.52	131.17
185.35	154.75	188.24	151.03	180.7	145.32	184.76	150.36
185.34	174.22	187.58	169.81	182.08	164.77	185	169.6
190.48	192.79	188.65	188.56	184.01	184.14	187.71	188.49
203.74	206.2	198.73	204.08	191.54	201.17	198	203.82
206.24	209.6	208.1	209.25	201.67	210.78	205.34	209.88
222.69	211.34	226.85	207.89	221.17	210.36	223.57	209.86
242.04	209.05	245.59	206.38	240.64	209.11	242.76	208.18
261.37	206.6	264.31	204.67	260.07	207.42	261.92	206.23
280.38	202.54	282.87	201.9	279.45	205.21	280.9	203.22
293.32	188.47	292.15	187.61	292.02	192.03	292.5	189.37
301.46	171.53	301.51	171.83	303.24	176.81	302.07	173.39
297.03	152.65	298.1	153.47	301.48	157.48	298.87	154.53
289.34	134.75	292.17	135.67	293.52	139.71	291.68	136.71
280.98	117.15	281.62	120.12	286.05	121.7	282.89	119.66
272.47	99.63	273.46	103.23	279.23	103.43	275.05	102.1
262.37	83.11	264.22	86.9	270.56	85.99	265.72	85.33
249.42	68.61	250.79	73.8	256.52	72.64	252.24	71.68
233.67	58.18	236.15	62.03	241.77	59.88	237.2	60.03
216.18	49.77	218.79	54.92	224.65	51	220.24	53.59
197.74	52.71	200.84	55.01	205.58	49.33	201.39	52.35

Table (10) – Computing the gold standard for the sample No. 10

Observer_1		Observer_2		Observer_3		Gold Standard	
X	Y	X	Y	X	Y	X	Y
206.14	89.47	205.34	93.87	205.74	83.99	205.74	89.11
201.71	104.52	200.68	108.42	201.07	99.37	201.71	104.31
201.29	120.36	199.76	123.71	198.16	115.22	199.74	119.76
201.63	136.2	201.19	138.98	196.61	131.26	199.81	135.48
199.28	151.77	199.37	154.18	194.63	147.25	197.76	151.07
196.04	167.07	195.9	168.84	191.32	162.99	194.42	166.3
184.7	177.9	189	181.43	186.42	178.33	186.7	179.22
189.31	188.85	189.95	189.12	189.12	190.65	189.46	189.54
204.82	191.93	205.17	191.09	203.07	193.1	204.36	192.04
220.58	193.61	220.48	192.37	219.08	194.92	220.04	193.63
236.39	194.64	235.8	193.33	235.13	196.43	235.77	194.8
252.22	195.14	251.14	194.03	251.2	197.53	251.52	195.57
268.07	195	266.49	194.38	267.31	197.96	267.29	195.78
283.79	193.34	281.82	193.71	283.11	195.64	282.91	194.23
283.38	181.97	281.11	182.79	284.41	181.75	282.97	182.17
285.07	166.57	283.92	167.89	287.51	166.35	285.5	166.93
286.62	151.03	285.66	152.88	289.94	150.85	287.41	151.59
283.96	135.42	282.21	137.93	284.98	135.55	283.72	136.3
280.35	119.99	276.53	123.69	278.25	120.91	278.38	121.53
275.28	104.99	269.46	110.06	271.68	106.2	272.14	107.09
267.1	91.49	261.44	96.98	265.15	91.49	264.57	93.32
255.54	80.7	251.29	85.48	253.85	80.18	253.56	82.12
241.37	74.14	238.07	78.23	240.11	71.85	239.85	74.74
225.94	77.32	222.96	79.63	224.29	70.17	224.84	75.03
211.56	83.75	205.34	93.87	210.12	77.27	210.51	83